



Méthode d'optimisation multi-segmentaire pour l'estimation de la cinématique articulaire : propositions d'amélioration

Vincent Richard

► To cite this version:

Vincent Richard. Méthode d'optimisation multi-segmentaire pour l'estimation de la cinématique articulaire : propositions d'amélioration. Biomécanique [physics.med-ph]. Université de Lyon, 2016. Français. NNT : 2016LYSE1090 . tel-01400155

HAL Id: tel-01400155

<https://tel.archives-ouvertes.fr/tel-01400155>

Submitted on 23 Nov 2016

HAL is a multi-disciplinary open access archive for the deposit and dissemination of scientific research documents, whether they are published or not. The documents may come from teaching and research institutions in France or abroad, or from public or private research centers.

L'archive ouverte pluridisciplinaire **HAL**, est destinée au dépôt et à la diffusion de documents scientifiques de niveau recherche, publiés ou non, émanant des établissements d'enseignement et de recherche français ou étrangers, des laboratoires publics ou privés.



N°d'ordre NNT : 2016LYSE1090

THESE de DOCTORAT DE L'UNIVERSITE DE LYON

En cotutelle avec L'UNIVERSITÀ DI BOLOGNA

opérée au sein de
l'Université Claude Bernard Lyon 1

Ecole Doctorale 162
Mécanique Energétique et Génie Civil

Spécialité de doctorat :
Mécanique - Biomécanique

Soutenue publiquement le 28/06/2016, par :

Vincent RICHARD

Multi-body optimization method for the estimation of joint kinematics: prospects of improvement

-

Méthode d'optimisation multi-segmentaire pour
l'estimation de la cinématique articulaire : propositions
d'amélioration

Devant le jury composé de :

FRIGO, Carlo	Professeur à Politecnico di Milano, Italie	Rapporteur
PILLET, Hélène	Maître de Conférences, HDR, à l'ENSAM, France	Rapporteur
CEREATTI, Andrea	Professeur à l'Università degli Studi di Sassari, Italie	Examineur
JACQUELIN, Éric	Professeur à l'Université Claude Bernard Lyon 1, France	Examineur
CAPPOZZO, Aurelio	Professeur à l'Università degli Studi di Roma - Foro Italico, Italie	Directeur de thèse
DUMAS, Raphaël	Directeur de Recherche à l'IFSTTAR, France	Directeur de thèse

THESE de DOCTORAT DE L'UNIVERSITE DE LYON
En cotutelle avec L'UNIVERSITÀ DI BOLOGNA

opérée au sein de
l'Université Claude Bernard Lyon 1

Ecole Doctorale 162
Mécanique Energétique et Génie Civil

Spécialité de doctorat :
Mécanique - Biomécanique

Soutenue publiquement le 28/06/2016, par :

Vincent RICHARD

**Multi-body optimization method for the estimation
of joint kinematics: prospects of improvement**

-

Méthode d'optimisation multi-segmentaire pour
l'estimation de la cinématique articulaire : propositions
d'amélioration

Directeurs de thèse :
Dr. Raphaël DUMAS

Directeur de thèse :
Pr. Aurelio CAPPOZZO

UNIVERSITE CLAUDE BERNARD - LYON 1

Président de l'Université

Président du Conseil Académique

Vice-président du Conseil d'Administration

Vice-président du Conseil Formation et Vie Universitaire

Vice-président de la Commission Recherche

Directeur Général des Services

M. le Professeur Frédéric FLEURY

M. le Professeur Hamda BEN HADID

M. le Professeur Didier REVEL

M. le Professeur Philippe CHEVALIER

M. Fabrice VALLÉE

M. Alain HELLEU

COMPOSANTES SANTE

Faculté de Médecine Lyon Est – Claude Bernard

Directeur : M. le Professeur J. ETIENNE

Faculté de Médecine et de Maïeutique Lyon Sud – Charles Mérieux

Directeur : Mme la Professeure C. BURILLON

Faculté d'Odontologie

Directeur : M. le Professeur D. BOURGEOIS

Institut des Sciences Pharmaceutiques et Biologiques

Directeur : Mme la Professeure C. VINCIGUERRA

Institut des Sciences et Techniques de la Réadaptation

Directeur : M. le Professeur Y. MATILLON

Département de formation et Centre de Recherche en Biologie Humaine

Directeur : Mme la Professeure A-M. SCHOTT

COMPOSANTES ET DEPARTEMENTS DE SCIENCES ET TECHNOLOGIE

Faculté des Sciences et Technologies

Directeur : M. F. DE MARCHI

Département Biologie

Directeur : M. le Professeur F. THEVENARD

Département Chimie Biochimie

Directeur : Mme C. FELIX

Département GEP

Directeur : M. Hassan HAMMOURI

Département Informatique

Directeur : M. le Professeur S. AKKOUCHE

Département Mathématiques

Directeur : M. le Professeur G. TOMANOV

Département Mécanique

Directeur : M. le Professeur H. BEN HADID

Département Physique

Directeur : M. le Professeur J-C PLENET

UFR Sciences et Techniques des Activités Physiques et Sportives

Directeur : M. Y. VANPOULLE

Observatoire des Sciences de l'Univers de Lyon

Directeur : M. B. GUIDERDONI

Polytech Lyon

Directeur : M. le Professeur E. PERRIN

Ecole Supérieure de Chimie Physique Electronique

Directeur : M. G. PIGNAULT

Institut Universitaire de Technologie de Lyon 1

Directeur : M. le Professeur C. VITON

Ecole Supérieure du Professorat et de l'Education

Directeur : M. le Professeur A. MOUGNIOTTE

Institut de Science Financière et d'Assurances

Directeur : M. N. LEBOISNE

Ad angusta per angusta...

Preface

This thesis is submitted as partial fulfilment of the requirement for the Doctor of Philosophy at the University Claude Bernard Lyon 1, Lyon, France and the Doctor of Philosophy at the University Alma Mater Studiorum – Università di Bologna, Bologna, Italy under a convention of *cotutelle*. The collaboration between both institutions has been sustained by a mobility grant from the Mediterranean Office for Youth. The work has been carried out in the period from October 2012 to June 2016 under the joint supervision of Dr. Raphaël DUMAS and Pr. Aurelio CAPPOZZO.

Vincent RICHARD

Lyon, June 2016.

Abstract

The estimate of joint kinematics during motor tasks generally relies on a model of the locomotor apparatus and on the stereophotogrammetric reconstruction of skin-marker trajectories or on the angular velocity and acceleration of the body segments provided by magneto-inertial measurement units. However, these techniques have important limitations including the "soft tissue artefacts" (i.e., the relative movement between the skin markers or the magneto-inertial sensors and the underlying bones). The multi-body optimization (MBO) method aims to compensate for these artefacts by constraining the measured kinematic quantities using selected kinematic models of the joints involved. The mechanical linkages normally used to model the joints, however, prevent satisfactory estimates of their kinematics. This thesis addresses the problem of using MBO as associated with data provided by magneto-inertial measurement units and stereophotogrammetry while analyzing lower limb joints. With regard to the latter technique, the improvement of the outcome of MBO, is sought through two different original approaches: (1) the embedment in MBO of an elastic joint model, based on a knee stiffness matrix, and a physiologically plausible optimization criterion, and (2) the introduction in the optimization process of a "kinematic-dependent" soft tissue artefact model. The present study, through experimental and statistical validation, demonstrates the versatility of the MBO approach, the feasibility of the original solutions proposed, fosters its use in soft tissue artefact compensation, and indicates ways to pursue a further improvement of the relevant outcome accuracy.

Keywords: movement analysis; lower limb; knee; magneto-inertial measurement unit; stiffness matrix; soft tissue artefact; multi-body optimization; biomechanics

Résumé

L'estimation de la cinématique articulaire lors de tâches motrices repose souvent sur un modèle de l'appareil locomoteur et sur la reconstruction de trajectoires de marqueurs cutanés par stéréophotogrammétrie ou de la vitesse angulaire et l'accélération des segments du corps issues de centrales inertielles. Mais ces techniques présentent d'importantes limites, dont les « artéfacts de tissus mous » (i.e., le mouvement relatif entre les marqueurs cutanés ou des centrales inertielles et les os sous-jacents). La méthode d'optimisation multi-segmentaire (MBO) vise à compenser ces artéfacts en imposant des contraintes aux grandeurs cinématiques mesurées à l'aide de modèles cinématiques articulaires. Cependant, les liaisons mécaniques modélisant les articulations empêchent une estimation satisfaisante de la cinématique articulaire. Cette thèse s'intéresse à l'utilisation de la MBO associée à des données issues de centrales inertielles et de stéréophotogrammétrie pour analyser les articulations du membre inférieur. Concernant cette dernière technique, l'amélioration des résultats de la MBO est évaluée à travers deux approches originales : (1) l'implémentation d'un modèle articulaire élastique basé sur la matrice de raideur du genou et un critère d'optimisation physiologiquement plausible, et (2) l'introduction dans la MBO d'un modèle d'artéfact de tissus mous « cinématique-dépendant ». Cette étude, par la validation expérimentale et statistique, démontre la polyvalence de l'approche MBO et la faisabilité des solutions proposées, encourage son utilisation pour la compensation des artéfacts de tissus mous, et indique les moyens pertinents d'améliorer la précision des résultats.

Mots-clés : analyse du mouvement ; membre inférieur ; genou ; centrale inertielle ; matrice de raideur ; artéfacts de tissus mous ; optimisation multi-segmentaire ; biomécanique

Sommario

La stima della cinematica articolare durante l'esecuzione di atti motori si basa su un modello dell'apparato locomotore e sulla ricostruzione stereofotogrammetrica delle traiettorie di marcatori cutanei o sulla velocità angolare e l'accelerazione dei segmenti corporei fornite da sensori inerziali. Tuttavia, queste tecniche presentano importanti limiti il più importante dei quali è "l'artefatto da tessuto molle" (il movimento relativo tra i marcatori o sensori inerziali e l'osso sottostante). Il metodo di ottimizzazione multi corpo (MBO) mira a compensare questi artefatti vincolando le grandezze cinematiche stimate con modelli cinematici delle articolazioni coinvolte. I meccanismi normalmente utilizzati per modellare le articolazioni, però, forzano la fisiologia delle stesse e impediscono stime soddisfacenti della loro cinematica. Questa tesi riguarda l'utilizzo della MBO associata a dati forniti da sensori inerziali e dalla stereofotogrammetria e fa riferimento alle articolazioni degli arti inferiori. Utilizzando, in particolare dati stereofotogrammetrici, i risultati forniti dalla MBO, sono stati valutati attraverso due differenti approcci originali: (1) inclusione nella MBO di un modello articolare elastico, basato su una matrice di rigidità del ginocchio associato ad un criterio di ottimizzazione fisiologicamente plausibile, e (2) introduzione nel processo di ottimizzazione di un modello di artefatto da tessuto molle "cinematica-dipendente". Il presente studio, attraverso la validazione sperimentale e statistica, dimostra la versatilità dell'approccio MBO, la fattibilità delle soluzioni proposte, promuove il suo utilizzo nella compensazione degli artefatti da tessuto molle, ed indica i metodi da utilizzare per un significativo miglioramento della accuratezza.

Parole-chiave: analisi del movimento; arto inferiore; ginocchio; sensore inerziale; matrice di rigidità; artefatti da tessuto molle; ottimizzazione multi corpo; biomeccanica

Résumé étendu

Dans le contexte du vieillissement de la population et de l'augmentation de l'espérance de vie, et afin d'appréhender au mieux les différentes pathologies affectant l'appareil locomoteur humain et ses performances, l'analyse du mouvement est plus que jamais une préoccupation sociale majeure. L'analyse du mouvement humain consiste dans l'observation et la définition des mouvements de la vie des êtres humains, et les recherches dans ce domaine sont nombreuses. Elles captivent une communauté multidisciplinaire et représente un intérêt pour l'orthopédie, le sport ou la vie quotidienne. La biomécanique propose de fournir en outre des connaissances scientifiques sur les causes et les effets des affections de la locomotion. En biomécanique, le mouvement est décrit comme l'ensemble des positions et orientations de segments du corps, déterminées à un instant donné pendant l'observation. En particulier, la cinématique est concernée par l'étude du mouvement d'un point de vue géométrique : elle représente la première étape vers la modélisation musculo-squelettique qui porte sur les causes qui amènent le corps à se déplacer comme il le fait. Evaluer une cinématique précise est donc le fondement essentiel de l'analyse du mouvement. Deux principales grandeurs caractérisant le mouvement sont intéressantes pour l'estimation de la cinématique articulaire : l'attitude des os et le mouvement relatif entre les os adjacents. En général, l'analyse du mouvement est effectuée sur la base des données de mesure de surface, tels que la stéréophotogrammétrie. Au-delà de la complexité de la représentation mathématique de la position et de l'orientation des os se trouve un enjeu majeur. Un problème se pose précisément lors de l'estimation de la cinématique des structures osseuses à l'aide de marqueurs de surface. En effet, la prise en compte de l'erreur observée entre les trajectoires mesurées des marqueurs de surface et la position et l'orientation réelles de l'os sous-jacent est nécessaire pour une estimation précise, du fait que ce que l'on appelle les « artefacts de tissus mous » (STA : *soft tissue artefact*) peut provoquer des mouvements irréalistes de grande amplitude au niveau des articulations. La prise en compte de ce phénomène reste un défi permanent (Leardini et al., 2005), car il empêche une mesure non-invasive directe du mouvement articulaire. Parmi les différentes méthodes de compensation des STAs, l'utilisation d'une méthode d'optimisation multi-segmentaire (MBO : *multi-body optimization*) a été proposée comme une solution potentielle (Lu and O'Connor, 1999), mais n'a à ce jour pas aboutie à des résultats pleinement satisfaisants.

La thèse propose des perspectives d'amélioration de l'estimation de l'attitude des os et de la cinématique articulaire en utilisant la méthode MBO. Le principe de la méthode repose sur la minimisation des erreurs entre les trajectoires de marqueurs cutanés mesurées et modélisées au sens des moindres carrés, au sein d'un modèle cinématique défini.

Tout d'abord, une restriction associée à la stéréophotogrammétrie qui repose sur le fait que le mouvement analysé doit être effectué dans un environnement contrôlé empêchant l'étude des mouvements *in-situ*. L'utilisation de centrales inertielles (MIMUs : *magneto-inertial measurement units*) représente une alternative prometteuse, mais puisque les mesures restent affectées par les STAs, on ne peut s'attendre à une estimation plus précise des positions et orientations des os qu'avec la stéréophotogrammétrie. Les mesures issues des MIMUs peuvent cependant être utilisées dans le cadre de la MBO afin de limiter la propagation des STA. L'orientation calculé à partir de MIMUs a déjà été introduit avec succès au procédé de la méthode MBO pour piloter le modèle cinématique associé (Koning et al., 2015). Cependant, dans cette première tentative, seule la cinématique articulaire a été évaluée et comparée avec celle obtenue par la technique de stéréophotogrammétrie et marqueurs cutanés, et non la position des segments, en particulier le segment terminal de la chaîne cinématique, c'est-à-dire le pied dans le cadre du membre inférieur. En outre, peu de détails ont été fournis sur la façon d'adapter la méthode MBO aux mesures des MIMUs. La calibration du modèle est également essentielle dans un tel procédé : une calibration incorrecte a pour conséquence de propager de larges erreurs à l'attitude estimée des os.

Deuxièmement, la méthode MBO repose sur l'hypothèse que les contraintes articulaires introduites dans le modèle cinématique représentent le comportement réel des articulations. Néanmoins, l'exactitude de ces méthodes basées sur des modèles mécaniques est discutable, en raison notamment de l'introduction de contraintes « strictes (*hard*) » qui empêchent ou prescrivent le mouvement de l'articulation. Les contraintes articulaires peuvent être considérées comme des contraintes « strictes » quand elles doivent être strictement satisfaites, et comme des contraintes « souples (*soft*) » quand elles doivent être minimisées. Évoluer vers des contraintes « souples », qui ne sont plus déterministes, pour modéliser les articulations peut être une alternative efficace pour mieux représenter le comportement réel des articulations (Gasparutto et al., 2015).

Enfin, la méthode MBO ne compense que partiellement les STAs. Des modèles de STAs ont été proposés (Alexander and Andriacchi, 2001; Bonci et al., 2014; Camomilla et al., 2013), jusqu'à présent appliqués seulement à l'optimisation mono-segmentaire (Alexander and Andriacchi, 2001) et l'estimation du centre articulaire (De Rosario et al., 2013). La réduction de la complexité de ces modèles (Camomilla et al., 2015), en particulier du nombre de paramètres les définissant, rend possible leur utilisation dans la méthode MBO et pourrait être une alternative à la calibration spécifique de ces modèles. En d'autres termes, une identification simultanée des paramètres d'un modèle de STAs avec l'estimation de l'attitude des os peut être développée dans le cadre de la méthode MBO.

Le travail de thèse s'articule donc autour de ces trois thématiques.

Suite à une introduction générale (Chapitre 1), le Chapitre 2 propose un état de l'art sur l'analyse du mouvement dans le but d'introduire les connaissances générales en anatomie du membre inférieur, les technologies de systèmes d'acquisition, et les méthodes pour l'estimation de la cinématique. Ce chapitre explore le domaine de l'analyse de mouvement, d'un point de vue biomécanique et identifie les principaux problèmes rencontrés lors de l'évaluation de la cinématique articulaire. Des arguments sont avancés pour légitimer l'utilisation d'une méthode MBO pour l'estimation de la position et de l'orientation des os. La méthode MBO est présentée dans sa version classique, utilisé pour l'analyse cinématique des membres inférieurs à partir des données de stéréophotogrammétrie utilisant des marqueurs cutanés (Lu and O'Connor, 1999), la méthode est détaillée dans le cadre spécifique d'un paramétrage « en coordonnées naturelles » (Dumas and Chèze, 2007). En particulier, ce chapitre développe les modèles articulaires mis en œuvre dans le modèle cinématique de la méthode MBO, la question des STAs, et de le potentiel des nouvelles technologies magnéto-inertielles.

Dans le Chapitre 3, un cadre de modélisation est développé, dérivé de la méthode MBO classique, pour l'adapter à l'utilisation de MIMUs. La méthode développée est utilisée pour étudier la possibilité d'introduire l'orientation, la vitesse angulaire et l'accélération mesurées par les capteurs inertiels dans la fonction objective de la méthode MBO. La méthode développée est testée sur le membre inférieur au cours de la marche, en comparant la cinématique articulaire et la position du pied par rapport au bassin obtenues par la méthode MBO utilisant les MIMUs ou la stéréophotogrammétrie et les marqueurs cutanés. L'hypothèse de cette étude est que réaliser un calibrage anatomique (Picerno et al., 2008) est pertinent pour définir le modèle cinématique inclus dans la méthode MBO. Cette étude vise donc à évaluer l'efficacité d'une méthode qui propose de combiner trois approches : l'estimation de la cinématique articulaire dans le cadre de la méthode MBO (Duprey et al., 2010; Lu and O'Connor, 1999), le suivi de données inertielles mesurées par les MIMUs (Koning et al., 2015) et la procédure de calibration anatomique (Picerno et al., 2008). L'étude a confirmé que l'orientation issue des MIMUs est une donnée d'entrée efficace pour la méthode MBO. La faisabilité de la prise en compte de la vitesse angulaire et de l'accélération comme données d'entrée complémentaires à l'orientation ou comme données d'entrée uniques ouvre des perspectives importantes. En effet, l'orientation des MIMUs résulte d'un traitement qui est sensible aux perturbations magnétiques mais ce n'est pas le cas de la vitesse angulaire et de l'accélération.

De plus, l'obtention d'une cinématique articulaire qui est en accord avec les mesures de vitesse angulaire et d'accélération s'avère pertinent pour des calculs de dynamique.

Dans le Chapitre 4, la performance de la méthode MBO pour estimer la cinématique articulaire du genou est étudiée lorsqu'un modèle élastique dérivé de la matrice de raideur de l'articulation du genou est intégré à la méthode. La matrice de raideur représente le comportement mécanique de l'articulation du genou, mais reste néanmoins sujet-dépendante. Une méthode de pénalité est mise en œuvre pour introduire le modèle élastique d'articulation comme une contrainte « souple » dans la méthode MBO. Un tel modèle cinématique de l'articulation du genou devrait fournir une meilleure estimation que les liaisons mécaniques rigides classiques (contraintes « strictes ») qui empêchent ou prescrivent certains déplacements. Considérant une matrice de raideur unique, cette étude de faisabilité démontre que la méthode est au moins aussi efficace que les méthodes classiques (avec des contraintes mécaniques de type rotule par exemple). En outre, l'analyse de sensibilité réalisée a montré que de grandes variations des coefficients de la matrice de raideur se propagent peu à l'estimation de la cinématique.

Dans le Chapitre 5, un modèle de STAs « cinématique-dépendant » est introduit dans la méthode MBO. Le développement mathématique et de calcul sont effectués tout en utilisant différents types de modèles cinématiques afin d'étudier l'efficacité de la méthode pour l'identification des paramètres du modèle de STAs en même temps que l'estimation de l'attitude des os. L'objectif est d'évaluer et compenser les STAs tout en améliorant la précision de la méthode MBO pour estimer la cinématique articulaire. Testée sur des données de course où les mouvements du membre inférieur sont mesurés par stéréophotogrammétrie avec simultanément des marqueurs cutanés et des marqueurs montés sur des tiges vissées dans l'os, la méthode se révèle inefficace quant à l'amélioration de la précision de l'estimation de la cinématique et démontre l'importance des choix de modélisation (paramètres du modèle de STAs, modèle cinématique).

Sommario esteso

La stima della cinematica articolare durante l'esecuzione di atti motori si basa su un modello dell'apparato locomotore e sulla ricostruzione stereofotogrammetrica delle traiettorie di marcatori cutanei o sull'orientamento, velocità angolare e accelerazione dei segmenti corporei fornite da sensori magneto-inerziali (*magneto-inertial measurement unit*: MIMU). Tuttavia, queste tecniche presentano dei limiti il più importante dei quali è la loro sensibilità "all'artefatto da tessuto molle" (il movimento relativo tra i marcatori o sensori inerziali e l'osso sottostante; *soft tissue artefact*: STA). La misura e la minimizzazione della propagazione ai risultati finali di questo artefatto è una sfida molto attuale vincendo la quale si renderebbe possibile un importante avanzamento di queste metodologie ed un allargamento dello spettro delle loro possibili applicazioni. L'approccio più promettente a tal fine consiste nel metodo di ottimizzazione multi corpo (*multi-body optimization*: MBO). Esso mira a compensare gli STA vincolando le grandezze cinematiche stimate con modelli cinematici delle articolazioni coinvolte. I meccanismi normalmente utilizzati per modellare le articolazioni, però, forzano la fisiologia delle stesse a comportamenti in parte predefiniti e, di conseguenza, impediscono stime soddisfacenti della loro cinematica in casi specifici. Questa tesi ha come obiettivo quello di dare un contributo verso il superamento di questi limiti e riguarda l'utilizzo della MBO associata a dati forniti sia da MIMU che dalla stereofotogrammetria. A scopo esemplificativo vengono prese in considerazione le articolazioni dell'arto inferiore. Per quanto riguarda l'uso dei MIMU, il metodo MBO proposto non sfrutta solo informazioni sull'orientamento, come normalmente fatto, ma anche quelle relative alle accelerazioni e velocità angolari. Utilizzando, invece, dati stereofotogrammetrici il classico metodo della MBO è stato modificato attraverso due differenti approcci originali: (1) inclusione nella MBO di un modello articolare elastico, basato su una matrice di rigidità del ginocchio associato ad un criterio di ottimizzazione fisiologicamente plausibile, e (2) introduzione nel processo di ottimizzazione di un modello di STA "cinematica-dipendente". Il presente studio, attraverso la validazione sperimentale e statistica, dimostra la versatilità dell'approccio MBO, la fattibilità delle soluzioni proposte, promuove il suo utilizzo nella compensazione degli artefatti da tessuto molle, ed indica i metodi da utilizzare per un significativo miglioramento della accuratezza.

La tesi è così organizzata.

Dopo un'introduzione generale (capitolo 1), il capitolo 2 fornisce lo stato dell'arte sull'analisi del movimento con l'obiettivo di introdurre le conoscenze generali dell'anatomia dell'arto inferiore, delle tecnologie dei sistemi di acquisizione del movimento, e i metodi di stima della cinematica.

Speciale attenzione viene dedicata all'uso del metodo MBO per la stima della posa delle ossa. Questo è presentato nella sua versione classica utilizzata per l'analisi cinematica degli arti inferiori da dati ottenuti con la stereofotogrammetria e marcatori cutanei. Il metodo è dettagliato nel contesto specifico di una parametrizzazione in "coordinate naturali". Vengono, inoltre, descritti i modelli articolari normalmente implementati con il metodo MBO, il problema del STA, ed il potenziale delle nuove tecnologie magneto-inerziali.

Nel capitolo 3, il metodo MBO classico, già utilizzato con dati stereofotogrammetrici, viene adattato all'uso di MIMU. In particolare l'orientamento, la velocità angolare e l'accelerazione resi disponibili dai sensori inerziali vengono introdotti nella funzione obiettivo del metodo MBO. Il metodo sviluppato è testato sull'arto inferiore durante il cammino e i suoi risultati vengono confrontati con la cinematica articolare e la posizione del piede rispetto al bacino ottenuti con il metodo MBO e la stereofotogrammetria con marcatori cutanei. Questo studio mira a valutare l'efficacia di un metodo che si propone di combinare tre procedure: la stima della cinematica articolare con il metodo MBO, il monitoraggio di dati inerziali misurati attraverso i MIMU, e la procedura di calibrazione anatomica. Lo studio ha confermato che l'orientamento derivato dai MIMU è un efficace dato di input per il metodo MBO. E' stata verificata anche la fattibilità dell'uso della velocità angolare e dell'accelerazione come dati di input aggiuntivi all'orientamento o come unici dati di ingresso. Ciò apre importanti prospettive. Infatti, l'orientamento dei MIMU è alquanto sensibile ai disturbi magnetici, mentre questo non è il caso per la velocità angolare e l'accelerazione. Inoltre, ottenere una cinematica articolare che è coerente con le misure di velocità angolare e di accelerazione è favorevole ad una stima accurata di grandezze dinamiche.

Nel capitolo 4 viene introdotto un modello elastico del ginocchio concepito per essere integrato nel metodo MBO. Detto modello è rappresentato da una matrice di rigidità ottenuta attraverso esperimenti *ex vivo*. La posa relativa di femore e tibia viene stimata inglobando nella MBO la minimizzazione della variazione di energia elastica del modello. Considerando una singola matrice di rigidità, questo studio di fattibilità dimostra che il metodo è efficace almeno quanto i metodi convenzionali (con vcoli meccanici di tipo sferico per esempio). Questa conclusione è stata ottenuta stimando la cinematica articolare del ginocchio utilizzando tre metodi classici nonché quello presentato in questo studio partendo da dati rilevati *in vivo* con la stereofotogrammetria. I risultati così ottenuti sono stati messi a confronto con la cinematica stimata utilizzando dati ad elevata accuratezza forniti dalla fluoroscopia. Inoltre, l'analisi di sensibilità ha mostrato che variazioni dei coefficienti della matrice di rigidità dovuti a differenze interindividuali e di posa del

ginocchio propagano poco alla stima della cinematica giustificando così l'uso di una singola matrice ottenuta su un singolo reperto anatomico.

Nel capitolo 5, viene presentato un modello di STA "cinematico-dipendente" e come questo viene introdotto nel metodo MBO. L'obiettivo è quello di valutare e compensare il STA e, quindi, migliorare l'accuratezza del metodo MBO nella stima della cinematica articolare. Il metodo è stato valutato su dati di corsa dove i movimenti delle ossa dell'arto inferiore sono stati misurati con la stereofotogrammetria e l'uso simultaneo di marcatori cutanei e marcatori montati su viti inserite nell'osso. Il metodo, seppure promettente, così come implementato nel presente studio è risultato essere non efficace nel miglioramento dell'accuratezza della stima della cinematica lasciando dunque spazio per ulteriori approfondimenti sul tema.

Acknowledgements

I would like to express my special thanks and esteem to my supervisors Dr. Raphaël DUMAS and Pr. Aurelio CAPPOZZO for their continuous support and guidance during the past years. Both of them have been tremendous mentors for me. I would like to acknowledge them for encouraging my research and for allowing me to grow as a research scientist. I appreciate all their contributions of time and ideas to make my PhD experience productive and stimulating. I am also thankful for the excellent example they have provided as successful and influent researchers.

I would like to thank everyone from the department of Mechanics at the Université Claude Bernard Lyon 1 for creating a good working environment. A special thanks goes to my “roommates” in the ground floor office.

I would like to thank everyone in the office at the University of Rome – Foro Italico for the hospitality. Your freshness made my warm time in Rome more comfortable.

A thanks also goes to everyone that I had the chance to meet at the Laboratoire de Biomécanique et Mécanique des Chocs.

I would like to thank my family and my longtime friends.

The greatest acknowledgement goes to Audrey for her support and patience during these long years.

Contents

Preface	7
Abstract	8
Résumé	9
Sommario	10
Résumé étendu	11
Acknowledgements.....	18
Contents	19
List of figures.....	22
List of tables.....	23
Notations and symbols.....	24
Chapter 1. Introduction	27
1. Background and motivation	27
2. Scope of the study	28
3. Thesis outline	29
Chapter 2. Literature review – state-of-the-art.....	31
1. Lower limb anatomy - osteoarticular description	31
1.1. Anatomical terminology	31
1.1.1. Anatomical reference position	31
1.1.2. Directional terms	32
1.1.3. Anatomical reference planes	32
1.1.4. Anatomical reference axis.....	32
1.1.5. Terms of movement for the lower limb.....	33
1.2. Human locomotor apparatus	34
1.2.1. Overview of the skeleton.....	34
1.2.1.a. Pelvis.....	36
1.2.1.b. Thigh.....	36
1.2.1.c. Shank.....	36
1.2.1.d. Foot.....	38
1.2.2. Joints of the lower limb	38
1.2.2.a. Structure.....	38
1.2.2.b. Hip joint	38
1.2.2.c. Knee joint.....	38
1.2.2.d. Ankle joint.....	40
2. Motion analysis	41
2.1. History of movement analysis	41
2.2. Issues in movement analysis	42
2.3. Kinematics.....	43
2.4. Dealing with skin markers – technological limitations	44
2.5. Soft tissue artefact	45
2.5.1. General characteristics of soft tissue artefact	45
2.5.2. Soft tissue artefact assessment and compensation.....	46
2.5.3. Modeling of soft tissue artefact	47
2.5.4. Conclusion	49
3. Alternative to stereophotogrammetry.....	50
3.1. Medical imaging	50
3.1.1. X-ray	50
3.1.2. Ultrasounds.....	51
3.1.3. Magnetism.....	51
3.1.4. Conclusion	51
3.2. Magneto-inertial measurement units	52
3.2.1. Device description and specification	52
3.2.2. Soft tissue artefact.....	54

4. Modeling and bone pose estimation – multi-body optimization	55
4.1. Rigid multi-body systems	55
4.2. Parameter set and systems of coordinates	55
4.3. Segment and joint coordinate systems	59
4.3.1. Segment coordinate system	59
4.3.2. Joint coordinate system	60
4.4. Constraints	63
4.4.1. Rigid body constraints	63
4.4.2. Kinematic constraints	64
4.4.2.a. Spherical joint	65
4.4.2.b. Hinge joint	65
4.4.2.c. Universal joint	65
4.4.2.d. Parallel mechanism	66
4.4.3. Driving constraints	67
4.5. Optimization	68
4.5.1. Formulation of the problem	68
4.5.2. Lagrangian formulation	68
Chapter 3. Multi-body optimization using magneto-inertial measurement units	70
1. Introduction	70
2. Materials and methods	71
2.1. Measured data and procedure	71
2.2. Multi-body optimization framework	74
2.2.1. Modeled orientation	74
2.2.2. Modeled angular velocity	75
2.2.3. Modeled acceleration	75
2.2.1. Objective function	77
2.3. Experimental methods	79
2.4. Statistics	81
3. Results	81
3.1. Comparative study of the joint kinematics estimates	81
3.1.1. Bias	83
3.1.2. Standard deviation	83
3.1.3. Root mean square differences	83
3.1.4. Correlation coefficient	83
3.2. Objective function residual and mean differences between measured and modeled parameters	85
3.3. Foot position and error	85
4. Discussion	86
Chapter 4. Knee kinematics estimation using multi-body optimization embedding a knee joint stiffness matrix	89
1. Introduction	89
2. Materials and methods	91
2.1. Multi-body optimization	91
2.2. Knee stiffness matrix	94
2.3. Validation data and procedure	95
2.3.1. Experimental methods	96
2.3.2. Sensitivity analysis	96
2.3.3. Statistics	99
3. Results	99
3.1. Comparative analysis of the knee kinematics estimates	99
3.1.1. Bias	99
3.1.2. Standard deviation	102
3.1.3. Root mean square error	103
3.1.4. Correlation coefficient	103
3.2. Sensitivity	105

4. Discussion.....	105
Chapter 5. Simultaneous optimization of bone pose and soft tissue artefact model parameters through multi-body optimization: a feasibility study	109
1. Introduction	109
2. Materials and methods.....	111
2.1. Mathematical representation of the STA model.....	111
2.2. STA rigid component model	113
2.3. Multi-body optimization.....	115
2.4. Validation data and procedure.....	118
2.5. Evaluation of STA model implementation and MBO effectiveness	118
2.6. Part 1: Overview and selection of relevant models	119
2.6.1. Objectives and procedure.....	119
2.6.2. Results.....	120
2.6.2.a. STA rigid component model approximated by six modes.....	120
2.6.2.b. STA rigid component model approximated by three modes	122
2.6.3. Discussion.....	125
2.7. Part 2: Evaluation of the selected models.....	126
2.7.1. Objectives and procedure.....	126
2.7.2. Results.....	127
2.7.3. Intermediate discussion.....	133
3. Discussion and conclusion	134
Chapter 6. General discussion	137
References	140

List of figures

Figure 2.1 Anatomical planes and axes	33
Figure 2.2 Lower limb overview	35
Figure 2.3 Skeletal framework of the lower limb (Moore and Dalley, 2006).....	37
Figure 2.5 Example of 3D parallel mechanism for knee modeling (Parenti-castelli et al., 2004).....	39
Figure 2.6 Example of 3D parallel mechanism for ankle modeling (Di Gregorio et al., 2007)	40
Figure 2.7 Movement analysis	41
Figure 2.8 The human movement analysis laboratory.....	44
Figure 2.9 Motion capture workflow	45
Figure 2.10 Representation of the lower limb	56
Figure 2.11 Segment parameters in the global reference frame (ICS)	58
Figure 2.12 Joint coordinate system	61
Figure 2.13 Classic joint models for the hip, the knee and the ankle.....	64
Figure 3.1 Lower limb joint angles during walking cycle.	82
Figure 3.2 Bland Altman plot.	84
Figure 3.3 Foot position and error with respect to the reference.	86
Figure 4.1 Model specifications.....	92
Figure 4.2 Distribution of coefficients of stiffness matrix samples	98
Figure 4.3 Bland Altman plot for subject S1.....	100
Figure 4.4 Bland Altman plot for subject S2.....	101
Figure 4.5 Knee joint angles and displacements, $U = [\theta_1 \ \theta_2 \ \theta_3 \ d_1 \ d_2 \ d_3]^T$ for both subjects.	104
Figure 5.1 Framework for the mathematical representation of the STA	113
Figure 5.2 Knee joint kinematics model N_6^h	120
Figure 5.3 Amplitude estimate's time histories for model N_6^h	121
Figure 5.4 Amplitude estimate's time histories for model N_6^h	122
Figure 5.5 Knee joint angle kinematics for models S_3^h , N_3^h and S_3^a	123
Figure 5.6 Amplitude estimate's time histories for models S_3^h , N_3^h and S_3^a	124
Figure 5.7 Amplitude model parameters h estimate for model S_3^h and N_3^h	124
Figure 5.8 Knee joint angles for model S_3^h and S_3^a	128
Figure 5.9 Root mean square errors (RMSE) for models S , S_3^h and S_3^a	129
Figure 5.10 Correlation coefficient (R^2) for models S , S_3^h and S_3^a	129
Figure 5.11 Amplitude estimate's time histories for models S_3^h and S_3^a	130
Figure 5.12 Amplitude estimate's time histories for models S_3^h and S_3^a	131
Figure 5.13 Root mean square errors (RMSE) for S_3^h and S_3^a	132
Figure 5.14 Correlation coefficient (R^2) for models S_3^h and S_3^a	133

List of tables

Table 2.1 Directional terms	32
Table 2.2 Description of segments parameters	57
Table 3.1 Methods notation.....	80
Table 3.2 Residual and mean difference.....	85

Notations and symbols

MBO	Multi-body optimization
SBO	Single-body optimization
STA	Soft tissue artefact
MIMU	Magneto-inertial measurement unit
DoF	Degree of freedom
ICS	Inertial coordinate system
JCS	Joint coordinate system
EF	Extension/Flexion
AA	Adduction/Abduction
IER	Internal/External rotation
LM	Lateral/Medial displacement
AP	Anterior/Posterior displacement
PD	Proximal/Distal displacement
N	No joint model
S	Spherical model
P	Parallel mechanism
M	Elastic joint model based on the stiffness matrix
i	Body segment index ($i = 2$: foot; $i = 3$: shank; $i = 4$: thigh; $i = 5$: pelvis)
\mathbf{Q}_i	Natural coordinates of segment i
P_i	Proximal endpoint of segment i
D_i	Distal endpoint of segment i
\mathbf{u}_i	Components of the frontal unitary direction vector of segment i
\mathbf{r}_P	Coordinates of the proximal endpoint of segment i
\mathbf{r}_D	Coordinates of the distal endpoint of segment i

\mathbf{w}_i	Components of the lateral unitary direction vector of segment i
j	Marker index
$\mathbf{r}_{M_i^j}$	Coordinates of marker j of segment i
$\ddot{\mathbf{r}}_A$	Components of the acceleration vector
$\boldsymbol{\omega}$	Components of the angular velocity vector
$\tilde{\boldsymbol{\omega}}$	Skew matrix of angular velocity vector
$\boldsymbol{\Phi}^m$	Driving constraints
$\boldsymbol{\Phi}^k$	Kinematic constraints
$\boldsymbol{\Phi}^r$	Rigid-body constraints
f	Objective function
\mathbf{S}	Stiffness matrix
\mathbf{U}	Actual joint angles and displacements
\mathbf{U}_0	Neutral joint angles and displacements
\mathbf{F}	Actual forces and moments
\mathbf{F}_0	Neutral forces and moments
θ	Euler angle
θ_1	Extension/flexion angle(degree)
θ_2	Adduction/abduction angle (degree)
θ_3	Internal/external rotation angle (degree)
d	displacement
d_1	Lateral/medial displacement (mm)
d_2	Anterior/posterior displacement (mm)
d_3	Proximal/distal displacement (mm)

\mathbf{e}_1	First vector of knee joint coordinate system
\mathbf{e}_2	Second vector of knee joint coordinate system
\mathbf{e}_3	Third vector of knee joint coordinate system
rmse	Root mean square error
rmsd	Root mean square difference
r^2	Squared Pearson's correlation coefficient
sd	Standard deviation
b	Bias (mean value of data)
l	Limit of agreement ($b \pm 1.96sd$)
\bullet	Dot product
\times	Cross product

Note that the Anglo-Saxon notations are used with vectors and matrices in bold and scalar in italic.

Chapter 1. Introduction

1. Background and motivation

In a context of ageing of the population and of rising of life expectancy, and to address the different pathologies affecting the locomotor apparatus as well as performance of the movements, human locomotion is more than ever a major social concern. Human movement analysis consists in the observation and definition of movements of living humans and investigations in this domain are various. It addresses a multi-disciplinary community and is of interest in orthopedics, sports or everyday life. Biomechanics proposes to provide further scientific knowledge on the causes and effects of locomotion affections. In biomechanics, a motion is described as the ensemble of the positions and orientations of adjacent body segments determined at a sampled instant of time during the observation. In particular, kinematics is concerned with the study of movement from a geometrical point of view: it represents the first step toward dynamics which is concerned with what causes the body to move the way it does.

Assessing an accurate kinematics is therefore the critical baseline for movement analysis. Two main quantities that characterize the movement are interesting for the estimation of joint kinematics: the instantaneous bone pose, and the relative movement between adjacent bones. Generally, movement analysis is performed based on surface measurement data, such as stereophotogrammetry. Beyond the complexity of the mathematical representation of bone positions and orientations lies a major issue. It arises precisely when estimating the kinematics of internal structures using surface markers. Indeed, taking into account the error observed between the measured trajectories of the surface markers and the actual position and orientation of the underlying bone is necessary for an accurate estimate because the so-called soft tissue artefact (STA) can cause unrealistic motions of the joint. Accounting for this phenomenon remains an ongoing challenge ([Leardini et al., 2005](#)), preventing from a straightforward non-invasive measurement of the skeletal movement. Among various STA compensation methods, the use of a multi-body optimization (MBO) method was proposed as a potential solution ([Lu and O'Connor, 1999](#)), but did not end up with fully satisfying results so far.

2. Scope of the study

The thesis addresses prospects of improvement for the estimation of bone pose and joint kinematics using the MBO method. The principle of the method relies on the minimization of the least-square errors between the modeled and the measured skin marker trajectories, within a defined kinematic model embedding joint constraints. Some limitations of the MBO method are to be overcome.

First, a restriction associated to the stereophotogrammetry relies in that the movement analyzed must be performed in a controlled environment preventing from studying *in-situ* movements. The use of magneto-inertial measurement units (MIMUs) is therefore a trade-off, but since STA remains, the accuracy of the estimation of bone pose cannot be expected to be better than with stereophotogrammetry. Measurement from MIMUs can be implemented in the MBO framework to limit the STA propagation. The orientation computed from MIMUs has been successfully introduced within a MBO method to drive the kinematic model associated (Koning et al., 2015). However, in this first attempt, only the joint kinematics was evaluated against stereophotogrammetry and skin markers, not the position of the segments within the kinematic model. In particular, the position of the terminal segment is of great interest. Moreover, few details were provided on how to adapt the MBO framework to MIMU measurements. The model calibration is also critical in such a method: inappropriate calibration results in large tracking errors which propagate to the bone pose estimation.

Moreover, the MBO method relies on the hypothesis that the joint constraints introduced in the kinematic model represents the actual joint behavior. Nevertheless, the accuracy of such model-based methods is questionable, in particular because of the introduction of “hard” constraints that impede or prescribe the movement at the joint. Joint constraints can be considered as “hard” constraints when they have to be strictly satisfied, and as “soft” constraints when they have to be minimized. Evolving toward “soft” constraints, that are no longer deterministic, to model the joints may be an efficient alternative to represent the actual joint behavior better (Gasparutto et al., 2015). Finally, MBO only partially compensate for STA. STA models have been proposed (Alexander and Andriacchi, 2001; Bonci et al., 2014; Camomilla et al., 2013), applied only to single body optimization (Alexander and Andriacchi, 2001) and joint center estimation (De Rosario et al., 2013) so far. The complexity reduction of these models (Camomilla et al., 2015) are encouraging their use in the MBO method, and could be an alternative to a specific calibration for these models. In other words, a simultaneous identification of the parameters of a kinematic-driven STA model and bone pose estimation can be developed within the MBO framework.

3. Thesis outline

The chapters following this introduction are outlined as follow.

Chapter 2

In Chapter 2, a state-of-the-art on movement analysis is carried out with the aim of introducing general prerequisite on anatomy of the lower limb, acquisition system technologies, and methods for kinematics estimation. Chapter 2 explores the domain of motion analysis, from a biomechanical point of view, through a review of the literature, and identifies the main issues encountered while assessing joint kinematics. Arguments are advanced to legitimate the use of a MBO framework for bone pose estimation. The MBO method is presented in its classic version used for kinematic analysis for lower limb from marker-based stereophotogrammetry data (Lu and O'Connor, 1999), the method is detailed on the specific framework of natural coordinates (Dumas and Chèze, 2007). In particular, this chapter develops the joint models implemented in the kinematic model of the MBO methods, the soft tissue artefact issue, and the emerging magneto-inertial technology.

Chapter 3

In Chapter 3, a modeling framework is developed, derived from the classic MBO method, to make the method appropriate to the use of MIMUs, which represent a promising acquisition system in movement analysis. The developed method is used to investigate the feasibility of introducing orientation, angular velocity and acceleration derived from inertial sensors in the objective function of the MBO method as an alternative to the classic skin marker trajectories assessed from stereophotogrammetry. The developed method is tested on the lower limb for gait, aiming at comparing joint kinematics and foot position relative to the pelvis obtained by tracking MIMU and skin marker-based estimation. The hypothesis in this study is that performing an anatomical calibration (Picerno et al., 2008) is relevant for defining the kinematic model included in the MBO framework. Therefore, this study aims at evaluating the efficiency of a method which combine three proposed approaches for joint kinematics estimation: the MBO framework (Duprey et al., 2010; Lu and O'Connor, 1999), the MIMU-tracking approach (Koning et al., 2015) and the anatomical calibration procedure (Picerno et al., 2008).

Chapter 4

In Chapter 4, the performance of the MBO method to estimate knee joint kinematics is investigated when an elastic joint model based on the knee stiffness matrix is embedded in the framework. The stiffness matrix represents the mechanical behavior of a knee joint, but remains nevertheless

subject-dependent. A penalty-based method is implemented to introduce the elastic joint model as “soft” constraints in the MBO framework. Such a model at the knee joint is expected to provide better kinematics estimate than classic mechanical linkages (“hard” constraints) that impede or prescribe some displacements. Considering a single constant stiffness matrix, this evaluates the feasibility of the method compared to more classic methods (using spherical joint for instance). Furthermore, a sensitivity analysis is performed to investigate how variations of the stiffness matrix coefficients propagate to the kinematics estimation.

Chapter 5

In Chapter 5, a kinematic-driven STA model is introduced in the MBO method. Mathematical and computational developments are carried out using different types of kinematic and STA models to investigate the efficiency of the method in identifying the STA model parameters concurrently with estimating bone pose. The objective is to assess and compensate for the STA while improving the accuracy of the MBO method in estimating kinematics.

Chapter 6

Chapter 6 presents a general discussion of the studies described in this thesis. The main contribution of the work are underlined and some perspective are indicated.

Chapter 2. Literature review – state-of-the-art

This chapter offers basic as well as specific information required to understand the themes developed in the thesis. In particular, in order to understand the origins of movement, the reader must acquire basic knowledge about the anatomy of the human body. Anatomy provides essential information and terminology for musculoskeletal structures and joint motion. A preliminary paragraph presents an osteoarticular description of the lower-limb (particular attention is paid to the knee). After this introduction to anatomy from a modeling perspective, we explore the evolution of human motion analysis in history through the development of societal needs and measurement technologies. This historical overview leads to the interrogation about the potential alternatives to the marker-based approach in motion analysis. Then, we identify the problems tackled in the thesis work by investigating the open issues in motion analysis. Finally, bone pose and joint kinematics estimation method for the lower limb using multi-body optimization (MBO) is presented, as it will be the main framework used in this thesis. A special attention is paid to the classic joint models embedded in the multi-body biomechanical model.

1. Lower limb anatomy - osteoarticular description

1.1. Anatomical terminology

As a starting point, anatomy provides a common language of the human body and motion for understanding human body functions. This part aims to provide the bases to biomechanical studies through a descriptive definition of anatomical terms for the lower limb. The description is adapted to the needs of the thesis. The aim is to clearly communicate specific information about human body movements which requires specialized terminology for a precise identification of body positions and orientations.

1.1.1. Anatomical reference position

Anatomical reference position is the upward position from which human body is studied. Standing erect, face directing forward and palms of the hands facing forward, it is the position of reference in precisely designating site or direction of structures of the body. It is not a natural standing position but is the conventional orientation used as reference for posture and movement definition. In particular, it is commonly used in motion analysis for calibration procedures.

1.1.2. Directional terms

The anatomical terms of location are used to describe the relationship of body parts or external objects with respect to the body, each term (Table 2.1 on the left) has its corresponding antonym (Table 2.1 on the right):

Superior closer to the head	Inferior farther away from the head
Anterior toward the front of the body	Posterior toward the back of the body
Medial toward the midline of the body	Lateral away from the midline of the body
Proximal closer in proximity to the trunk	Distal at a distance from the trunk
Superficial toward the surface of the body	Deep inside the body and away from the body surface

Table 2.1 Directional terms

1.1.3. Anatomical reference planes

The anatomical planes are three imaginary cardinal planes that bisect the mass of the body in three dimensions. They allow the description of the body in its own regarding to a reference position. Body planes are commonly defined as follow (Figure 2.1):

- the **sagittal plane** (or anterior-posterior plane) is vertical and divides the body into left and right halves
- the **frontal plane** (or coronal plane) is vertical and divides the body into a front and a back
- the **transverse plane** (or horizontal plane) is horizontal and divides the body into a top and a bottom

In the anatomical reference position, all three planes intersect at a single point assumed to be the center of mass (or center of gravity).

1.1.4. Anatomical reference axis

The three anatomical axes associated with motion in each of the anatomical planes (Figure 2.1) defines the body reference coordinate system. Each axis is oriented perpendicular to one of the three planes of motion:

- the **medial-lateral axis** (or frontal-horizontal axis) is perpendicular to the sagittal plane.

- the **anterior-posterior axis** (or sagittal-horizontal axis) is perpendicular to the frontal plane
- the **longitudinal axis** (or vertical axis) is perpendicular to the transverse plane

These terms are used indifferently for the entire body or for a segment.

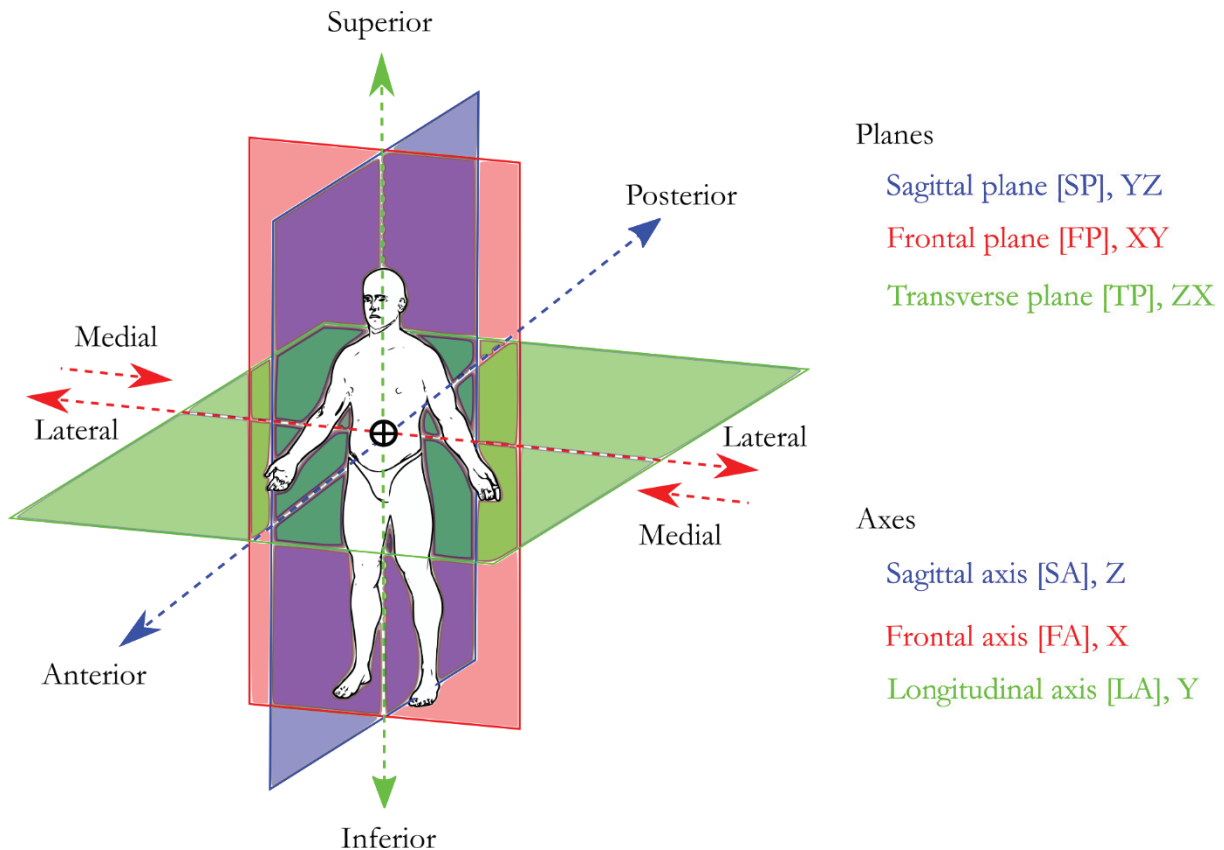


Figure 2.1 Anatomical planes and axes

1.1.5. Terms of movement for the lower limb

Flexion and extension occurs in the sagittal plane. **Flexion** generally refers to a movement that decreases the angle between a segment and its proximal segment. At the opposite, in the present work, **extension** refers to a movement that increases the angle between two body parts.

Abduction and adduction occurs in the frontal/sagittal plane. **Abduction** refers to a movement away from the midline. **Adduction** refers to a movement towards the midline.

Internal and external rotation (or medial and lateral rotation) occurs in the transverse plane, around the long axis of the segment.

These terms are used indifferently for the movements of a limb or a segment with respect to the body or for the movements of one distal segment with respect to the proximal one, that is to say the articular movements.

1.2. Human locomotor apparatus

The human body is a complex system the functioning of which relies on the multiple interaction between complementary biological structures. In particular, the musculoskeletal system, which groups passive (bones, ligaments, tendons) and active (muscles) elements, ensures the integrity of the body in supporting, maintaining, moving and protecting organs from fall or impact. Not only the skeleton is composed of 206 independent articulated bones, but also 630 skeletal muscles and 244 degrees of freedom (Paul et al., 2014) constituting the internal framework of the body with specific shape, structure and role, but also the redundancy of actuators offers plenty of combinations to perform a given movement. Human beings are different from the rest of the animal reign in that they adopt a bipedal station, which during evolution, engendered remarkable transformations to the whole body, in particular at a skeletal level (Lovejoy, 2005a, 2005b). Indeed, the straightening of the trunk created a unique situation for mammals, where the head, pelvis and feet are aligned vertically, elevating at the same time the center of mass. The lower limb's major role is the support of weight, adaptation to gravity and locomotion. The so-called human locomotor apparatus is composed of the two lower limbs (or legs) and the pelvis support the main part of body weight. Its schematic comportment is similar to an inverted pendulum whose lever arm is the length of the limb.

The direct consequence is the instability of such a system, requiring a perpetual control from the central nervous system. Focusing on the lower limb, instability is first due to the lever arm represented by the distance between the center of mass and the ground (e.g. inverted pendulum). In addition, the lower limb is poly-articulated, jeopardizing stability. Nevertheless, the body evolved brilliantly, solving the problem of instability at joint level in different manners depending on the role of the articulation.

1.2.1. Overview of the skeleton

The human locomotor apparatus is composed of three main type of organic structures: the osteoarticular system, the muscular system, the vascular and finally the nervous systems. The thesis work tackles the kinematics of the osteoarticular structures, without getting involved in the role of the muscular (or nervous) system.

At an osteoarticular level, the lower limb is composed of six main regions, linked to the lower portion of the lumbar spine through the pelvis. The pelvis is not included in the definition of the lower limb but its description is necessary to introduce the hip joint as the articulation between the torso and the leg. The soft tissues surrounding the skeleton are not specified in this description as they are not considered in kinematics analysis. That is to say that the kinematic analysis focuses only on the movement of the osteoarticular system. However, we will see further that, unfortunately, the soft tissues surrounding the skeleton play a role in motion analysis based on skin markers. The lower limb is divided in five regions (Figure 2.2) used to identify articulations and bony segments. We consider three articular regions: gluteal (hip joint), knee and ankle regions, and four segmental regions: gluteal (pelvis), thigh, shank and foot regions. Note that the gluteal region contains both the hip joint and the hip bone. The knee is composed of two articulations, the tibiofemoral and patellofemoral joints. As for the ankle, it includes the talocrural and talocalcaneal joints. The foot can be also divided in multiple articulations and bony segments. A detailed model of the foot will not be used in this thesis and, therefore, the corresponding anatomy is not presented.

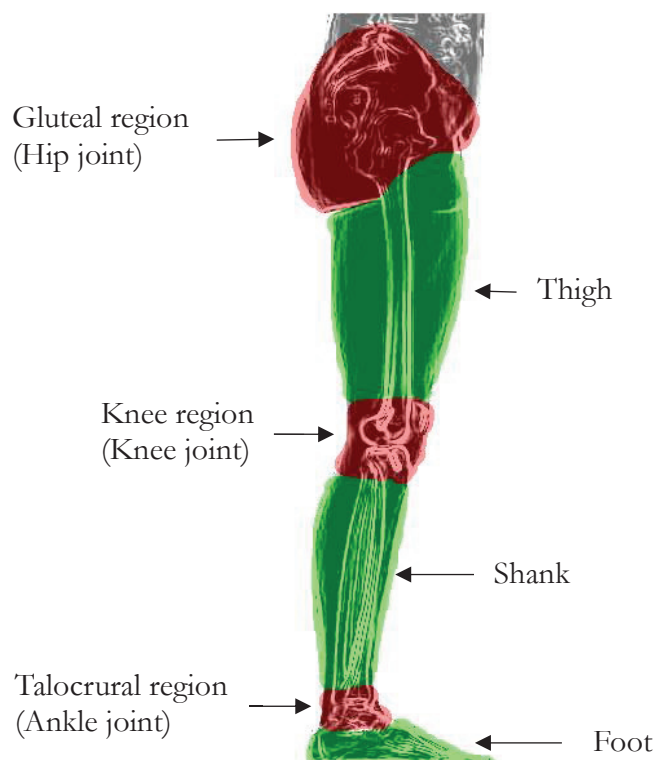


Figure 2.2 Lower limb overview

Among all biological structures composing the lower limb, we will focus our attention to the elements playing a passive role in movement, that is to say the skeleton and ligaments. We will develop a descriptive approach for the understanding of the subsequent work concentrating on the skeleton. Since a kinematic analysis does not require a complete and exhaustive anatomical description (e.g.; (Netter, 2010)), or functional anatomy (e.g.; (Kapandji, 2009)), a simplified phenomenological model will be proposed. The different kinematic models of the hip, knee and ankle joints will be presented in the next sections.

The human body, from an osteoarticular point of view is considered sagittal symmetrical for an asymptomatic subject. As a consequence, modeling is often developed with reference to one limb.

Bones

The previously mentioned lower limb skeleton (Figure 2.3) contains many bones, in particular in the foot. The following description focuses on the bones involved in the model developed for the thesis work. The objective was to reduce the skeletal model to a four body-segment articulated system: pelvis, thigh, shank, and foot.

1.2.1.a. Pelvis

The skeleton of the gluteal region is known as the pelvic girdle. It consists of the two symmetric iliac bones, the sacrum and the coccyx that represents the lower extremity of the spine (Dubousset, 1994) and thus, the coxofemoral joints between the iliac bones and the femurs represent the demarcation between upper and lower part of the body, better known as hip joint.

1.2.1.b. Thigh

The bony structures composing the thigh are the femur and the patella (that is not considered in this thesis work). The femur is articulated to the pelvis through the hip joint at its proximal end. The femur is the longest and most resistant bone of the human body. The proximal epiphysis is composed by three regions: the femoral head, which is a sphere covered with cartilage inserted in the pelvis acetabulum to form the hip joint, the femoral neck that links the femoral head to the diaphysis, and the greater (and smaller) trochanter insertion point for the hip muscles.

1.2.1.c. Shank

The leg region, named shank, is the part that lies between the knee region and the ankle region, the skeleton is composed of the tibia and the fibula, generally considered rigidly attached to each other, except in some complex 3D anatomical ankle joint models (Baldisserri and Parenti-Castelli, 2012) (see sections bellow) not used in motion analysis so far. Tibia is the second longest bone in the human body. Its proximal epiphysis is composed by the lateral and medial epicondyles, receiving

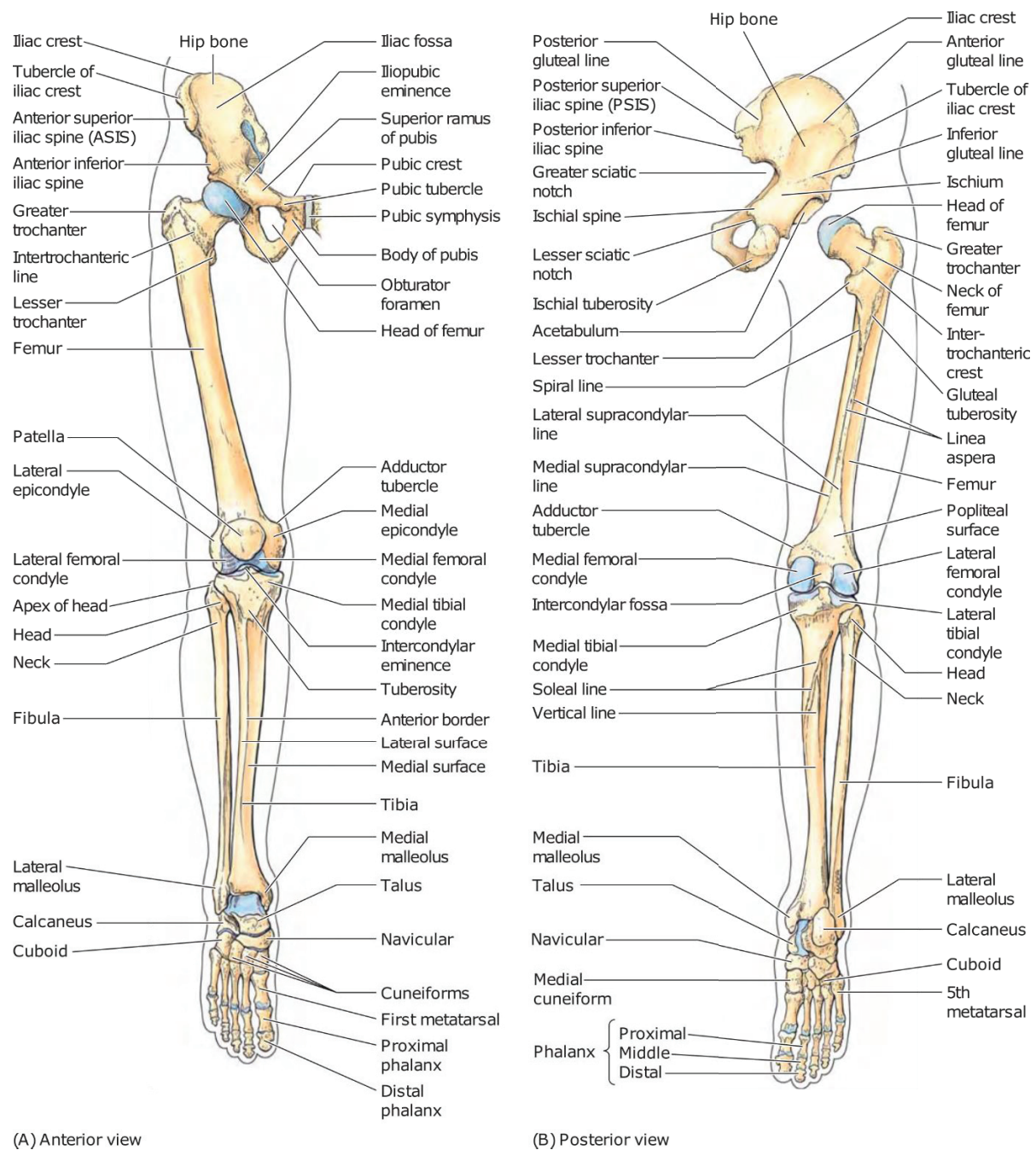


Figure 2.3 Skeletal framework of the lower limb (Moore and Dalley, 2006)

the femoral condyles, called tibial plateau. The distal epiphysis of the tibia contains the medial malleolus, and represents the supporting part of the ankle joint, while the distal part of the fibula, called lateral malleolus, is the second element of the articulation.

1.2.1.d. Foot

The foot is the most complex region of the lower limb, it contains 26 poly-articulated bones. The foot is composed of the tarsus, metatarsus and phalanges, though, it is considered as a rigid bony segment articulated with the shank at the ankle (talocrural) joint in the thesis work.

1.2.2. Joints of the lower limb

1.2.2.a. Structure

As previously mentioned, the lower limb contains multiple articulations between bones, in particular at the foot. Nevertheless it can be pictured as a system composed of three segments articulated by three main joints. All three hip, knee and ankle joints are synovial joints, or diarthrosis, which is the most common and complex type of joint in the body. The main characteristic of diarthroses consists in a joint cavity containing synovial fluid. This space between bones is delimited by the articular capsule, a fibrous capsule in continuity with the periosteum of the articulating bones, and the articular cartilage covering the articular surface of bones. Joints of the lower limb are mainly loaded in compression as they have a support function for the rest of the human body. The composition of joints is therefore adapted to high loads and generally the range of motion is reduced in favor of a better stability.

1.2.2.b. Hip joint

The hip or coxofemoral sacroiliac joint is the proximal joint of the lower limb, it is composed of the head of the femur and the acetabulum of the pelvis. Its ball-and-socket configuration makes it the most stable joint in the body, apparently easy to model because it exhibits articular surfaces that are close to spheres (Cereatti et al., 2010). The main role of the hip is the orientation of the lower limb in the 3 directions of space. The hip has three degrees of freedom. For an average asymptomatic subject the maximum hip range of motion is approximately as follow. In the transverse plane, maximum internal-external rotation angles are about 15° to 20°. When the knee is in extension, hip flexion angle is limited to 90° while it reaches up to 120° when the knee is flexed. Maximum extension is between 5° and 10°. Maximum abduction angle is about 45°, maximal adduction angle is up to 30°. No significant translation is allowed by the articulation (Kapandji, 2009). From a modeling perspective, the hip joint is classically modeled as a spherical joint (Stops et al., 2011).

1.2.2.c. Knee joint

The knee is the intermediate joint of the lower limb, it is the most complex joint in the body and is composed of the distal femur and proximal tibia. The knee is composed of two joints: the tibiofemoral articulation and the patellofemoral articulation. The patella is not considered in this

thesis work even if a 3D anatomical kinematic model of the patellofemoral articulation has been proposed (Sancisi and Parenti-Castelli, 2011). This kinematic model is mainly used for musculoskeletal modeling (Moissenet et al., 2014). The knee joint involves many biological structures of different nature. Focusing on the osteoarticular composition of the knee joint, it is mechanically defined with three rotations and three displacements. The mechanism of movement between femur and tibia is a combination of rolling and gliding. For an average asymptomatic subject maximum knee range of motion is approximately as follow. Flexion reaches up to 160° , when both knee and hip are flexed. Knee extension can be up to 5° , this posture of hyper-extension is reached in straight position when the knee is locked. In this particular case, internal-external rotation is null while, with the knee unlocked, it may be about 5° to 10° . Due to the asymmetry of the articular surfaces at the knee and ligament guiding, flexion-extension movement induces rotations and displacements that involve other degrees of freedom (DoFs), namely, internal rotation and anterior displacement of the tibia regarding to the femur during flexion. This coupling inducing up to 15° of internal rotation mainly appears during the first 20° of flexion. In opposition, anterior displacement about 20 mm of magnitude appears after the knee exceeds 20° of flexion (Kapandji, 2009).

From a modeling perspective, the knee can be represented by various mechanical linkages. First, we find the hinge joint (Andersen et al., 2009; Reinbolt et al., 2005), allowing flexion/extension in only one plane. Then, we find the spherical joint, probably the most common representation of the knee (Lu and O'Connor, 1999), allowing all rotational movements. These two models impede translation (spherical joint) and some rotations (hinge joint), providing in most of the cases quite an inadequate 3D representation of the physiological movement of the knee. Finally, 3D anatomical models (Duprey et al., 2009; Gasparutto et al., 2015) can be pictured as compound joints representing an assembly of simple mechanical linkages accompanied by more detailed anatomical knowledge like ligament insertion (Bergamini et al., 2011). These models generally allow most rotations and translations, while coupling the DoFs. In particular, the parallel mechanism (Figure 2.4) proposes a detailed mechanical model close to knee anatomy (Parenti-castelli et al., 2004). The use of such models has been reported to be a trade-off alternative in kinematics estimation (Duprey et al., 2010; Gasparutto

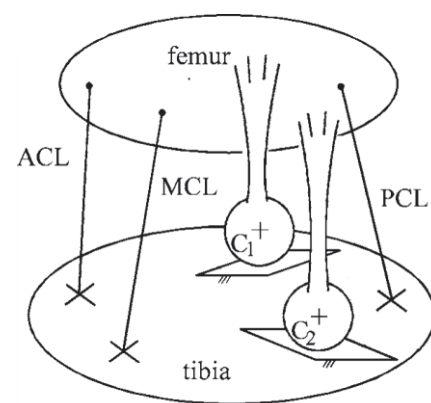


Figure 2.4 Example of 3D parallel mechanism for knee modeling (Parenti-castelli et al., 2004)

et al., 2015) in comparison to more classic models (spherical, hinge). But they still prescribe displacements in a deterministic way (i.e. kinematics is imposed by the geometry of the model).

1.2.2.d. Ankle joint

The ankle joint is composed of two joints, the talocalcaneal (subtalar joint) is formed by the articulation of the talus with the calcaneus. The talocrural (ankle) joint is commonly considered as hinge joint formed by the articulation of the distal tibia and fibula with the trochlea of the talus. The talocrural joint itself has only one degree of freedom, but the complex of the rear foot expands the mobility of the articulation procuring two degrees of freedom to the joint (Dettwyler et al., 2004). The bony process extending distally with respect to the medial tibia is referred to as medial malleolus. The lateral malleolus is the distal aspect of the fibula. The line passing through the malleoli represents the anatomical axis of flexion of the ankle. For an average asymptomatic subject the ankle movement is essentially a combination of two rotations about anatomical axis, it is commonly modeled as a universal joint. Maximal dorsi-flexion is about 20° and 45° , while plantar-flexion (extension) is between 30° and 50° (Kapandji, 2009).

From a modeling perspective, existing ankle models are similar to the knee models. For the ankle, we find spherical joints (Charlton et al., 2004; Lu and O'Connor, 1999), universal joints (Andersen et al., 2009; Reinbolt et al., 2005), and parallel mechanisms (Di Gregorio et al., 2007) (Figure 2.5).

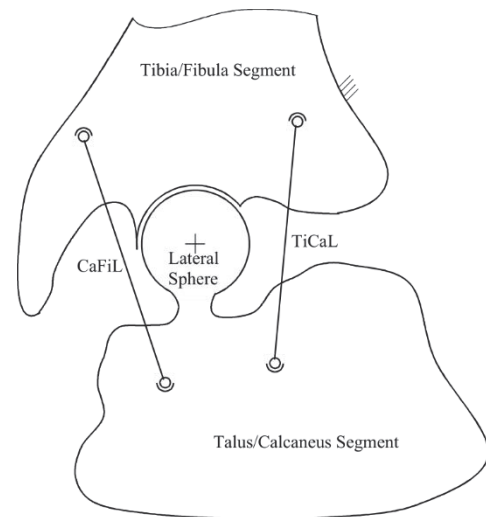


Figure 2.5 Example of 3D parallel mechanism for ankle modeling (Di Gregorio et al., 2007)

2. Motion analysis

2.1. History of movement analysis

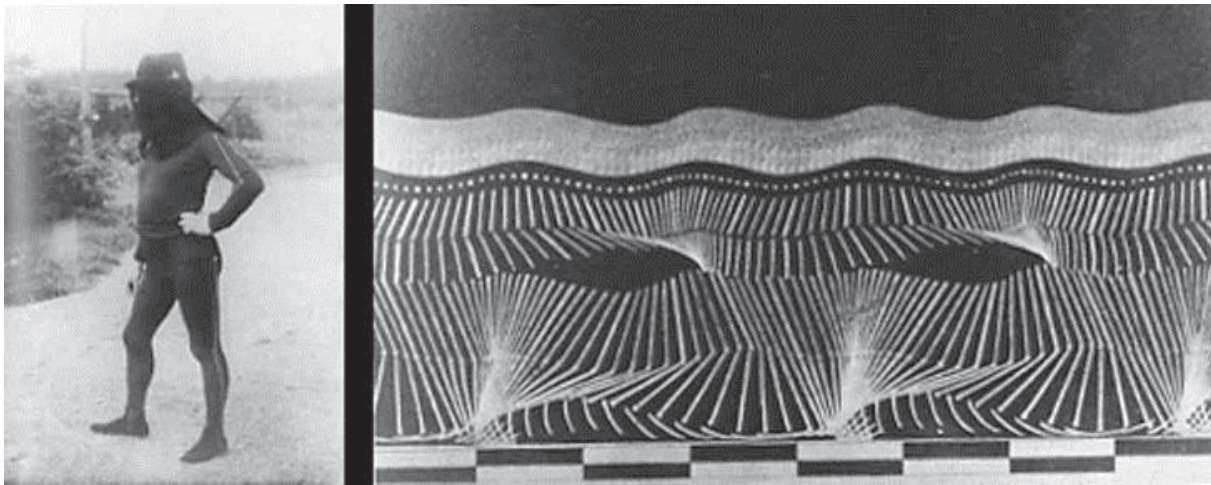


Figure 2.6 Movement analysis

Materialization of body segments by white lines on black coat from Etienne Jules Marey (1830-1904)

At the beginning, biomechanics of human and animal locomotion appeared with the willingness of exploring mechanical properties of living organisms. The objective was analyzing the relationship between structure and function, in other terms the causes and effects of structured biological materials constituting the body while evolving in its environment. In particular, a branch of biomechanics is devoted to the spatio-temporal variables pertaining to locomotion and posture characterization. The so-called motion analysis (or movement analysis) constitutes the first approach of biomechanics as a fully-fledged science (see (Baker, 2007) for a review on the early stages of gait analysis). A storytelling of modern research on the locomotor apparatus may probably begin with the names of Etienne-Jules Marey (1830-1904) (Marey, 1873) and Eadweard. Muybridge (1830-1904) (Muybridge, 1887). Indeed, while locomotion is a subject of examination since antiquity, for centuries observations remained qualitative. Animals were the first subjects of research, until Leonardo da Vinci who, defying restrictions with the first documented human dissection, collects fundamental information about human anatomy. Biomechanics is born, the link between external observations and internal structures can be seen from a mechanical point of view. Borelli (1608-1679) went a step forward with the first publication dealing with the scientific analysis of locomotion (Borelli, 1653). We have to wait until the XIXth century, with industrial revolution and contemporary wars raging in Europe that dedicated tools are created for locomotion analysis. Chronophotography (Marey, Muybridge), is the beginning of the technological development of

motion capture systems and more generally to the development of tools dedicated to motion analysis (Figure 2.6). The XXth century brought motion analysis in modern science, with the development of Fordism and Taylorism as best ambassador, not to mention the tragic needs engendered by the war for better performance, prosthetics and rehabilitation protocols. More recently, motion analysis technologies have been widely used for the development of animation movies and video games. To sum up, motion analysis, as a branch of biomechanics, is an interdisciplinary science that covers a large scope of applications like clinics (Lu and Chang, 2012), sports or animation to mention the most prominent. Obviously, in each domain, the needs and objectives are different, a research in motion analysis must be situated within a context that defines and justifies hypothesis, technologies and goals.

2.2. Issues in movement analysis

In studying human movement, one aims at describing the behavior of the different structures constituting the body, involved in the movement or posture. Motion analysis may provide reliable and objective data, in order to better understand the mechanics of musculoskeletal and osteoarticular systems, improve performance of athletes, or parameters on which clinical decision could properly rely. Motion analysis entails measurement, analysis and assessment of the biomechanical features that are associated with movement. Human motion analysis can be divided in three categories: detection of activity, body segment movement tracking, and skeletal movement analysis. For example, gait analysis is a common clinical test at this time, the applications of which include evaluation of disorders affecting the locomotion of individuals or the improvement of the performance of athletes.

Besides the importance of selecting the parameters adapted to the study, the question of data acquisition is critical. To this purpose, and in particular for clinics, a good tool for 3D motion analysis must be precise, accurate, valid, and not invasive. With the aim of performing an accurate 3D representation reflecting the actual mechanics, or at least kinematics, of the osteoarticular system, the specific quantification of parameters is necessary. Thanks to a constant effort in the improvement of precision and accuracy of measurement devices and technics, experimental acquisition systems are globally reliable (Chiari et al., 2005). Nevertheless, little information is available concerning the skeletal motion and the variables acquired by surface measurement are subject to various artefacts. For this reason, we will tackle the soft tissue artefact issue in a following part of this text.

While estimating the skeletal movement, the measured variables (marker trajectories, bone pose and geometry) are critical. For decades now, a widespread method to compensate for this bias relies

on the use of least-squares fitting to approach actual bone pose by biomechanical models involving joint models (multi-body optimization: MBO) or not (single-body optimization: SBO). Indeed, the main issue while assessing bone pose, is that the exact measurement of the skeleton is impossible without using pins inserted through the skin into the bone or using bi-plane medical imaging (see sections below).

2.3. Kinematics

Kinematics estimation concerns the description of the movement of a body without consideration of the cause of the activity. In other words, kinematics is the study of the relative and/or absolute position and orientation of bony segments that compose the moving body. Kinematics is the branch of biomechanics concerned with the study of movement from a geometrical point of view. Kinematics estimation aims at delivering angular and linear displacements occurring between two adjacent bones (or segments) at the articulation. To this purpose, the segments must be located in space in a global reference coordinate system (ICS: inertial coordinate system) through segment coordinate systems embedded in every single segment. Kinematics can be therefore concerned by the relative movement of adjacent segments on its own or by the movement of segments with respect to the global reference frame. The branch of biomechanics concerned with the causes of movement is kinetics (sometimes called dynamics). It aims at estimating joint forces and moments based on the kinematics and measurement of external variables associated to external loads (e.g.; force platform). Kinematics is therefore essential and represents the first step toward kinetics and, in a further step, musculoskeletal modeling. The thesis work is dedicated to the development of better kinematics estimators.

The variables estimated for the description of kinematics are time, position, displacement, velocity, and acceleration. Most of the kinematic study are limited to the use of time and position. Indeed, displacement, velocity and acceleration can be computed from time and position. Optical marker-based acquisition systems represent nowadays the most common motion analysis system since they are the best compromise between reliability, knowledge and cost.

Stereophotogrammetry: optoelectronic system

The measurement of human movement using stereophotogrammetry is widely used in professional and research domains. This term stands for all the techniques and methods that provide the

geometry/position of an object from at least two plane images recorded from different points of view. In biomechanics, this term is related to the optoelectronic systems based on multiple video camera recording (Figure 2.7). The principle is the same as for human vision: the faculty of perceiving objects in 3D by merging 2D images provided by the two eyes. Obviously, the precision and accuracy of this technique relies on the resolution of the video cameras as well as on the performance of the merging algorithm to manage the multiple sources of measurement.

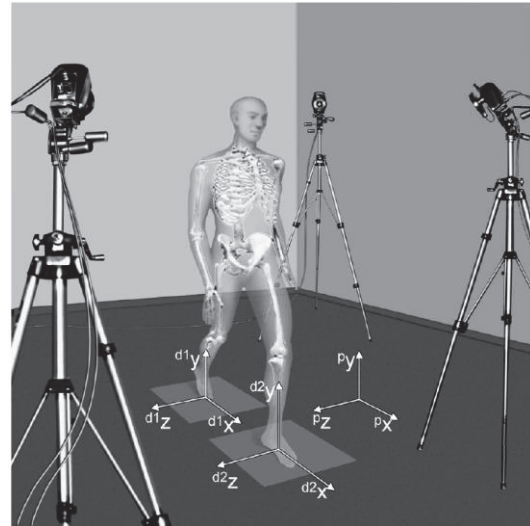


Figure 2.7 The human movement analysis laboratory. Stereophotogrammetric system (Cappozzo et al., 2005)

2.4. Dealing with skin markers – technological limitations

Until few years ago, the choice for ambulatory acquisitions of motion was limited to three main types of video-based technologies. As a direct evolution to the 2D analysis, the simplest systems are composed of two video cameras recording the moving subject in two planes (usually face and profile) (Braune, 1987). Whereas these video systems involve a very simple protocol and allow large outdoor field, manual digitization and post-processing are cumbersome and time consuming. Moreover, due to the low accuracy of trajectories, it is not adapted to a clinical analysis. Its use is basically limited to on-site athletes or animals movement analysis.

Improving dramatically the accuracy of spatial trajectories in real-time, we find systems based on active markers, whose markers contains the source that emit a signal to the sensor. Furthermore, post-processing is shorten by the automatic identification of markers. Nevertheless, the counterpart of these enhancements is that the sampling rate is inversely linked to the number of markers. In addition, markers, be they light emitting diodes or ultrasound emitters, are powered and cabled, limiting the capture volume.

With stereophotogrammetry, a compromise is made between accuracy, post-processing time and capture volume, by using passive markers that reflect light back to the sensors thanks to the retro-reflecting surface that covers them. The tracking of each individual marker is performed simultaneously by multiple video cameras. Infra-red or red light illuminators surround each camera lens and these lens receive the reflected pulses of infra-red light (or red light). Each camera record

a 2D image where markers appears as bright dots. The 3D position of every single marker is computed at the step of image processing (Figure 2.8), by fusion of the sets of 2D coordinates provided by each camera recording the same marker from different perspectives.



Figure 2.8 Motion capture workflow

Tracking and identification of individual marker trajectories may be quasi-automated. Theoretically, only two cameras are needed to perform the acquisition, but a minimum of 6 cameras is recommended to cover 360 degrees, due to the risk of occlusions from cameras or the crossing of marker trajectories.

To sum up, both active and passive marker systems require markers to be attached to the subjects and provide 3D coordinates of each marker. The main point encouraging the use of the stereophotogrammetric systems is that most of the studies are based on this technology, imposing it as a silver standard for motion analysis. Passive optoelectronic systems technology still present major issues, for instance, interferences due to camera lens distortion or markers occlusions and artefact can lead to an inaccurate estimation of the kinematics. Furthermore, the area of measurement is limited to controlled laboratory environment. Even if these acquisition systems present a satisfactory accuracy (Chiari et al., 2005), the latter mentioned issues are a limitation that cannot be overcome.

2.5. Soft tissue artefact

2.5.1. General characteristics of soft tissue artefact

Soft tissue artefact (STA) is a typical issue which reveals the complexity of studying living subjects in motion based on surface measurements. Actually, body surface markers, the positions of which are recorded by stereophotogrammetry, are distant from internal skeleton, separated by the soft tissues surrounding bones (muscles, fat and skin). The main causes of STA are skin sliding associated with joint movement, volumetric deformation of tissues due to muscle contraction, gravity and inertial effects (wobbling). As reported in the literature (Leardini et al., 2005), STA presents many characteristics that prevent from a straightforward compensation. For instance, STA is greater than instrumental errors associated to marker-based acquisition systems (Chiari et al., 2005); STA is task-dependent (Akbarshahi et al., 2010; Cappozzo et al., 1996), subject-specific (Benoit et al., 2006; Houck et al., 2004; Manal et al., 2000; Reinschmidt et al., 1997c), and marker

location-dependent (Akbarshahi et al., 2010; Cappozzo et al., 1996; Kuo et al., 2011; Ryu et al., 2009; Sati et al., 1996; Stagni et al., 2005; Tsai et al., 2011). STA introduces systematic and random errors and the frequency content of STAs is similar to the skeletal movement, preventing from filtering the signals (Chiari et al., 2005). As an example, during walking, the impact of STA on knee joint kinematics may be up to 8° for rotation and 18mm for displacements (Benoit et al., 2006). In this context, only the joint DoFs with large amplitude may be estimated with confidence, as the errors introduced by STA may be negligible with regard to the amplitude of the movement. Typically, for the knee, only flexion-extension angle estimation is reliable. STA concerns every single marker, each one has its proper movement, assumed unpredictable, with respect to the underlying bone. In other words, two phenomena are actually observed which characterize STA: from one part, the relative movement of markers one with each other; from another part, the relative movement between markers and the underlying bone (Andriacchi and Alexander, 2000; Leardini et al., 2005; Peters et al., 2010b). This phenomenon prevents from assessing the exact position and orientation of the skeleton during a movement task using external markers measurement, since bone pose and notably joint kinematics estimation are jeopardized by these inaccuracies. As a result, the optoelectronic systems only provide good estimation of movement of large amplitude, as hip, knee and ankle flexion/extension during gait. For this reason, and for years, many researches attempted to understand the patterns of STA and compensate for this phenomenon, but no satisfactory solution was found yet.

The amplitude of the STA differs depending on the study methods, the task performed, the segment concerned and the location of the marker on the segment. Pelvic STA amplitudes were reported to be about 17 mm (Hara et al., 2014). For markers located on the thigh, the STA has significant amplitude (Cappozzo et al., 1996), from 10 mm up to 40 mm. In the same study, authors demonstrated that markers on the tibia are less sensitive to STA (3 to 15 mm). STA on the foot is reported to be less important, between 1.8 mm and 4.3 mm (Tranberg and Karlsson, 1998). For many years and notably during the last decade, the number of studies on this topic has grown dramatically. Many studies (see (Peters et al., 2010b) for a review) give an overview of the complexity of quantifying the STA, and the literature reports quite different results.

2.5.2. Soft tissue artefact assessment and compensation

In the literature, numerous studies presented techniques for STA assessment and quantification. Unfortunately, the available information does not provide sufficient knowledge to propose a general description of the phenomenon. Indeed, the relevance of this knowledge was limited to a specific movement, the measurement system used to assess STA, the location of skin markers, etc... Anyway, STA assessment was performed by measuring trajectories of skin markers relative to the

actual skeletal movement. Literature provided patterns and magnitude of the relative distance variation of skin markers from reference positions. STA was assessed by different means on *in-vivo* or *ex-vivo* data. Techniques for assessing STA were based on the use of a set of skin markers subject to STA and a supplementary device used for the definition of the reference bone pose. This reference pose may be acquired using different methods. For instance, intracortical pins inserted in bones equipped with reflective markers (Andersen et al., 2012; Ball and Pierrynowski, 1998; Benoit et al., 2006; Camomilla et al., 2013; Houck et al., 2004; Lafortune et al., 1992; Ramsey et al., 2003; C. Reinschmidt et al., 1997a, 1997b) are assumed to provide the exact skeletal kinematics. It presents the advantage of a direct tracking of the motion using the same acquisition system as for skin markers. In reality, the results are significantly more reliable than the estimated kinematics from skin markers, but intracortical pins may cause discomfort, and there still remain some errors engendered by the pin bending, skin and muscle insertion sites anesthesia and deterioration, etc.... Moreover, they present ethical issues. Studies also reported the use of external fixators (Alexander and Andriacchi, 2001; Cappello et al., 1997; Cappozzo et al., 1996; Ryu et al., 2009); percutaneous systems (Hagemeister et al., 2005; Holden et al., 1997; Manal et al., 2000) and medical imaging (Akbarshahi et al., 2010; Barré et al., 2013; Sangeux et al., 2006; Tsai et al., 2011).

Different techniques have been proposed to compensate for STA (Alexander and Andriacchi, 2001; Andersen et al., 2009; Andriacchi et al., 1998; Ball and Pierrynowski, 1998; Cappello et al., 1997; Challis, 1995; Chèze et al., 1995; Dumas and Chèze, 2009; Duprey et al., 2010; Heller et al., 2001; Lu and O'Connor, 1999; Lucchetti et al., 1998; Soderkvist and Wedin, 1993). But the STA issue remains unsolved as there is no efficient model that entail the different specificities of the problem. The STA assessment related above provide quantities of information that may be exploited for a reliable STA characterization and modeling.

2.5.3. Modeling of soft tissue artefact

Compensating for STA is a widespread problem in motion analysis (Leardini et al., 2005). The goal of a STA model is to be implemented in a bone pose estimator, that will remove skin markers displacements from the reconstruction process, and thus to provide accurate reconstruction of the skeleton. It has been shown that incorporating a STA model is feasible in SBO (Alexander and Andriacchi, 2001), MBO (Richard et al., 2012) or algorithms based on a functional approach (De Rosario et al., 2013). An important characteristic to consider for an efficient mathematical STA model is the number of parameters embedded in the algorithm. This number must be as low as possible, and the calibration of the model parameters must be possible with non-invasive procedure. A STA mathematical model, driven by trial-specific variables has been proposed (Camomilla et al., 2013) considering markers at an individual level, but the high number of

parameters prevented from implementing the model in a bone pose estimator. The reduction of the number of parameters involved in the model to its minimum is necessary for the convergence of the bone pose estimator as well as for a reasonable computation time. Indeed, each parameter introduces a DoF that quickly lead to an under-determined problem.

While STA assessment may provide intrinsic properties of the phenomenon, it may be used for compensation and minimization of its impact on kinematics estimation. Amongst others, the STA model obtained by modal decomposition (Bonci et al., 2014; Camomilla et al., 2015; Dumas et al., 2014), or principal component analysis (Andersen et al., 2012) seems particularly promising. Indeed, STA field may be split into additive components (modes), the additional series of modes representing the STA can easily be truncated (in particular considering only the rigid transformation of the marker-cluster) with a proportion of the actual STA content depending on the selected modes constituting the model. Selecting adequate modes to describe STA involves a reasonable number of parameters to be optimized within the bone pose estimation while providing an acceptable approximation of STA. For instance, when using a modal decomposition based on principal component analysis, during gait, 4 principal modes represents up to 95% of STA (Andersen et al., 2012).

In Dumas et al. (Dumas et al., 2014) generalized mathematical representation of the STA is presented with three different possible definitions. STA can be defined considering the individual marker displacements relative to the segment coordinate system. (Akbarshahi et al., 2010; Camomilla et al., 2009; Cappozzo et al., 1996; Kuo et al., 2011; Sati et al., 1996; Stagni et al., 2005; Tsai et al., 2011). This definition is particularly suited when marker displacements and adjacent joint angles are quasi-linearly correlated (Akbarshahi et al., 2010; Camomilla et al., 2013; Cappozzo et al., 1996; Hara et al., 2014). However, it presents a large number of parameters and is computationally time consuming. A second STA definition considers the marker-cluster geometrical transformation that describes the phenomenon as rigid and non-rigid transformation of marker-cluster. This definition may include translation and rotation only (De Rosario et al., 2013; Sangeux et al., 2006; Südhoff et al., 2007); translation, rotation and isometric homothety (Challis, 1995; Horn et al., 1988) or rotation, translation, homothety and stretch (Ball and Pierrynowski, 1998; Dumas and Chèze, 2009; Grimpampi et al., 2014). Another definition of STA relies in the skin envelope shape variation involving a eigen decomposition (Dumas et al., 2009) or principal component analysis (Andersen et al., 2012). The present study proposed to implement models defined by marker-cluster geometrical transformations approach and, in particular, the rigid transformation of the marker-cluster. Indeed, it has been recently demonstrated that the rigid component of the STA not only represents the major part of the phenomenon (Andersen et al.,

2012; Barré et al., 2013; Benoit et al., 2015; De Rosario et al., 2012; Grimpampi et al., 2014) but is also the only artefact that affects (Dumas et al., 2015) the bone pose estimation within a Procrustes superimposition.

The finality of developing a STA model is its implementation into an optimal bone pose estimator, in order to minimize the effects of STA on the reconstruction. Very few studies actually propose a STA model designed for a further implementation in an optimal bone pose estimator. These models are based on a statistical approach to define STA (Alexander and Andriacchi, 2001; Camomilla et al., 2013). Moreover, the efficiency of a model dealing with rigid modes only has been shown for knee joint kinematics estimation during running (Camomilla et al., 2015). In the latter mentioned study, the STA translation and rotation components were obtained using a modal approach and embedded in a bone pose estimator. The calibration of the model for the thigh and shank was performed using the actual STA derived from intracortical pin data and skin markers trajectories. The study showed the efficiency of STA rigid component compensation on knee joint linear and angular kinematics while providing realistic STA for both thigh and shank. Nevertheless, since the calibration procedure was based on intracortical pin data, it is not applicable in routine experimental conditions where only skin-marker data are available. In this case, the model parameters must be estimated concurrently with the bone pose.

The study concluded in the relevance of approximating STA by its rigid components. The STA were well represented by the proposed model, improving the accuracy of the joint kinematics estimated after its removal from original dataset.

2.5.4. Conclusion

In recent years, methods have been proposed with the aim of compensating for STA (Leardini et al., 2005). Moreover, the modeling of STA is also a current topic (Andersen et al., 2012; Camomilla et al., 2009) and some models (however limited to Gaussian noise) have been embedded in single body optimizations (Alexander and Andriacchi, 2001). Different methods for compensation of STA are classified in four categories: least squares matching (SBO) e.g., (Andriacchi et al., 1998; Ball and Pierrynowski, 1998; Chèze et al., 1995), the multiple anatomical landmark calibration (Cappello et al., 2005; Cappozzo et al., 1995; Lucchetti et al., 1998), MBO method e.g., (Andersen et al., 2009; Duprey et al., 2010; O'Connor et al., 1998; Reinbolt et al., 2005; Sandholm et al., 2011; Scheys et al., 2011; Sholukha et al., 2006a; Stagni et al., 2009) and specific attachment systems (Hagemeister et al., 2005). Note that some of the compensation methods rely on modifying the experimental protocol while others are computational. The MBO method, a computational one, will be the main framework used in this thesis.

3. Alternative to stereophotogrammetry

Stereophotogrammetric systems demonstrate a satisfying accuracy for movement analysis, but their use is limited by their set-up time, capture volume and expertise requirements. Moreover, as stated above, surface measurements only give a biased estimation of the skeletal kinematics.

3.1. Medical imaging

Medical imaging groups several techniques, from the very first use of X-ray to assess internal *in-vivo* images to bi-planar fluoroscopy. This multitude of acquisition systems and image restitution of the human body relies on various physical phenomena: X-ray absorption, nuclear magnetic resonance, reflection of ultrasonic waves or radioactivity. Developed in medicine for diagnostic and therapeutic purposes, it is more and more affordable for research purposes, to better understand both anatomy and function of the human organism. The ultimate goal of medical imaging is to provide intelligible visual representation of internal information of a living subject with the smallest impact possible on the organism. Ideally, the result of an imaging system would provide an animated tri-dimensional reconstruction of the target system accompanied by the corresponding time dependent physical parameters. Medical imaging exists for a little bit more than a century, and a significant headway in the field has been made. Nevertheless, major limitations persists, particularly concerning the invasive character of these methods. Focusing on the 3-D reconstruction of bone pose and geometry, proposed technologies are based on four physical discoveries: X-ray, ultrasounds, magnetic field and radioactivity.

3.1.1. X-ray

Technologies based on X-rays (e.g., radiography, CT scan or fluoroscopy) relies on the capacity of X-rays to pass through the body exposed at a greater or lesser degree depending on its density. An emitting source of X-rays is placed in front of the segment and a receiver is placed in the back. Thus, the distinction between bones and soft tissues is allowed by the difference of photons received, rendering the absorption of the two components and so the density. Basically, radiography only provide 2D images in static position. The CT scan uses the same technology but allows a 3D acquisition thanks to the simultaneous rotation of the source and the receiver around the body and multiple axial images. The 3D reconstruction is processed in real-time from 2D images. For 3D reconstruction of human internal structures, a low-dose bi-planar radiography (EOS) was developed to reconstruct from two planes the whole body. The main limitations to the generalization of X-ray-based technology are the cost of such a system and it allows only static (radiography, bi-planar radiography) or low frequency dynamic acquisitions (fluoroscopy, bi-planar

fluoroscopy (Ackland et al., 2011)). Furthermore, depending on the dose and nature of the X-ray, it may be invasive and prevents from a systematic utilization.

3.1.2. Ultrasounds

Echography relies on the exploitation of the echo resulting from the exposure of tissues to an ultrasonic wave. The propagation of ultrasounds from the transducer (emitter and receptor) reflected by the structures of various density provide a 2D or 3D reconstruction of the structures. The main drawbacks are the questionable reliability when applied to a moving body and the repeatability. However, it is adapted to specific applications, for instance the estimation of hip joint center in static position (Peters et al., 2010a). Emerging methods also aim at tracking the position of the bone during movement by ultrasound and image registration based approach (Masum et al., 2014) or with dedicated ultrasound sensors (Kiss, 2010; Kiss et al., 2004).

3.1.3. Magnetism

From simple magnetic sensors to magnetic resonance imaging (MRI) or magnetic resonance spectroscopy (MRS), this technology must be used in a magnetic disturbance free environment. Classic magnetic sensors (e.g.; Flock of Birds (Ascension Technology Inc., Burlington, Vermont, USA), FastTrack (FastTrack, Polhemus, VT)) present nowadays little interest for clinical kinematics estimation, mainly for the fact that they often consist in superficial active markers using earth magnetic field, subject to magnetic interference. The use of magnetic tracking devices may be cumbersome and requires adapting the test set-up to the constraint imposed by such a device, preventing from using any ferromagnetic material. Many magnetic acquisition systems also embed active sensors with cable that limit the capture volume (for instance, they are used for *in-vitro* measurements (Hagemeister et al., 2002; Wong et al., 2005)). By contrast, MRI, is based on the use of nuclear magnetic resonance of water molecules. Eighty percent of the human body mass is water. MRI excites hydrogen contained in water to map in 3D the internal structures of the body, depending on their composition. It is nowadays the best way to identify bones, despite the fact that it may be invasive, in particular technologies based on ionizing radiation, and provides static information only. Still, MRI is widely used for the personalized characterization of knee osteoarticular structure parameters on which kinematics estimation relies (Freeman and Pinskerova, 2005) and has been tested for STA assessment (Sangeux et al., 2006).

3.1.4. Conclusion

While some of these technologies are relevant for clinical application, all of them therefore show one or more important limitations such as: the cost, the inability to record dynamic phenomena, the low frequency of acquisition, the questionable performance of registration and reconstruction

procedures, the difficulty of calibration or the small acquisition volume. For research purposes, they are used on a small panel of patients, and mostly employed for validation.

3.2. Magneto-inertial measurement units

In the context of exploration of non-invasive technologies for human movement analysis and surface measurement, magneto-inertial measurement units (MIMUs) (Fong and Chan, 2010) display high potential for quantitative evaluation of kinematics. Nowadays, joint kinematics estimation using MIMUs is not fully satisfactory, but for other applications both method and technology are mature enough as, for example, for locomotor performance assessment in athletes (Ahmadi et al., 2006), ambulatory measurement to monitor patients' daily activities (Favre et al., 2008, 2006; Kun et al., 2011; Liu et al., 2009), gait event detection (Clark et al., 2010; Cooper et al., 2009; Dejnabadi et al., 2005; Findlow et al., 2008; Hanlon and Anderson, 2009; Lau et al., 2008), identification of different daily activities (Chan et al., 2010; Coley et al., 2005).

3.2.1. Device description and specification

Technically, MIMUs entail three types of sensors: a 3D gyroscope, a 3D accelerometer and a magnetometer. The gyroscope provides a rate of turn (i.e., angular velocity); the accelerometer measures the linear acceleration, including gravity and the magnetometer measures a magnetic field, particularly sensitive to magnetic disturbance (Roetenberg et al., 2005). Those signals can be interpreted independently or by combination of the three information to compute orientation or position. Indeed, MIMUs, despite their ability to monitor ambulatory measurements, does not provide directly positions. The main issue when using MIMU for kinematic estimation is that the position of the MIMUs, and of segments, is unknown, only angular velocity, linear acceleration of the MIMU and the orientation of the magnetic source is provided. A first solution consists in performing the direct measurement of positions of each single MIMU during the movement, this imply the use of supplementary material such as GPS or stereophotogrammetry. Obviously, no significant benefit is brought to the method if optical systems are needed as the method combines most of drawbacks of both acquisition systems, it is therefore used for validation, and we will not confine on the use of GPS that is not precise enough for use in the context. A second solution, widely used, is to compute the positions of MIMUs. In practice, this is tantamount to compute position from the parameters provided by MIMUs, namely numerically integrating once the velocity or twice the acceleration. This numerical integration may be problematic in terms of reliability and consistency of results, mainly due to the bias of the measure such as drift of the gyroscope and the proclivity of numerical integration to propagate the errors. In the case of

kinematics estimation involving numerical integration, it is recommended to process signals through a fusion algorithm such as a Kalman filter (Kalman and others, 1960; Mazzà et al., 2012; Orgerie et al., 2008) which correct the numerical and measurement errors. For instance, the drift effect which affects the gyroscope signal when integrated (Luinge and Veltink, 2005; Picerno et al., 2011), and the measurement of the direction of magnetic north by the magnetometer allow to control and correct the absolute attitude of MIMUs against the vertical.

The first studies using MIMUs were conducted using hand-made combinations of uniaxial sensors mainly accelerometers (Willemssen et al., 1991, 1990). Then, different types of sensors were combined and miniaturized, leading to the development and commercialization of built-in units incorporating wireless motion trackers with a 3D gyroscope, 3D accelerometers, and, in some cases, 3-D magnetometers. The performance of MIMUs for movement analysis has been pointed out during the last decade (Sabatini, 2006). MIMUs overcome some of the drawbacks encountered when using stereophotogrammetry or ultrasound/ magnetic sensors. First, they are neither limited to a calibrated field of measurement nor in the movement performed. Indeed, most of MIMUs proposed nowadays are not cabled, so that they do not limit the amplitudes of movements. Furthermore, data loss encountered when occlusion occurs using optical systems are avoided since MIMUs are active sensors. First results on the estimation of joint kinematics using MIMUs compared to optoelectronic reference system are encouraging (Mayagoitia et al., 2002). A limit to the use of MIMUs remain for the high acceleration movement for whom the inertial effect on the sensors unit are critical.

Using MIMUs for locomotion analysis presents some benefits against stereophotogrammetry. The most interesting one is the ability of MIMUs to record a movement *in-situ*, the acquisition is not confined in a laboratory to the field covered by cameras. Inertial sensors have been employed for measuring movement of athletes performing sports movements in their environment of comfort (Chardonens et al., 2013; Kondo et al., 2012), it is use in detection of activities, for monitoring patients in everyday life, (Altun et al., 2010; Coley et al., 2005; Hanlon and Anderson, 2009), and for gait analysis in various environments (Cutti et al., 2010; Favre et al., 2008). Wireless technologies convincingly contributed to the growing interest of such devices. Furthermore, MIMUs are less expensive than classic optoelectronic systems. Focusing on the matter of the thesis work, the ease of use is particularly relevant for clinical application while estimating joint kinematics by the means of MIMUs.

Nevertheless, additionally to the fact they do not provide direct information on the position, MIMUs also entail disadvantages. First, the use of MIMUs embedding magnetometers may be treated with precaution since measures are dramatically influence by the surrounding magnetic

disturbance. As far as magnetometers uses magnetic north as reference for technical calibration and orientation of the device during the movement, the variations of magnetic reference induced by environmental disruption throughout the duration of the acquisition definitely introduce a bias to the results (Roetenberg et al., 2005). Unless not using magnetometers, this represents a limitation in the environment where to proceed to the measurement. A second issue lies in the fact that rate gyroscope actually provide the instantaneous angular velocity at each instant of time relatively to the previous one. The calibration phase for the determination of the initial orientations of MIMUs is therefore critical to estimate orientations of segments in the reference frame. Furthermore, MIMU sensor orientation is represented by a technical coordinate system expressed with respect to an earth-based global coordinate system. The latter global coordinate system is built from the measurement of gravity and magnetic north, provided by the accelerometer and the magnetometer, respectively (O'Donovan et al., 2007). It is common to all the MIMUs, but is generally different from a reference coordinate system defined using a stereophotogrammetric system for example. In any case, an appropriate calibration procedure is needed to define a segment coordinate system consistent with the technical coordinate system. The relation established during the calibration procedure between each MIMU technical coordinate system and the corresponding segment coordinate system may be assessed following four different procedures. A first method consist in positioning the MIMU in a segment so that both MIMU technical coordinate system and segment anatomical system are coincident. A second method consists in aligning all MIMUs technical coordinate system in measuring the subject in a reference static position. A third method consists in performing functional tasks to estimate functional axes for segment coordinate system definition. A last method, used in the present study consists in performing an anatomical calibration using a device, equipped with a supplementary MIMU, used to measure orientation of specific axes obtained by pointing anatomical landmarks. Measuring two reference axis in static position are sufficient to define the 3D orientation of the anatomical coordinate system. The definition of anatomical axes is used to compute the orientation matrix representing the transformation from the technical coordinate system to the anatomical coordinate system.

3.2.2. Soft tissue artefact

The use of MIMUs, as well as measurement from any external devices, including optoelectronic systems, is the relative movement between the skin and the underlying bone known as soft tissue artefact (Leardini et al., 2005). The study presented in the thesis dealing with MIMUs was not concerned in the direct compensation of STA. Nevertheless, all the results have to be considered with regard to this artefact. Actually, particular caution must be given in the case of high speed

movement involving high accelerations, MIMUs are significantly heavier than skin markers and inertial effects may be important.

4. Modeling and bone pose estimation – multi-body optimization

MBO was introduced with the aim of estimating bone pose of a system while limiting the effects of the soft tissue artefact (Andersen et al., 2009; Duprey et al., 2010; Li et al., 2013; Lu and O'Connor, 1999; Moniz-Pereira et al., 2014; Reinbolt et al., 2005; Sandholm et al., 2011; Scheys et al., 2011; Sholukha et al., 2006a; Stagni et al., 2009). The Procrustes method based on a minimization in the least squares sense is driven by skin marker trajectories and joint models. Originally introduced by Lu and O'Connor (Lu and O'Connor, 1999) with spherical joints, numerous studies attempted to improve estimates of the kinematics through the introduction of more physiological constraints (Duprey et al., 2010; Gasparutto et al., 2015). The following section is dedicated to the presentation of the MBO method, which is the central topic of the present thesis.

4.1. Rigid multi-body systems

A rigid multi-body system is an assembly of two or more articulated rigid body segments interconnected with idealized joints, which restraint the movement. In real systems, joints are not ideal which may undergo large translational and rotational displacements with, possibly, six degrees of freedom. Nevertheless, depending on the study, these joints are generally simplified and modeled by basic geometry keeping mobility on axes with large range of motion and prescribing or impeding the movement in other directions.

4.2. Parameter set and systems of coordinates

In this thesis work, bone pose is defined by means of natural coordinates (Dumas and Chèze, 2007; Dumas et al., 2012b; Duprey et al., 2010; Garcia De Jalon et al., 1994; Gasparutto et al., 2015) for computational expediency. Each body segment i is fully located and oriented through the vector $\mathbf{Q}_i = [\mathbf{u}_i \quad \mathbf{r}_{P_i} \quad \mathbf{r}_{D_i} \quad \mathbf{w}_i]^T$, where \mathbf{r}_{P_i} and \mathbf{r}_{D_i} are the position vectors of proximal (P_i) and distal (D_i) endpoints of the segment, and \mathbf{u}_i and \mathbf{w}_i are orientation vectors (Table 2.2, Figure 2.10), all vectors expressed in the global reference coordinate system (ICS: inertial coordinate system). All vectors may be noted $\mathbf{u}_i|_0$, $\mathbf{r}_{P_i}|_0$, $\mathbf{r}_{D_i}|_0$ and $\mathbf{w}_i|_0$ but this notation will be omitted for simplicity (i.e., natural coordinates are absolute coordinates by definition). The parameters of a multi-body

systems are concatenated in a single vector $\mathbf{Q} = [\mathbf{Q}_1 \ \mathbf{Q}_2 \ \mathbf{Q}_3 \ \mathbf{Q}_4]^T$, which stands for the design variables of the optimization. For the lower limb, $i=1,2,3,4$ stands for foot, shank, thigh and pelvis respectively (Figure 2.9).

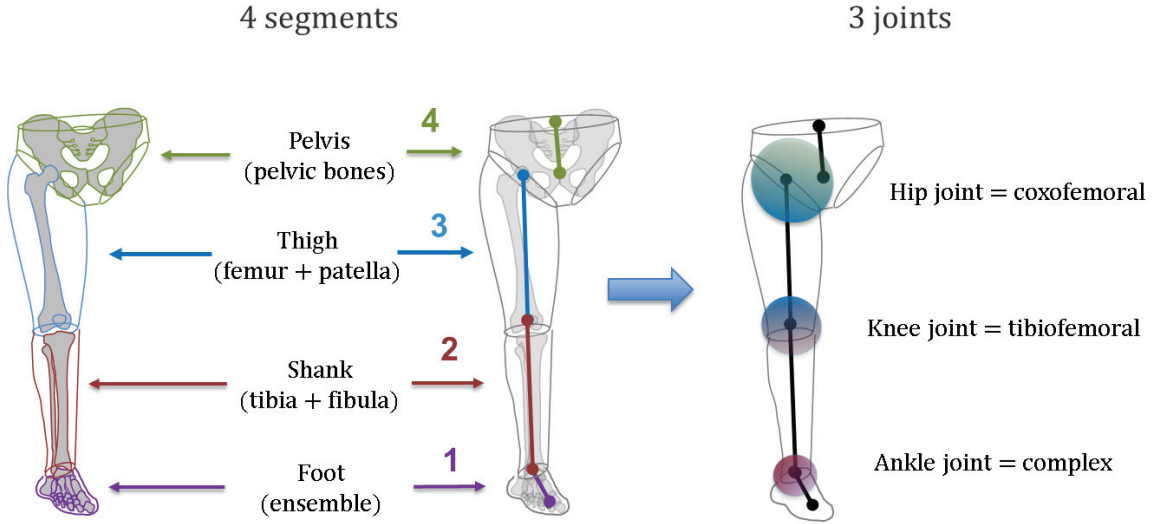


Figure 2.9 Representation of the lower limb

This parameterization and the associated non-orthogonal coordinate system $(P_i, \mathbf{u}_i, \mathbf{r}_{P_i} - \mathbf{r}_{D_i}, \mathbf{w}_i)$ (Dumas and Chèze, 2007) is particularly adapted to the MBO because it contains both anatomical and functional information. Indeed, the length of segment i is defined by $L_i = \|\mathbf{r}_{P_i} - \mathbf{r}_{D_i}\|$ while \mathbf{w}_i defines the axis of flexion of the distal joint and $(P_i, \mathbf{u}_i, \mathbf{v}_i = \mathbf{r}_{P_i} - \mathbf{r}_{D_i})$ defines the sagittal plane of the segment. The position of any point M can be expressed, for each segment i , in the global reference frame, $\mathbf{r}_i^M = \mathbf{N}_i^M \mathbf{Q}_i$, thanks to a constant interpolation matrix \mathbf{N}_i^M (Dumas and Chèze, 2007). By the way, natural coordinates contain redundant information as far as each segment pose is defined by 12 parameters for 6 degrees of freedom, additional constraints are mathematically necessary to solve the indeterminacy.

Segment	Parameter	Construction
Pelvis	\mathbf{r}_{P_4}	Midpoint between posterior iliac spines or lumbar joint center
	\mathbf{r}_{D_4}	Projection of point P_3 in the pelvis sagittal plane
	\mathbf{u}_4	From midpoint between anterior iliac spines to midpoint between posterior iliac spines.
	\mathbf{w}_4	Normal to the pelvis sagittal plane.
Thigh	\mathbf{r}_{P_3}	Hip joint center, estimated by regression (Dumas et al., 2007; Reed et al., 1999) or functionally (Ehrig et al., 2006)
	\mathbf{r}_{D_3}	Midpoint between medial and lateral epicondyles. Knee joint center.
	\mathbf{u}_3	Normal to the plane defined by point P_3 and medial and lateral epicondyles.
	\mathbf{w}_3	From medial to lateral epicondyle or functional axis of knee flexion/extension.
Shank	\mathbf{r}_{P_2}	$= \mathbf{r}_{D_3}$
	\mathbf{r}_{D_2}	Midpoint between medial and lateral malleoli. Ankle joint center.
	\mathbf{u}_2	Normal to the plane defined by the fibula's head and points P_2 and D_2
	\mathbf{w}_2	From medial to lateral malleolus.
Foot	\mathbf{r}_{P_1}	$= \mathbf{r}_{D_2}$
	\mathbf{r}_{D_1}	Midpoint between the 1 st and 5 th metacarpal head.
	\mathbf{u}_1	From calcaneus to D_1
	\mathbf{w}_1	From 1 st to 5 th metatarsi

Table 2.2 Description of segments parameters

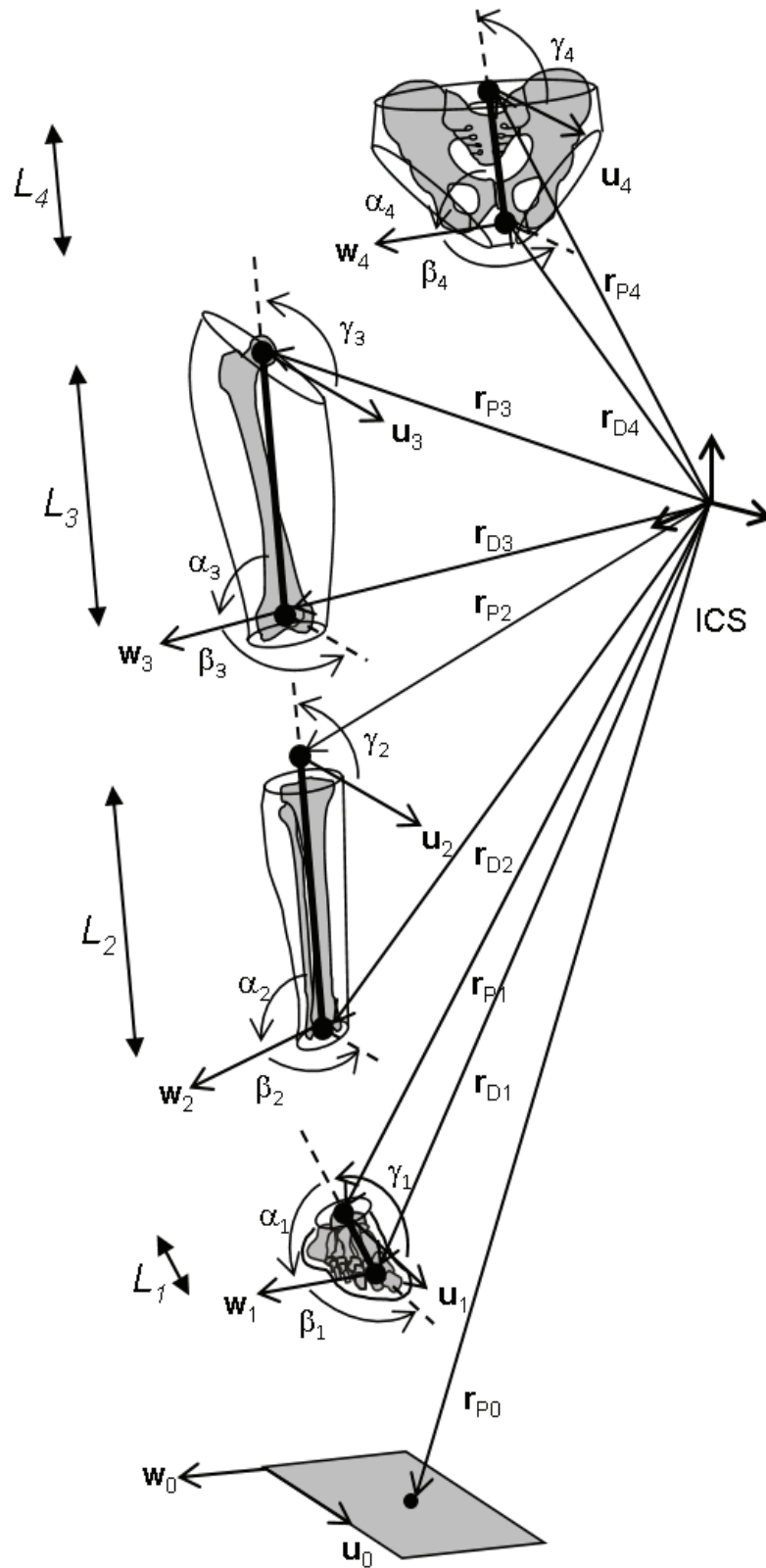


Figure 2.10 Segment parameters in the global reference frame (ICS)

4.3. Segment and joint coordinate systems

4.3.1. Segment coordinate system

The non-orthogonal segment coordinate system is first defined by one anatomical axis ($\mathbf{v}_i = \mathbf{r}_{P_i} - \mathbf{r}_{D_i}$: non-unitary vector in the direction of the long axis of the bone(s) for thigh and shank segments), one functional axis (\mathbf{w}_i : the unitary vector in the direction of the axis of flexion of the distal joint) and an axis normal to the frontal plane. The origin is defined at segment proximal endpoint P_i . By construction this coordinate system is not orthogonal. Second, the associated

orthogonal segment coordinate system $\left(P_i, \mathbf{X}_i|_0 = \mathbf{u}_i, \mathbf{Y}_i|_0, \mathbf{Z}_i|_0 = \frac{\mathbf{u}_i \times \mathbf{v}_i}{\|\mathbf{u}_i \times \mathbf{v}_i\|} \right)$ that conforms to the

ISB recommendation (Wu et al., 2002) is defined as:

$$\begin{bmatrix} \mathbf{X}_i|_0 & \mathbf{Y}_i|_0 & \mathbf{Z}_i|_0 \end{bmatrix} = \begin{bmatrix} \mathbf{u}_i & (\mathbf{r}_{P_i} - \mathbf{r}_{D_i}) & \mathbf{w}_i \end{bmatrix} [\mathbf{B}_i^{\text{uv}}]^{-1} \quad (2.1)$$

with

$$\mathbf{B}_i^{\text{uv}} = \begin{bmatrix} 1 & L_i \cos \gamma_i & \cos \beta_i \\ 0 & L_i \sin \gamma_i & \frac{\cos \alpha_i - \cos \beta_i \cos \gamma_i}{\sin \gamma_i} \\ 0 & 0 & \sqrt{1 - (\cos \beta_i)^2 - \left(\frac{\cos \alpha_i - \cos \beta_i \cos \gamma_i}{\sin \gamma_i} \right)^2} \end{bmatrix} \quad (2.2)$$

and with

$$\begin{cases} L_i = \sqrt{(\mathbf{r}_{P_i} - \mathbf{r}_{D_i})^2} \\ \alpha_i = \cos^{-1} \left(\frac{((\mathbf{r}_{P_i} - \mathbf{r}_{D_i}) \bullet \mathbf{w}_i)}{L_i} \right) \\ \beta_i = \cos^{-1} (\mathbf{u}_i \bullet \mathbf{w}_i) \\ \gamma_i = \cos^{-1} \left(\frac{(\mathbf{u}_i \bullet (\mathbf{r}_{P_i} - \mathbf{r}_{D_i}))}{L_i} \right) \end{cases} \quad (2.3)$$

The definition of the segment length and of the segment angles can be performed in a static position or averaged on several instants of time during the movement of interest.

4.3.2. Joint coordinate system

Joint coordinate systems are used to compute the kinematics of the joint, for each articulation, the conventions for axes and Euler sequence proposed by the ISB (Wu et al., 2002) are satisfied. The construction of orthogonal axes $\mathbf{X}_i|_0$, $\mathbf{Y}_i|_0$ and $\mathbf{Z}_i|_0$ is realized thanks to transformation matrices \mathbf{B}_i representing the expression of the vectors of the non-orthogonal coordinate systems in the segments coordinate system (Dumas and Chèze, 2007).

Joint kinematics is computed from the angular and linear displacements of the distal and proximal orthogonal coordinate systems. In this case, the origins are advantageously chosen at the distal point of the proximal segment and at the proximal point of the distal segment, extracted from the output estimates of the parameters \mathbf{Q} . Moreover, for this purpose, two segment coordinate systems are built for each segment, associated to the proximal and the distal joint respectively.

The computation of Euler angles following the selected sequence is possible in computing the rotation matrix of the proximal segment $i+1$ to the distal i segment coordinate system. For the hip joint and knee joints, the sequence for Euler angles is \mathbf{ZXY} , to get flexion-extension angle in first rotation θ_1 and internal-external rotation in third rotation θ_3 . The first axis \mathbf{e}_1 corresponds to the axis \mathbf{w}_{i+1} of the proximal segment (as the transformation from the non-orthogonal to the orthogonal segment coordinate systems yield $\mathbf{Z}_{i+1}|_0 = \mathbf{w}_{i+1}$), the third axis \mathbf{e}_3 generally corresponds to the axis \mathbf{v}_i of the distal segment (as the transformation from the non-orthogonal to the orthogonal segment coordinate systems yield $\mathbf{Y}_i|_0 = \mathbf{v}_i$ as long as γ_i is 90°), the second axes \mathbf{e}_2 (floating axis) corresponds to the cross product of \mathbf{e}_3 by \mathbf{e}_1 (Figure 2.11). The transformation matrix $\mathbf{B}_{i+1}^{\mathbf{wu}}$ is defined for the proximal segment $i+1$, so that the orthogonal segment coordinate

system $\left(D_{i+1}, \mathbf{X}_{i+1}|_0, \mathbf{Y}_{i+1}|_0 = \frac{\mathbf{w}_{i+1} \times \mathbf{u}_{i+1}}{\|\mathbf{w}_{i+1} \times \mathbf{u}_{i+1}\|}, \mathbf{Z}_{i+1}|_0 = \mathbf{w}_{i+1} \right)$ is built:

$$\mathbf{B}_{i+1}^{\mathbf{wu}} = \begin{bmatrix} \sin \beta_{i+1} & L_{i+1} \frac{\cos \gamma_{i+1} - \cos \alpha_{i+1} \cos \beta_{i+1}}{\sin \beta_{i+1}} & 0 \\ 0 & L_{i+1} \sqrt{1 - (\cos \alpha_{i+1})^2 - \left(\frac{\cos \gamma_{i+1} - \cos \alpha_{i+1} \cos \beta_{i+1}}{\sin \beta_{i+1}} \right)^2} & 0 \\ \cos \beta_{i+1} & L_{i+1} \cos \alpha_{i+1} & 1 \end{bmatrix} \quad (2.4)$$

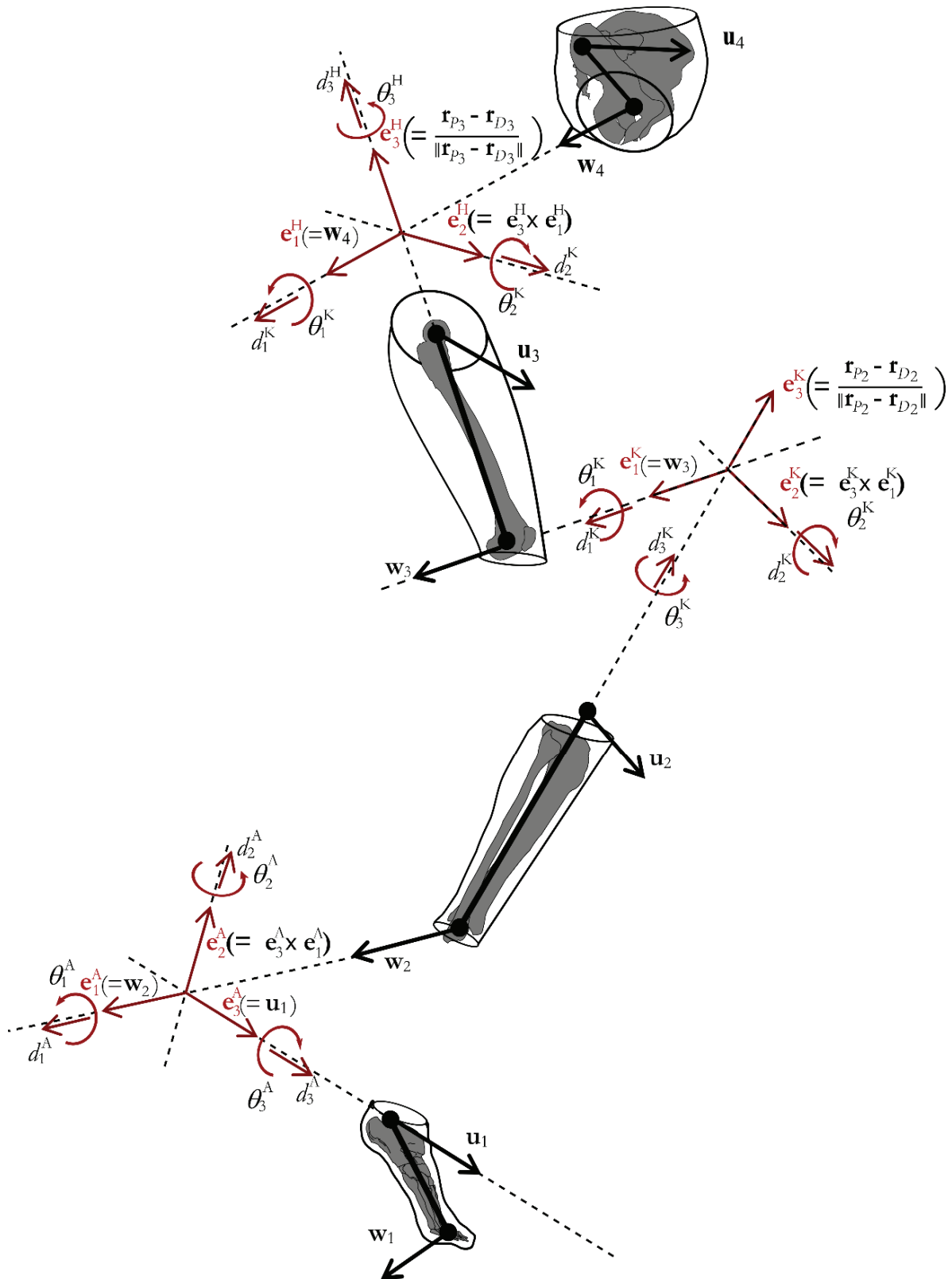


Figure 2.11 Joint coordinate system: hip (H), knee (K) and ankle (A), joint angles ($\theta_1, \theta_2, \theta_3$) and displacements (d_1, d_2, d_3)

The transformation matrix $\mathbf{B}_i^{\mathbf{uv}}$ as presented above is used for the distal segment. Then, the rotation matrix between proximal and distal segments is defined as follow (Dumas et al., 2012b):

$$\mathbf{R}_{i+1 \rightarrow i}(\theta_1, \theta_2, \theta_3) = \mathbf{B}_{i+1}^{\mathbf{wu}} \cdot \left(\begin{bmatrix} \mathbf{u}_{i+1} & (\mathbf{r}_{P_{i+1}} - \mathbf{r}_{D_{i+1}}) & \mathbf{w}_{i+1} \end{bmatrix} \right)^{-1} \cdot \begin{bmatrix} \mathbf{u}_i & (\mathbf{r}_{P_i} - \mathbf{r}_{D_i}) & \mathbf{w}_i \end{bmatrix} (\mathbf{B}_i^{\mathbf{uv}})^{-1} \quad (2.5)$$

Consequently, the Euler angles are defined as:

$$\theta_1 = \tan^{-1} \left(\frac{-\mathbf{R}_{12}}{\mathbf{R}_{22}} \right), \theta_2 = \sin^{-1}(\mathbf{R}_{32}), \theta_3 = \tan^{-1} \left(\frac{-\mathbf{R}_{31}}{\mathbf{R}_{33}} \right) \quad (2.6)$$

For the ankle, the sequence chosen for the kinematics is ZYX, to get flexion-extension angle in first rotation θ_1 and abduction-adduction in third rotation θ_3 . The first axis \mathbf{e}_1 still corresponds to the axis \mathbf{w}_{i+1} but the third axis \mathbf{e}_3 correspond to the axis \mathbf{u}_i of the distal segment (as the transformation from the non-orthogonal to the orthogonal segment coordinate systems yield

$\mathbf{X}_i|_0 = \mathbf{u}_i$) (Figure 2.11). In this case, another transformation matrix is defined for the proximal segment i , so that the orthogonal segment coordinate system

$\left(D_i, \mathbf{X}_i|_0 = \mathbf{u}_i, \mathbf{Y}_i|_{0i} = \frac{\mathbf{w}_i \times \mathbf{u}_i}{\|\mathbf{w}_i \times \mathbf{u}_i\|}, \mathbf{Z}_i|_0 \right)$ is built:

$$\mathbf{B}_i^{\mathbf{uw}} = \begin{bmatrix} 1 & L_i \cos \gamma_i & \cos \beta_i \\ 0 & L_i \sqrt{1 - (\cos \gamma_i)^2 - \left(\frac{\cos \alpha_i - \cos \gamma_i \cos \beta_i}{\sin \beta_i} \right)^2} & 0 \\ 0 & L_i \frac{\cos \alpha_i - \cos \gamma_i \cos \beta_i}{\sin \beta_i} & \sin \beta_i \end{bmatrix} \quad (2.7)$$

The rotation matrix between proximal and distal segments and the Euler angles are defined as follow:

$$\mathbf{R}_{i+1 \rightarrow i}(\theta_1, \theta_2, \theta_3) = \mathbf{B}_{i+1}^{\mathbf{wu}} \cdot \left(\begin{bmatrix} \mathbf{u}_{i+1} & (\mathbf{r}_{P_{i+1}} - \mathbf{r}_{D_{i+1}}) & \mathbf{w}_{i+1} \end{bmatrix} \right)^{-1} \cdot \begin{bmatrix} \mathbf{u}_i & (\mathbf{r}_{P_i} - \mathbf{r}_{D_i}) & \mathbf{w}_i \end{bmatrix} (\mathbf{B}_i^{\mathbf{uw}})^{-1} \quad (2.8)$$

$$\theta_1 = \tan^{-1} \left(\frac{\mathbf{R}_{21}}{\mathbf{R}_{11}} \right), \theta_2 = \sin^{-1}(-\mathbf{R}_{31}), \theta_3 = \tan^{-1} \left(\frac{\mathbf{R}_{32}}{\mathbf{R}_{33}} \right) \quad (2.9)$$

The linear displacements at the joint are the results of the non-orthogonal projection (Desroches, 2010; Pennock and Clark, 1990) on the three axis of the corresponding joint coordinate system of

the distance vector \mathbf{d} defined from the distal point D_{i+1} of the proximal segment to the proximal point P_i of the distal segment (Figure 2.11).

$$\mathbf{d} = \underbrace{\frac{(\mathbf{e}_2 \times \mathbf{e}_3) \cdot \mathbf{d}}{(\mathbf{e}_1 \times \mathbf{e}_2) \cdot \mathbf{e}_3}}_{d_1} \mathbf{e}_1 + \underbrace{\frac{(\mathbf{e}_3 \times \mathbf{e}_1) \cdot \mathbf{d}}{(\mathbf{e}_1 \times \mathbf{e}_2) \cdot \mathbf{e}_3}}_{d_2} \mathbf{e}_2 + \underbrace{\frac{(\mathbf{e}_1 \times \mathbf{e}_2) \cdot \mathbf{d}}{(\mathbf{e}_1 \times \mathbf{e}_2) \cdot \mathbf{e}_3}}_{d_3} \mathbf{e}_3 \quad (2.10)$$

with $\mathbf{d} = \mathbf{r}_{P_i} - \mathbf{r}_{D_{i+1}}$ and d_1 , d_2 and d_3 the joint displacements along the axis of the joint coordinate system.

4.4. Constraints

Three types of constraints are basically used in MBO, rigid body constraints Φ^r , joint (or kinematic) constraints Φ^k , and driving constraints Φ^m . The constraints are split in two sets of equations: a set of “soft” constraints contains the equations which are allowed to be violated (i.e., Φ^m) with the objective of minimizing the deviation between modeled and measured variables; a set of “hard” constraints contains the equations which must be satisfied (Φ^r) with the objective of null deviation between modeled and measured variables. Kinematic constraints Φ^k may be considered as “hard” or “soft” constraints.

4.4.1. Rigid body constraints

Equations referred as rigid body constraints stand for the assumption that body segments are non-deformable. Another way to interpret these constraints is that the parameters cannot be independent if they are more than 6 (for the six degrees of freedom). For instance, rigid body constraints will be the orthogonality of rotation matrix (Lu and O'Connor, 1999) or the normality of quaternion (sometimes referred as Euler parameters) vector (Andersen et al., 2009). Thus, using the natural coordinates, the rigid body constraints ensure a constant segment length and the conservation of the non-orthogonal coordinate system defined by vector \mathbf{Q}_i :

$$\Phi_i^r = \begin{cases} \mathbf{u}_i^2 - 1 = 0 \\ \mathbf{u}_i \cdot (\mathbf{r}_{P_i} - \mathbf{r}_{D_i}) - L_i \cos \gamma_i = 0 \\ \mathbf{u}_i \cdot \mathbf{w}_i - \cos \beta_i = 0 \\ (\mathbf{r}_{P_i} - \mathbf{r}_{D_i})^2 - L_i^2 = 0 \\ (\mathbf{r}_{P_i} - \mathbf{r}_{D_i}) \cdot \mathbf{w}_i - L_i \cos \alpha_i = 0 \\ \mathbf{w}_i^2 - 1 = 0 \end{cases} \quad (2.11)$$

As stated above, the definition of the segment length and of the segment angles can be performed in a static position or averaged on several instants of time during the movement of interest.

The rigid body constraints vector is:

$$\Phi^r = \begin{cases} \Phi_1^r \\ \Phi_2^r \\ \Phi_3^r \\ \Phi_4^r \end{cases} \quad (2.12)$$

4.4.2. Kinematic constraints

Joint constraints are the mathematical relations between two adjacent segments. They are supposed to prevent from non-physiological displacements and dislocation of joints. They are traditionally based on simple mechanical linkage and geometry. While minimizing the impact of STA, constraints implemented in the model also impose specific kinematic patterns (according to the mechanical linkage selected) to the joint. In the case of simple mechanical linkages (hinge, universal, spherical joint) (Figure 2.12), the accuracy of the model-based kinematics is questionable (Andersen et al., 2010a; Stagni et al., 2009).

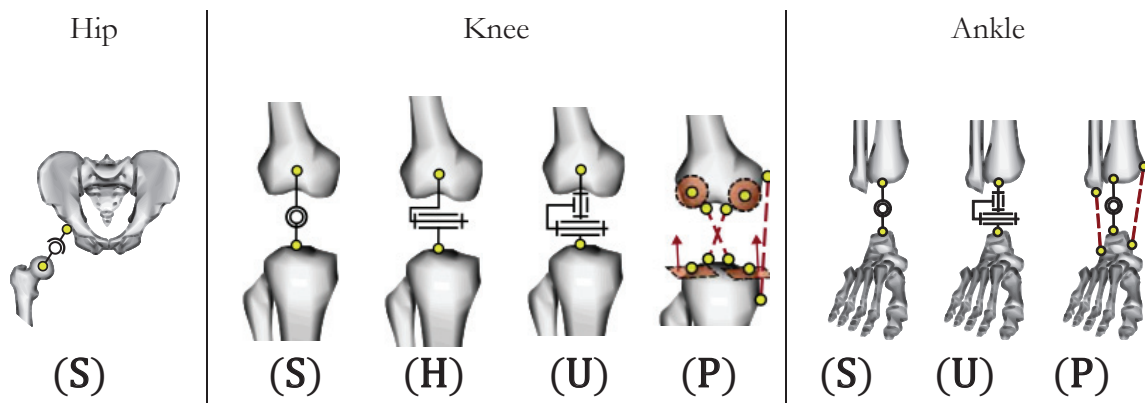


Figure 2.12 Classic joint models for the hip, the knee and the ankle.

Spherical joint (S), hinge joint (H), universal joint (U) and parallel mechanism (P).

More complex joints were proposed in order to better approaching physiological displacements, combining different basic linkage and involving ligaments (i.e., typically the parallel mechanisms presented in the sections above). Some authors also proposed to introduce some joint limits as inequality constraints (Fohanno et al., 2014). Nevertheless, this method introduces non-linear constraints, and was not used in the thesis work. The different types of classic joint constraints

implemented in the study are presented in the following part. Classic joint models are generally based on “hard” (deterministic) constraints as opposed to “soft” constraints when a penalty method is used. It must be mentioned that the specific case where MBO does not embed kinematic constraints is the so-called SBO.

4.4.2.a. Spherical joint

Spherical joint model is defined by three rotations, it is used in the literature for modeling hip, knee and ankle joints. However, this representation particularly suits to the hip joint (Cereatti et al., 2010). Indeed, it is widely used (Andersen et al., 2009; Charlton et al., 2004; Lu and O’Connor, 1999; Reinbolt et al., 2005). It is also the model historically introduced in MBO for knee and ankle, even if more sophisticated joint models are preferred at this time. For ankle and knee, spherical joint constraints are:

$$\Phi_{A,K}^k = \mathbf{r}_{D_i} - \mathbf{r}_{P_{i-1}} = \mathbf{0} \quad (2.13)$$

For the hip constraints are:

$$\Phi_H^k = \mathbf{N}_4^{V_4^1} \mathbf{Q}_4 - \mathbf{r}_{P_3} = \mathbf{0} \quad (2.14)$$

with V_4^1 the hip joint center in the pelvis and $\mathbf{N}_4^{V_4^1}$ the corresponding interpolation matrix.

4.4.2.b. Hinge joint

Hinge joint is used for modeling knee (Andersen et al., 2009; Duprey et al., 2010; Reinbolt et al., 2005).

For the knee joint the constraints are:

$$\Phi_K^k = \begin{cases} \mathbf{r}_{D_{i+1}} - \mathbf{r}_{P_i} = \mathbf{0} \\ \mathbf{w}_{i+1} \bullet (\mathbf{r}_{P_i} - \mathbf{r}_{D_i}) - L_i \cos \varphi_K^1 = 0 \\ \mathbf{w}_{i+1} \bullet \mathbf{u}_i - \cos \varphi_K^2 = 0 \end{cases} \quad (2.15)$$

where φ_K^1 and φ_K^2 are two constant angles defining the orientation of the hinge with respect to the thigh segment.

4.4.2.c. Universal joint

Universal joint is used for modeling ankle joint (Andersen et al., 2009; Duprey et al., 2010; Reinbolt et al., 2005).

For the ankle constraints Φ_A^k are:

$$\Phi_A^k = \begin{cases} \mathbf{r}_{D_2} - \mathbf{r}_{P_1} = \mathbf{0} \\ \mathbf{w}_2 \bullet \mathbf{u}_1 - \cos \varphi^A = 0 \end{cases} \quad (2.16)$$

where φ^A is the constant angle of the universal joint for the ankle. In the model the angle φ^A can be arbitrarily set to 90° or to β_2 if we assume the axis \mathbf{u}_1 and \mathbf{u}_2 aligned in neutral position. The angle can also be derived from natural coordinates \mathbf{Q} giving $\varphi^A = \cos^{-1}(\mathbf{w}_2 \bullet \mathbf{u}_1)$ where \mathbf{w}_2 and \mathbf{u}_1 are computed in a single sample of time in static position (e.g., in neutral position) or computed for all samples of time during the movement. In this case, taking the mean value $\bar{\varphi}^A$ is similar to the “solidification” procedure (Chèze et al., 1995) in static or dynamic analysis.

4.4.2.d. Parallel mechanism

For the parallel mechanism at the knee (Duprey et al., 2010), the joint constraints Φ_K^k are:

$$\Phi_K^k = \begin{cases} \left(\mathbf{N}_3^{V_3^1} \mathbf{Q}_3 - \mathbf{N}_2^{V_2^6} \mathbf{Q}_2 \right) \mathbf{N}_2^{n_2^3} \mathbf{Q}_2 - l_1^K = 0 \\ \left(\mathbf{N}_3^{V_3^2} \mathbf{Q}_3 - \mathbf{N}_2^{V_2^7} \mathbf{Q}_2 \right) \mathbf{N}_2^{n_2^4} \mathbf{Q}_2 - l_2^K = 0 \\ \left(\mathbf{N}_3^{V_3^3} \mathbf{Q}_3 - \mathbf{N}_2^{V_2^8} \mathbf{Q}_2 \right)^2 - \left(l_3^K \right)^2 = 0 \\ \left(\mathbf{N}_3^{V_3^4} \mathbf{Q}_3 - \mathbf{N}_2^{V_2^9} \mathbf{Q}_2 \right)^2 - \left(l_4^K \right)^2 = 0 \\ \left(\mathbf{N}_3^{V_3^5} \mathbf{Q}_3 - \mathbf{N}_2^{V_2^{10}} \mathbf{Q}_2 \right)^2 - \left(l_5^K \right)^2 = 0 \end{cases} \quad (2.17)$$

With $\mathbf{N}_i^{V_i^j}$ and $\mathbf{N}_i^{n_i^j}$ constant interpolation matrices defining the positions and orientations of the different anatomical features (e.g., center of femoral condyles, orientation of tibial plateau) and l_j^K constant distances.

We find also two different parallel mechanism for the ankle (Di Gregorio et al., 2007), the model presented hereby (Dumas et al., 2012a) is composed of 3 constraints representing a spherical joint and 2 isometric ligaments, the joint constraints Φ_A^k are:

$$\Phi_A^k = \begin{cases} \left(\mathbf{N}_2^{V_2^1} \mathbf{Q}_2 - \mathbf{N}_1^{V_1^1} \mathbf{Q}_1 \right)^2 = 0 \\ \left(\mathbf{N}_2^{V_2^2} \mathbf{Q}_2 - \mathbf{N}_1^{V_1^2} \mathbf{Q}_1 \right)^2 - \left(l_A^2 \right)^2 = 0 \\ \left(\mathbf{N}_2^{V_2^3} \mathbf{Q}_2 - \mathbf{N}_1^{V_1^3} \mathbf{Q}_1 \right)^2 - \left(l_A^3 \right)^2 = 0 \end{cases} \quad (2.18)$$

with $\mathbf{N}_i^{V_i^j}$ the interpolation matrices defining the positions of the different anatomical features and l_A^j constant distances.

4.4.3. Driving constraints

Driving constraints Φ^m consist of distances between measured skin marker positions obtained by an optoelectronic system and positions calculated from the multi-body model made of segment and articulated joints (represented by a set of constraints Φ^k and Φ^r). The position of the computed model-determined markers correspond to the fixed position of markers in the segment coordinate system, computed from a static position (or any specific frame of the movement) or averaged on several instants of time during the movement of interest, just like the segment length and angles.

The objective function f is the sum of the square distances between measured and model-determined marker trajectories:

$$f = \sum_{i=1}^4 \sum_{j=1}^{m_i} \left(\mathbf{r}_{M_i^j}^{\wedge} \Big|_0 - \mathbf{N}_i^{M_i^j} \mathbf{Q}_i \right)^2 \quad (2.19)$$

with m_i the number of skin markers embedded in segment i and where \wedge denotes a variable measured by stereophotogrammetry as opposed to the modeled one (obtained by interpolation matrix). The distance between measured and model-determined markers M_i^j is concatenated in the vector of driving constraints Φ^m . The objective function becomes:

$$f = \frac{1}{2} (\Phi^m)^T \Phi^m \quad (2.20)$$

with

$$\Phi^m = \begin{cases} \mathbf{r}_{M_1^1}^{\wedge} \Big|_0 - \mathbf{N}_1^{M_1^1} \mathbf{Q}_1 = \mathbf{0}_{3 \times 1} \\ \vdots \\ \mathbf{r}_{M_1^{m_1}}^{\wedge} \Big|_0 - \mathbf{N}_1^{M_1^{m_1}} \mathbf{Q}_1 = \mathbf{0}_{3 \times 1} \\ \vdots \\ \mathbf{r}_{M_4^1}^{\wedge} \Big|_0 - \mathbf{N}_4^{M_4^1} \mathbf{Q}_4 = \mathbf{0}_{3 \times 1} \\ \vdots \\ \mathbf{r}_{M_4^{m_4}}^{\wedge} \Big|_0 - \mathbf{N}_4^{M_4^{m_4}} \mathbf{Q}_4 = \mathbf{0}_{3 \times 1} \end{cases} \quad (2.21)$$

Here, particular attention should be drawn to the model-based marker positions $\mathbf{N}_i^{M_i} \mathbf{Q}_i$. The interpolation matrix actually represents the calibration procedure from anatomical to technical coordinate systems.

Some authors proposed to introduce weighting factors to the objective function, assigning to each marker a different weight in the solution. These weighting factors can be pictured as the error distribution among markers (Ausejo et al., 2011; Lu and O'Connor, 1999). The choice was made in this thesis work to use the same weight for all markers.

4.5. Optimization

MBO consists in the minimization in least-squares senses of the sum of squared distances. The algorithm involves rigid body constraints and kinematic constraints (except in the special case of SBO), the design variables are the bone pose parameters, \mathbf{Q} .

4.5.1. Formulation of the problem

In the present studies, the problem is solved frame by frame with a quasi-static approach. For MBO, in addition to rigid body constraints, the minimization is subject to kinematic constraints. Both rigid body and kinematic constraints are deterministic constraints, the problem can be reduced to the resolution of the following system:

$$\begin{aligned} \min_{\mathbf{Q}} f &= \frac{1}{2} (\Phi^m)^T \Phi^m \\ \text{subject to } &\begin{cases} \Phi^k = \mathbf{0} \\ \Phi^r = \mathbf{0} \end{cases} \end{aligned} \quad (2.22)$$

with

$$\Phi^k = \begin{cases} \Phi_A^k \\ \Phi_K^k \\ \Phi_H^k \end{cases} \quad (2.23)$$

Again, in the specific case of SBO, the problem only involves rigid body constraints.

4.5.2. Lagrangian formulation

The use of natural coordinates presents the advantage to yield linear or quadratic Jacobian matrices for the driving, rigid and kinematic constraints. Thus, the use of Lagrange formulation for the resolution (Andersen et al., 2009) is particularly adapted to the problem.

The problem becomes the zero search of the function \mathbf{F} :

$$\mathbf{F} \begin{pmatrix} \mathbf{Q} \\ \lambda \end{pmatrix} = \begin{pmatrix} [\mathbf{K}^m]^T (\Phi^m) + \begin{bmatrix} \mathbf{K}^k & \mathbf{0} \\ \mathbf{0} & \mathbf{K}^r \end{bmatrix}^T \begin{pmatrix} \lambda^k \\ \lambda^r \end{pmatrix} \\ \Phi^r \end{pmatrix} \quad (2.24)$$

with $\mathbf{K}^m = \frac{d\Phi^m}{d\mathbf{Q}}$, $\mathbf{K}^k = \frac{d\Phi^k}{d\mathbf{Q}}$ and $\mathbf{K}^r = \frac{d\Phi^r}{d\mathbf{Q}}$ the Jacobian matrices of the constraints and λ^k

and λ^r the Lagrange multipliers associated to the kinematic and rigid body constraints respectively.

For computational purpose, using a Gauss-Newton algorithm is judicious for the resolution, requiring the differentiation of the previous equation (2.24) regarding to \mathbf{Q} and λ .

Chapter 3. Multi-body optimization using magneto-inertial measurement units

1. Introduction

As already mentioned in Chapter 2, the MBO method classically estimates the lower limb joint kinematics from marker-based stereophotogrammetry. There is a need for a more flexible device than stereophotogrammetry when monitoring ambulatory measurement. This chapter addresses the feasibility of using magneto-inertial measurement units (MIMUs) as an alternative to stereophotogrammetry and skin markers to assess bone pose and joint kinematics of the lower limb. Recently, an original approach has been proposed using the orientation of MIMUs (Koning et al., 2015) in the objective function of the MBO method instead of marker trajectories. The model calibration (segment lengths, position and orientation of the MIMUs with respect to the segments) is central in such method and was not detailed in the original approach (Koning et al., 2015). In other words, inappropriate calibration may result in high tracking errors (that is to say objective function residual) and inaccurate estimation of the position of the segments. Another study investigated on the fusion of MIMU signals for use in a multi-body system of equations (Torres-Moreno et al., 2016), a robotic planar four-bar linkage system was equipped with MIMUs which signals were processed by the means of Kalman filters to estimate kinematics and dynamics as well as positions. In the latter mentioned study, the use of advanced fusion algorithms merging the three types of signals provided by the MIMUs is proposed to compensate for the measurement errors. The method used in the present study has been developed for MIMUs consisting of a 3D gyroscope, a 3D accelerometer and a 3D magnetometer. Such MIMUs are commercialized with a software support that collects the raw rate of turn, namely angular velocity, measured by the gyroscopes, the raw linear acceleration measured by the accelerometers, both signals are expressed in the technical coordinate system of the device, and the raw magnetic field measured by the magnetometers. Furthermore, the software also provides pre-processed signals resulting from the filtering and smoothing of the raw data. Finally, the software provides an estimate of the orientation of the MIMUs in the earth-based global coordinate system thanks to a Kalman filter.

Our hypothesis is that the use of the anatomical calibration procedure (Picerno et al., 2008) is an adequate procedure for defining the kinematic model included in the MBO framework. This study aims at evaluating the efficiency of a method which combine three proposed approaches for joint kinematics estimation: a versatile MBO framework (Duprey et al., 2010), the MIMU-tracking approach (Koning et al., 2015; Torres-Moreno et al., 2016) and the anatomical calibration procedure (Picerno et al., 2008).

2. Materials and methods

2.1. Measured data and procedure

The lower limb model consisted to a chain of rigid body segments representing the pelvis, the femur, the shank and the foot. Each segment coordinate system was constructed consistently with the anatomical calibration procedure, with one MIMU placed on each segment (Picerno et al., 2008). The experiment involved only one subject with no history of lower limb complaints and gave his informed consent for this experiment. The protocol proposed in Picerno et al. (2008) was reproduced for the calibration as well as for the assessment of movement parameters. A total of five MIMU sensors (MTx, Xsens, Enschede, Netherlands) were used for this experiment. The MTx is a small and light device (38 x 58.6 x 20.9mm, 30g) consisting of a 3D rate gyroscope, a 3D linear accelerometer and a 3D magnetometer. The pre-processed signals resulting from the filtering and smoothing of the raw angular velocity and linear acceleration were recorded while MIMU orientation, (i.e., technical coordinate system) with respect to the earth-based reference coordinate system was extracted from Xsens fusion algorithm. To minimize issues related to ferro-magnetic disturbances, experiments were conducted in a controlled magnetic field environment. The movement was simultaneously tracked by an optoelectronic system (9 VICON Mx cameras, Oxford Metrics, UK), marker trajectories were recorded with respect to its own calibrated reference coordinate system. Both MIMU output signals and stereophotogrammetric data were recorded at 100 samples per second. Four MIMUs were firmly attached to the subject's sacrum, the lateral-distal thigh, the medial facet of the tibia and, laterally, to the tarsal bones. Additionally, a marker cluster composed of three reflective markers were fixed to each MIMU.

An anatomical calibration was performed (Picerno et al., 2008) in order to define the segment coordinate systems. To summarize, a calibration device equipped with a MIMU and a marker cluster is used to measure two anatomical directions for each segment, by pointing anatomical landmarks (AL) in a static position. In this way a rotation matrix is established between the technical coordinate system attached to the MIMU for a given segment and the anatomical coordinate system defining the orientation of the segment. This matrix is referred to as calibration matrix $\mathbf{R}_{i^* \rightarrow i}$. The AL locations were identified through manual palpation and marked with a felt pen. After the calibration procedure accomplished, retro-reflective markers were placed on the ALs using the relevant marks. Thirteen retro-reflective markers were glued on the subject, with four markers on the pelvis (left and right anterior and posterior superior iliac spines), three markers on the thigh (great trochanter, lateral and medial epicondyles), three markers on the shank (head of the fibula, lateral and medial malleoli) and three markers on the foot (calcaneus, first and fifth metatarsal

heads). The orientation of the MIMU sensor and the position of the marker-cluster were tracked simultaneously in their respective reference coordinate system. Note that each reference coordinate system derived from MIMUs is expressed in a common earth-based coordinate system. Two skeletal models were built from the two different acquisition systems. The lengths of the segments were defined with the two anatomical landmarks pointed with the calibration device (Picerno et al., 2008). The segment coordinate systems were correspondingly defined using the stereophotogrammetric system. In other words, the same anatomical calibration (i.e., two anatomical directions for each segment) was performed using the marker-cluster on the calibration device. The kinematic model was constructed using the length of segments measured during the calibration phase between the palpated anatomical landmarks (or regression equations from such measurements). For instance, the segments were defined in terms of length by the distance from first metacarpal to calcaneus for the foot; from lateral malleolus to lateral epicondyle for the shank, from lateral epicondyle to great trochanter. The kinematic model was fixed at the reconstructed proximal endpoint of the pelvis segment as origin. Using direct kinematics method and the MIMU orientations, the kinematic chain therefore allowed to estimate the initial solution of the bone pose to be used in the MBO method. The same procedure was used to build segments from skin markers except that the orientation was obtained by straightforward measurement of the marker positions. For consistency, the same length was used for both models, furthermore, the initial solution of the movement was reconstructed considering spherical constraints at the hip, the knee and the ankle, using skin markers and MIMUs. The movement was thus reconstructed using both methods, the stereophotogrammetry-based reconstruction, referred to as method SSS_{vicon} was used as a reference for the study, and the MIMU-based direct kinematics computation, referred to as method SSS_{MIMU} , was considered as initial solution for MBO method.

It is important to note that both the acquisition systems have their own reference coordinate system. The MIMUs reference coordinate system is an earth-based coordinate system, common to all the MIMUs, while the stereophotogrammetric system has a calibrated reference coordinate system. A calibration was done during the anatomical calibration procedure performed using both MIMUs and the marker-cluster rigidly attached to the calibration device while pointing the same ALs to express both acquisition datasets in the same coordinate system. The rotation matrix which represents the orientation of the earth-based coordinate (MIMUs) system in the reference coordinate system (stereophotogrammetry) is referred to as $\mathbf{R}_{0 \rightarrow 0^*}$.

As already mentioned, the measured variables involved in the MBO method were the orientation of the technical coordinate system expressed in the earth-based coordinate system $\mathbf{R}_{0^* \rightarrow i^*}^{\wedge}$, the

angular velocity $\hat{\boldsymbol{\omega}}_i|_{i^*}$ and the linear acceleration $\hat{\mathbf{r}}_{A_i}|_{i^*}$ expressed in the technical coordinate system ($|_{i^*}$ denotes a vector expressed in the technical coordinate system of the device and $\hat{}$ denotes a variable measured by the MIMU as opposed to the modeled one). These quantities were thereafter transformed in the adequate coordinate system.

The measured orientation matrix $\hat{\mathbf{R}}_{0^* \rightarrow i^*}$ was first expressed in the anatomical (segment) coordinate system thanks to the calibration matrix $\mathbf{R}_{i^* \rightarrow i}$, then, expressed in the reference coordinate system (stereophotogrammetry) thanks to the rotation matrix $\mathbf{R}_{0 \rightarrow 0^*}$. The matrix $\hat{\mathbf{R}}_{0 \rightarrow i}$ stands for the measured orientation of the segment coordinate system in the reference coordinate system, defined as follow:

$$\hat{\mathbf{R}}_{0 \rightarrow i} = \mathbf{R}_{0 \rightarrow 0^*} \hat{\mathbf{R}}_{0^* \rightarrow i^*} \mathbf{R}_{i^* \rightarrow i} \quad (3.1)$$

The measured angular velocity $\hat{\boldsymbol{\omega}}_i|_{i^*}$ was expressed in the segment coordinate system thanks to the calibration matrix $\mathbf{R}_{i^* \rightarrow i}$, the computation of $\hat{\boldsymbol{\omega}}_i|_i$ ($|_i$ denotes a vector expressed in this segment coordinate system) is straightforward:

$$\hat{\boldsymbol{\omega}}_i|_i = (\mathbf{R}_{i^* \rightarrow i})^T \hat{\boldsymbol{\omega}}_i|_{i^*} \quad (3.2)$$

Nevertheless, the format of the measured data were different, for instance, the measured orientation were represented by a 3x3 matrix, the angular velocity and linear acceleration were represented by a 3x1 vector. The MBO framework imposed to format these data in consistent vectors. To this end, an application ν was defined which represents the reshaping of the vectors of a 3x3 matrix into a 9x1 vector. For instance, the orientation matrix $\hat{\mathbf{R}}_{0 \rightarrow i} = [\mathbf{X}_i|_0 \quad \mathbf{Y}_i|_0 \quad \mathbf{Z}_i|_0]$ can be reshaped in a 9x1 vector through the application ν :

$$\nu(\hat{\mathbf{R}}_{0 \rightarrow i}) = \begin{bmatrix} \mathbf{X}_i|_0 \\ \mathbf{Y}_i|_0 \\ \mathbf{Z}_i|_0 \end{bmatrix} \quad (3.3)$$

The angular velocity vector $\hat{\boldsymbol{\omega}}_i|_i = \begin{bmatrix} \hat{\omega}_{ix} \\ \hat{\omega}_{iy} \\ \hat{\omega}_{iz} \end{bmatrix}_i$, after being transformed to the skew matrix for

convenience in the MBO method $\hat{\tilde{\boldsymbol{\omega}}}_i|_i = \begin{bmatrix} 0 & -\hat{\omega}_{iz} & \hat{\omega}_{iy} \\ \hat{\omega}_{iz} & 0 & -\hat{\omega}_{ix} \\ -\hat{\omega}_{iy} & \hat{\omega}_{ix} & 0 \end{bmatrix}_i$, can be transformed in a 9x1

vector following using the application ν , finally:

$$v(\tilde{\boldsymbol{\omega}}_i|_i) = \begin{bmatrix} 0 & \hat{\omega}_{iz} & -\hat{\omega}_{iy} & -\hat{\omega}_{ix} & 0 & \hat{\omega}_{ix} & \hat{\omega}_{iy} & -\hat{\omega}_{iz} & 0 \end{bmatrix}_i^T \quad (3.4)$$

The linear acceleration $\mathbf{r}_{A_i}^\wedge|_{i^*}$ was also expressed in the segment coordinate system using the same transformation:

$$\ddot{\mathbf{r}}_{A_i}|_i = (\mathbf{R}_{i^* \rightarrow i})^T \ddot{\mathbf{r}}_{A_i}|_{i^*} \quad (3.5)$$

Note that, the measured acceleration also accounts for gravity, it must be considered in the modeled acceleration.

2.2. Multi-body optimization framework

2.2.1. Modeled orientation

The modeled orientation of the segment was defined by a rotation matrix representing the orientation of the anatomical coordinate system of the segment i in the global reference coordinate system. Two equivalent computation formalisms are therefore possible to express the rotation matrix $\mathbf{R}_{0 \rightarrow i}$, it is obtained from \mathbf{Q}_i thanks to the matrix $\mathbf{B}_i^{\mathbf{uv}}$ (Dumas and Chèze, 2007),

$$\mathbf{R}_{0 \rightarrow i} = \begin{bmatrix} \mathbf{u}_i & (\mathbf{r}_{P_i} - \mathbf{r}_{D_i}) & \mathbf{w}_i \end{bmatrix} [\mathbf{B}_i^{\mathbf{uv}}]^{-1} \quad (3.6)$$

Or thanks to the interpolation matrices $\mathbf{N}_i^{X_i}$, $\mathbf{N}_i^{Y_i}$ and $\mathbf{N}_i^{Z_i}$:

$$\mathbf{R}_{0 \rightarrow i} = \begin{bmatrix} \mathbf{N}_i^{X_i} & \mathbf{N}_i^{Y_i} & \mathbf{N}_i^{Z_i} \end{bmatrix} \mathbf{Q}_i \quad (3.7)$$

In both cases, the operator of the transformation is constant in time. Indeed, we can expressed the components of a vector \mathbf{n}_i embedded in the segment, and in particular, the vectors $\mathbf{X}_i|_0$, $\mathbf{Y}_i|_0$ and $\mathbf{Z}_i|_0$ as:

$$\mathbf{n}_i = \left(n_i^{n_i}\right)_u \mathbf{u}_i + \left(n_i^{n_i}\right)_v (\mathbf{r}_{P_i} - \mathbf{r}_{D_i}) + \left(n_i^{n_i}\right)_w \mathbf{w}_i \quad (3.8)$$

$$\mathbf{n}_i = \underbrace{\begin{bmatrix} \left(n_i^{n_i}\right)_u \mathbf{E}_{3 \times 3} & \left(n_i^{n_i}\right)_v \mathbf{E}_{3 \times 3} & -\left(n_i^{n_i}\right)_v \mathbf{E}_{3 \times 3} & \left(n_i^{n_i}\right)_w \mathbf{E}_{3 \times 3} \end{bmatrix}}_{\mathbf{N}_i^{n_i}} \begin{bmatrix} \mathbf{u}_i \\ \mathbf{r}_{P_i} \\ \mathbf{r}_{D_i} \\ \mathbf{w}_i \end{bmatrix} \quad (3.9)$$

2.2.2. Modeled angular velocity

As explained above, the measured angular velocity $\hat{\boldsymbol{\omega}}_i|_i$ was transformed in a skew matrix. In the same formulation, the modeled angular velocity $\boldsymbol{\omega}_i|_i$ was extracted from the computation of the skew matrix $\tilde{\boldsymbol{\omega}}_i|_i$:

$$\tilde{\boldsymbol{\omega}}_i|_i = \begin{bmatrix} 0 & -\omega_{iz} & \omega_{iy} \\ \omega_{iz} & 0 & -\omega_{ix} \\ -\omega_{iy} & \omega_{ix} & 0 \end{bmatrix}_i \quad (3.10)$$

It was computed from the rotation matrix of segment i $(\mathbf{R}_{0 \rightarrow i})^T$ and its first time derivative $(\dot{\mathbf{R}}_{0 \rightarrow i})$ (Legnani et al., 1996):

$$\tilde{\boldsymbol{\omega}}_i|_i = (\mathbf{R}_{0 \rightarrow i})^T \dot{\mathbf{R}}_{i \rightarrow 0} \quad \text{with} \quad (\mathbf{R}_{0 \rightarrow i})^T = (\mathbf{R}_{0 \rightarrow i})^{-1} \quad (3.11)$$

The expression of $\dot{\mathbf{R}}_{i \rightarrow 0}$ was straightforward considering equation (3.7):

$$\dot{\mathbf{R}}_{i \rightarrow 0} = \begin{bmatrix} \mathbf{N}_i^{X_i} & \mathbf{N}_i^{Y_i} & \mathbf{N}_i^{Z_i} \end{bmatrix} \dot{\mathbf{Q}}_i \quad (3.12)$$

since the interpolation matrix $\begin{bmatrix} \mathbf{N}_i^{X_i} & \mathbf{N}_i^{Y_i} & \mathbf{N}_i^{Z_i} \end{bmatrix}$ is constant.

Note that the nine components of the orientation vector and angular velocity vector were not independent, but the redundancy of the information reinforce the robustness of the method. For instance, it is convenient to compare to zero the diagonal values of the skew matrix of the modeled angular velocity.

2.2.3. Modeled acceleration

The position in the ICS of a point A_i embedded in segment i is computed from parameters \mathbf{Q}_i by a linear interpolation:

$$\mathbf{r}_{A_i}|_0 - \mathbf{r}_{P_i} = \left(n_i^{A_i}\right)_u \mathbf{u}_i + \left(n_i^{A_i}\right)_v (\mathbf{r}_{P_i} - \mathbf{r}_{D_i}) + \left(n_i^{A_i}\right)_w \mathbf{w}_i \quad (3.13)$$

$$\mathbf{r}_{A_i}|_0 = \underbrace{\begin{bmatrix} \left(n_i^{A_i}\right)_u \mathbf{E}_{3 \times 3} & \left(1 + \left(n_i^{A_i}\right)_v\right) \mathbf{E}_{3 \times 3} & -\left(n_i^{A_i}\right)_v \mathbf{E}_{3 \times 3} & \left(n_i^{A_i}\right)_w \mathbf{E}_{3 \times 3} \end{bmatrix}}_{\mathbf{N}_i^{A_i}} \begin{bmatrix} \mathbf{u}_i \\ \mathbf{r}_{P_i} \\ \mathbf{r}_{D_i} \\ \mathbf{w}_i \end{bmatrix} \quad (3.14)$$

with $\mathbf{E}_{3 \times 3}$ the identity matrix, $\left((n_i^{A_i})_{\mathbf{u}}, (n_i^{A_i})_{\mathbf{v}}, (n_i^{A_i})_{\mathbf{w}} \right)$ the coordinates of point A_i expressed in the non-orthogonal coordinate system (NSCS) of segment i $(P_i, \mathbf{u}_i, \mathbf{r}_{P_i} - \mathbf{r}_{D_i}, \mathbf{w}_i)$ and $\mathbf{N}_i^{A_i}$ the corresponding interpolation matrix.

The constant interpolation matrix $\mathbf{N}_i^{A_i}$ can then be used to build the model of linear acceleration of point A_i :

$$\ddot{\mathbf{r}}_{A_i} \Big|_0 = \mathbf{N}_i^{A_i} \ddot{\mathbf{Q}}_i \quad (3.15)$$

The origin of the accelerometer, which is the point where the linear acceleration is calculated, is estimated thanks to the marker-cluster fixed on the MIMU and stereophotogrammetry.

To be consistent with the measured linear acceleration, further transformations were operated. First the gravity must be taken into account, since $\ddot{\mathbf{r}}_{A_i}$ represents the linear acceleration of a point A_i embedded to the segment coordinate system in the reference coordinate system. The vertical axis was assumed to be coincident with the gravity vector \mathbf{g} . Then the obtained modeled linear acceleration was expressed in the segment coordinate system, the modeled linear acceleration became:

$$\ddot{\mathbf{r}}_{A_i} \Big|_i = (\mathbf{R}_{0 \rightarrow i})^T \left(\ddot{\mathbf{r}}_{A_i} \Big|_0 + \mathbf{g} \right) \quad (3.16)$$

Note that the linear acceleration depends on the point in which it is computed, in particular, the measured linear acceleration is given at the origin of the accelerometer. As already mentioned, the MIMUs does not allow the measurement of positions, as a consequence, the corresponding modeled acceleration is calculated at the estimated, unknown *a priori*, origin of the accelerometer and so estimated with a possible high level of error. This quantity is therefore to consider with care and tracking accelerations only is unreliable and may result in inaccurate estimation of the kinematics. As explained before, the kinematic model was assumed to be fixed at the proximal endpoint of the pelvis segment. Therefore, the modeled acceleration can only partially represents the measured one. According to the rules of composition of relative and absolute accelerations, the modeled acceleration (expressed in a coordinate system parallel to the ICS but translated at the pelvis proximal endpoint) and the measured acceleration (expressed in the ICS) can only match if the pelvis proximal endpoint translates at constant velocity during the movement. It is the hypothesis made in the study.

2.2.1. Objective function

The originality of this study lied in the nature of input data introduced in the MBO method. While classic MBO considers the position of markers to estimate bone pose, we proposed to substitute marker trajectories with MIMU-derived variables, namely angular velocity, linear acceleration and orientation of the MIMU. For any segment i , the modeled position depended on the natural coordinates \mathbf{Q}_i . Both linear and angular velocities and accelerations involve their first and second

time derivatives $\dot{\mathbf{Q}}_i = \frac{d\mathbf{Q}_i}{dt}$ and $\ddot{\mathbf{Q}}_i = \frac{d^2\mathbf{Q}_i}{dt^2}$.

The modeled angular velocity $\boldsymbol{\omega}_i|_i(\mathbf{Q}_i, \dot{\mathbf{Q}}_i)$, linear acceleration $\ddot{\mathbf{r}}_{A_i}|_i(\mathbf{Q}_i, \ddot{\mathbf{Q}}_i)$ and orientation $\mathbf{R}_{0 \rightarrow i}(\mathbf{Q}_i)$ were therefore computed from the design variables set as $\mathbf{Q}_i, \dot{\mathbf{Q}}_i, \ddot{\mathbf{Q}}_i$.

The MBO method was formulated as follow:

$$\begin{aligned} \min_{\substack{\mathbf{Q} \\ \dot{\mathbf{Q}} \\ \ddot{\mathbf{Q}}}} f &= \frac{1}{2} [\boldsymbol{\Phi}^m]^T \mathbf{W} \boldsymbol{\Phi}^m + \frac{1}{2} \left(\begin{bmatrix} \dot{\boldsymbol{\Phi}}^k \\ \dot{\boldsymbol{\Phi}}^r \end{bmatrix}^T \dot{\mathbf{W}} \begin{bmatrix} \dot{\boldsymbol{\Phi}}^k \\ \dot{\boldsymbol{\Phi}}^r \end{bmatrix} + \begin{bmatrix} \ddot{\boldsymbol{\Phi}}^k \\ \ddot{\boldsymbol{\Phi}}^r \end{bmatrix}^T \ddot{\mathbf{W}} \begin{bmatrix} \ddot{\boldsymbol{\Phi}}^k \\ \ddot{\boldsymbol{\Phi}}^r \end{bmatrix} \right) \\ \text{subject to } &\begin{bmatrix} \boldsymbol{\Phi}^k \\ \boldsymbol{\Phi}^r \end{bmatrix} = \mathbf{0} \end{aligned} \quad (3.17)$$

where $\boldsymbol{\Phi}^k$ and $\boldsymbol{\Phi}^r$ stand for the kinematic and rigid body constraints and $\dot{\boldsymbol{\Phi}}^k, \dot{\boldsymbol{\Phi}}^r$ and $\ddot{\boldsymbol{\Phi}}^k, \ddot{\boldsymbol{\Phi}}^r$ stand for their first and second time derivatives respectively. The framework of the MBO considers the minimization of the difference between the measured and the modeled orientation, angular velocity and linear acceleration, respectively.

The problem was adapted to consider the first and second time derivatives of the kinematics and rigid body constraints as “soft” constraints. Indeed, it is convenient to manage the level of contribution of the constraints by choosing the matrices of weighting factor $\dot{\mathbf{W}}$ and $\ddot{\mathbf{W}}$ (the notation here is for weighting factors corresponding to the first and second time derivatives of the kinematic and rigid body constraints not the derivatives of weighting factors \mathbf{W}). The objective function is however subject to the constraints $\boldsymbol{\Phi}^k$ and $\boldsymbol{\Phi}^r$.

The vector of driving constraints $\boldsymbol{\Phi}^m$ was therefore defined as follow:

$$\mathbf{\Phi}^m = \begin{bmatrix} v(\mathbf{R}_{0 \rightarrow 1}^{\wedge} - \mathbf{R}_{0 \rightarrow 1}(\mathbf{Q}_1)) \\ \vdots \\ v(\mathbf{R}_{0 \rightarrow 4}^{\wedge} - \mathbf{R}_{0 \rightarrow 4}(\mathbf{Q}_4)) \\ v(\tilde{\mathbf{\omega}}_1^{\wedge}|_1 - \tilde{\mathbf{\omega}}_1|_1(\mathbf{Q}_1, \dot{\mathbf{Q}}_1)) \\ \vdots \\ v(\tilde{\mathbf{\omega}}_4^{\wedge}|_4 - \tilde{\mathbf{\omega}}_4|_4(\mathbf{Q}_4, \dot{\mathbf{Q}}_4)) \\ \tilde{\mathbf{r}}_{A_1}^{\wedge}|_1 - \tilde{\mathbf{r}}_{A_1}|_1(\mathbf{Q}_1, \ddot{\mathbf{Q}}_1) \\ \vdots \\ \tilde{\mathbf{r}}_{A_4}^{\wedge}|_4 - \tilde{\mathbf{r}}_{A_4}|_4(\mathbf{Q}_4, \ddot{\mathbf{Q}}_4) \end{bmatrix} \quad (3.18)$$

The objective function can be detailed as:

$$\begin{aligned} f(\mathbf{Q}, \dot{\mathbf{Q}}, \ddot{\mathbf{Q}}) = & \frac{1}{2} \sum_{i=1}^4 \alpha_i v(\mathbf{R}_{0 \rightarrow i}^{\wedge} - \mathbf{R}_{0 \rightarrow i}(\mathbf{Q}_i))^2 \\ & + \frac{1}{2} \sum_{i=1}^4 \beta_i v(\tilde{\mathbf{\omega}}_i^{\wedge}|_i - \tilde{\mathbf{\omega}}_i|_i(\mathbf{Q}_i, \dot{\mathbf{Q}}_i))^2 \\ & + \frac{1}{2} \sum_{i=1}^4 \gamma_i (\tilde{\mathbf{r}}_{A_i}^{\wedge}|_i - \tilde{\mathbf{r}}_{A_i}|_i(\mathbf{Q}_i, \ddot{\mathbf{Q}}_i))^2 \\ & + \frac{1}{2} \delta \left(\begin{bmatrix} \dot{\mathbf{\Phi}}^k \\ \dot{\mathbf{\Phi}}^r \end{bmatrix}^T p_1 \begin{bmatrix} \dot{\mathbf{\Phi}}^k \\ \dot{\mathbf{\Phi}}^r \end{bmatrix} + \begin{bmatrix} \ddot{\mathbf{\Phi}}^k \end{bmatrix}^T p_2 \ddot{\mathbf{\Phi}}^k \right) \end{aligned} \quad (3.19)$$

Thus, the terms of the driving constraints which involves orientation matrix and angular velocity skew matrix were reshaped to a 9 by 1 vector through the application v for each instant of time, the construction of all the modeled variables will be detailed in the next sections. The matrix \mathbf{W} contains in the diagonal the factors α_i , β_i and γ_i associated to the terms of orientation, angular velocity and linear acceleration respectively. Note that the kinematic constraints and rigid body constraints are introduced using a penalty-based method involving a weighting factor δ affecting all these constraints and individual weighting factors p_1 and p_2 . The second time-derivative of the rigid body constraints were not considered since it highly deteriorates the convergence of the method. In other words, the weighting factor for $\ddot{\mathbf{\Phi}}^r$ is always set to 0.

The objective function can be written as:

$$f = f_R + f_\omega + f_A + f_\Phi \quad (3.20)$$

with

$$f_R = \frac{1}{2} \sum_{i=1}^4 \alpha_i v \left(\hat{\mathbf{R}}_{0 \rightarrow i} - \mathbf{R}_{0 \rightarrow i}(\mathbf{Q}_i) \right)^2 \quad (3.21)$$

$$f_\omega = \frac{1}{2} \sum_{i=1}^4 \beta_i v \left(\hat{\tilde{\omega}}_i|_i - \tilde{\omega}_i|_i(\mathbf{Q}_i, \dot{\mathbf{Q}}_i) \right)^2 \quad (3.22)$$

$$f_A = \frac{1}{2} \sum_{i=1}^4 \gamma_i \left(\hat{\ddot{\mathbf{r}}}_{A_i}|_i - \ddot{\mathbf{r}}_{A_i}|_i(\mathbf{Q}_i, \ddot{\mathbf{Q}}_i) \right)^2 \quad (3.23)$$

$$f_\Phi = \frac{1}{2} \delta \left(\begin{bmatrix} \dot{\Phi}^k \\ \dot{\Phi}^r \end{bmatrix}^T p_1 \begin{bmatrix} \dot{\Phi}^k \\ \dot{\Phi}^r \end{bmatrix} + \begin{bmatrix} \ddot{\Phi}^k \end{bmatrix}^T p_2 \ddot{\Phi}^k \right) \quad (3.24)$$

In general, for the constraint Φ , the Jacobian matrix of Φ with respect to \mathbf{Q} , and its first time derivative, we have:

$$\begin{cases} \Phi(\mathbf{Q}) = 0 \\ \dot{\Phi}(\mathbf{Q}, \dot{\mathbf{Q}}) = \frac{\partial \Phi(\mathbf{Q})}{\partial \mathbf{Q}} \dot{\mathbf{Q}} = 0 \\ \ddot{\Phi}(\mathbf{Q}, \dot{\mathbf{Q}}, \ddot{\mathbf{Q}}) = \frac{d}{dt} \left(\frac{\partial \Phi(\mathbf{Q})}{\partial \mathbf{Q}} \right) \dot{\mathbf{Q}} + \frac{\partial \Phi(\mathbf{Q})}{\partial \mathbf{Q}} \ddot{\mathbf{Q}} = 0 \end{cases} \quad (3.25)$$

The method allowed to alter the values for the weighting factors α_i , β_i and γ_i to consider any combination of orientation, velocity or acceleration terms. In particular, by setting zero for β_i and γ_i , the principle was the same as proposed in (Koning et al., 2015).

As explained before, the kinematic model was assumed to be fixed at the proximal endpoint of the pelvis segment. Indeed, both origins of the earth-based coordinate system of the MIMUs and of the ICS of the stereophotogrammetry were translated to the corresponding proximal endpoint of the pelvis defined in static position.

2.3. Experimental methods

In this study, the joint angles for the ankle, the knee and the hip were estimated through the MBO method embedding spherical joint models at each joint (referred to as SSS), and compared to the reconstructed joint angles from skin markers (method referred to as $\text{SSS}_{\text{vicon}}$ (Table 3.1)) and MIMUs (method referred to as SSS_{MIMU}). The bias extracted from Bland-Altman analysis (Bland

and Altman, 1986) were reported to investigate the between-method difference of the MBO methods with respect to the reference. Additionally to the joint angles comparison, the method was evaluated by comparing the position of the distal point of the foot estimation through the MBO method against the foot position obtained from stereophotogrammetry. In both cases, the foot position was expressed in the ICS translated at the pelvis proximal endpoint. The study considered different combinations of input data. The different objective functions f that can be included into the MBO method are reported as follow:

Name of the method	Kinematic model	Objective function
SSS_R	SSS	$f = f_R + f_{\Phi}$
SSS_{ω}	SSS	$f = f_{\omega} + f_{\Phi}$
SSS_A	SSS	$f = f_A + f_{\Phi}$
$SSS_{\omega+A}$	SSS	$f = f_{\omega} + f_A + f_{\Phi}$
$SSS_{R+\omega}$	SSS	$f = f_R + f_{\omega} + f_{\Phi}$
SSS_{R+A}	SSS	$f = f_R + f_A + f_{\Phi}$
$SSS_{R+\omega+A}$	SSS	$f = f_R + f_{\omega} + f_A + f_{\Phi}$

Table 3.1 Methods notation

The MBO method was evaluated regarding the performance of kinematics estimation and foot position with all the above-mentioned models. Nevertheless, the estimated kinematics obtained with MBO embedding two models only were reported because, on one hand, the estimated kinematics obtained with $SSS_{R+\omega}$, SSS_{R+A} , and $SSS_{R+\omega+A}$ was similar to the one obtained with SSS_R , and because, on the other hand, SSS_A did not converge. Thus, the comparative analysis of the joint kinematics estimates considered the methods SSS_R and SSS_{ω} only. Conversely, the results of the MBO processing embedding all the models were reported in the analysis of the residual of the objective function. The terms $d\bar{f}_R$, $d\bar{f}_{\omega}$ and $d\bar{f}_A$ refer to the residual of the objective function when embedded in the objective function and mean difference (mean difference between modeled and measured parameters) when only computed but not optimized. The residuals of the objective functions were confronted to the mean differences between modeled and measured angular velocities, accelerations and orientations while not embedded in the objective functions. The MBO was implemented in Matlab using the built-in function *fmincon* embedding the *sqp* algorithm with default parameters.

2.4. Statistics

The hypotheses of the study were supported by Bland-Altman analysis (Bland and Altman, 1986; McLaughlin, 2013) of the knee joint kinematics estimated from MBO embedding both methods SSS_R , SSS_ω . The between-method differences were computed for the MBO method embedding each model as well as the reference kinematics, determined from stereophotogrammetry and skin markers. The difference between MIMU-tracked kinematics and skin marker-based kinematics was plotted against the mean difference over reference and each MIMU-tracked kinematics (as initially proposed for Bland-Altman analysis) (Bland and Altman, 1986). Consequently, to assess differences in the performance of the methods, the Bland-Altman results for each model were compared. The method's accuracy was given by the bias, and its precision was given by the standard deviation of differences. Limits of agreement were set to 1.96 sd (lb: lower limit of agreement, ub: upper limit of agreement), providing an interval within which 95% of differences between MIMU-tracked and skin marker-based kinematics are expected to lie. Rmse and correlation coefficients (r^2) were also reported.

The position of the distal endpoint of the foot segment expressed in the ICS translated at the pelvis proximal endpoint obtained through the MBO method embedding each model was represented during the movement and compared to the position reconstructed using skin marker trajectories (i.e., middle of first and fifth metatarsal heads).

3. Results

3.1. Comparative study of the joint kinematics estimates

A qualitative analysis of the patterns of the joint angles reconstructed using skin-markers and the MIMUs showed similar results for EF at the knee and the hip, the pattern was slightly shifted for EF and IER at the ankle and for AA at the hip. Patterns were found similar with larger amplitudes for AA at the ankle, and IER at the knee for the MIMU-tracked kinematics. Finally, the patterns of AA at the knee and IER at the hip were found significantly different. The curves obtained using method SSS_R were superimposed with the joint angles directly obtained with the MIMUs and the anatomical calibration (method SSS_{MIMU}), for all angles at each joint (Figure 3.1). The results at knee and hip joint for EF with method SSS_ω were similar with the method SSS_{MIMU} , while a slight difference was observed for the other angles and joints.

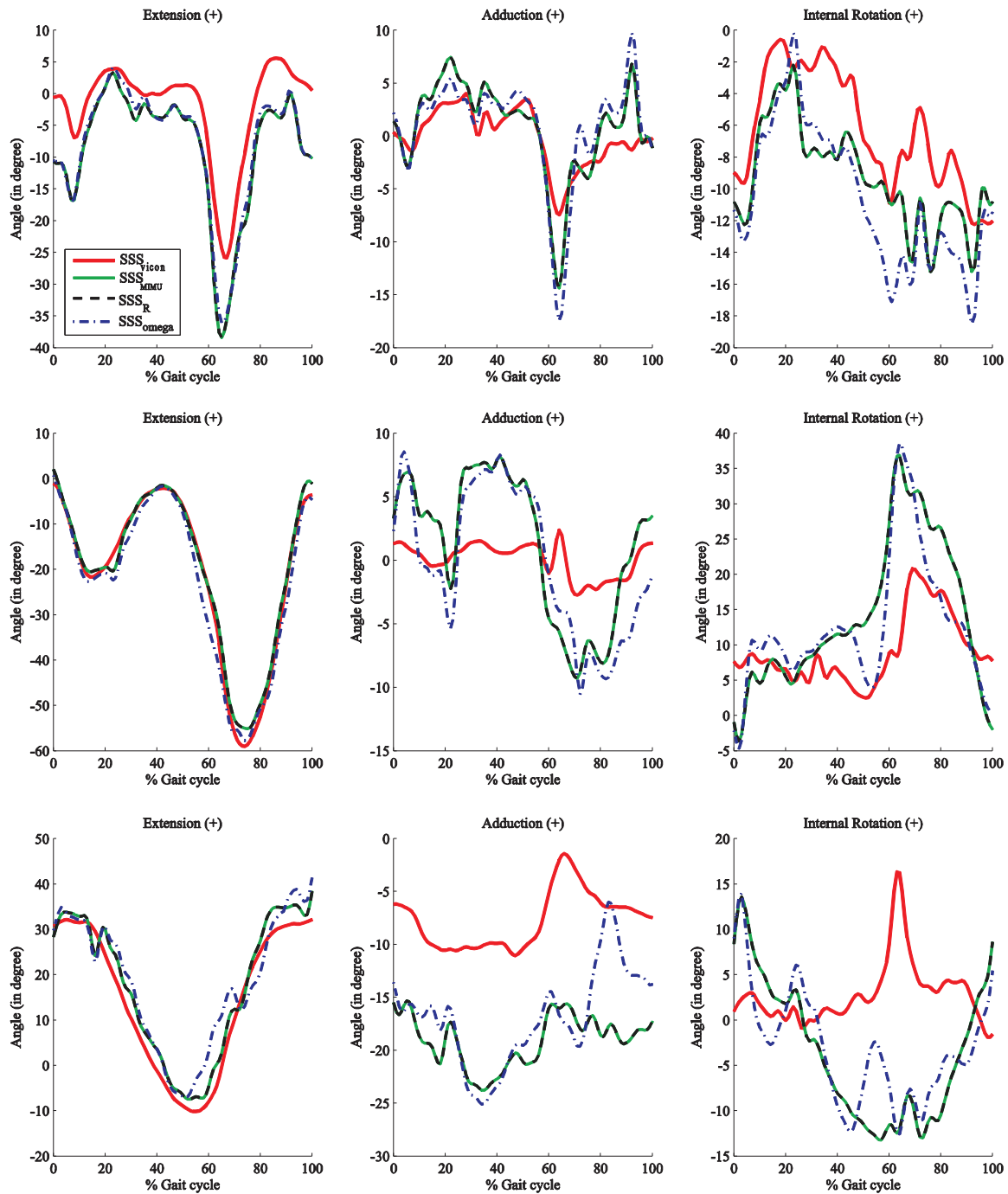


Figure 3.1 Lower limb joint angles during walking cycle.

Ankle (top), knee (middle) and hip (bottom) joint angles estimated through MBO method embedding spherical joint constraints (SSS) with orientation tracking (SSS_R : green), and angular velocity tracking (SSS_ω : blue) compared against reconstructed kinematics obtained from MIMUs (SSS_{MIMU} : black) and skin markers (SSS_{vicon} : red).

3.1.1. Bias

The kinematics directly obtained with the MIMUs and the anatomical calibration (method SSS_{MIMU}) and the MIMU-tracked kinematics obtained with method SSS_R showed the same absolute value of the bias (Figure 3.2)

for EF and AA when compared to the skin markers-based kinematics, with 0.9° and 1.1° , respectively. The bias was found larger with method SSS_ω for EF (2.0°), smaller for AA (0.3°). For IER, the largest absolute bias was found with model SSS_ω (9.3°) and the smallest with method SSS_R (3.4°), while the absolute value of the bias obtained from the MIMUs orientation was in-between (5.0°). The bias was systematically negative with kinematics derived from MIMUs and method SSS_R , while it was positive with method SSS_ω .

3.1.2. Standard deviation

The standard deviation was found similar with the MIMU-tracked kinematics and the estimation using method SSS_R for EF and AA, with 1.6° and 4.7° , respectively while, with method SSS_ω , sd was found significantly higher for EF (2.5°) and slightly higher for AA (4.9°). For IER, the kinematics obtained with method SSS_R showed the smallest sd (7.4°) with respect to the skin marker-based kinematics, when for the kinematics obtained from the MIMUs orientations and the kinematics obtained using method SSS_ω the sd were found larger, with 8.2° and 10.1° , respectively.

3.1.3. Root mean square differences

For EF and IER rmsd values were found similar with the MIMU orientations and the ones obtained with method SSS_R with 1.9° and 4.8 , respectively. The rmsds found for EF and AA with method SSS_ω were 3.2° and 4.9° . The rmsds for IER obtained from the MIMU orientations, methods SSS_R and SSS_ω were respectively 9.5° , 8.1° and 13.6° .

3.1.4. Correlation coefficient

The value of r^2 for the three methods was similar and between 0.98 and 0.99. For AA, method SSS_ω showed the larger value for r^2 with 0.61 than the other methods (0.56). For IER, the largest value for r^2 was found with method SSS_ω (0.59), and the smallest with method SSS_R (0.38), while with the MIMU orientations the value for r^2 was 0.44.

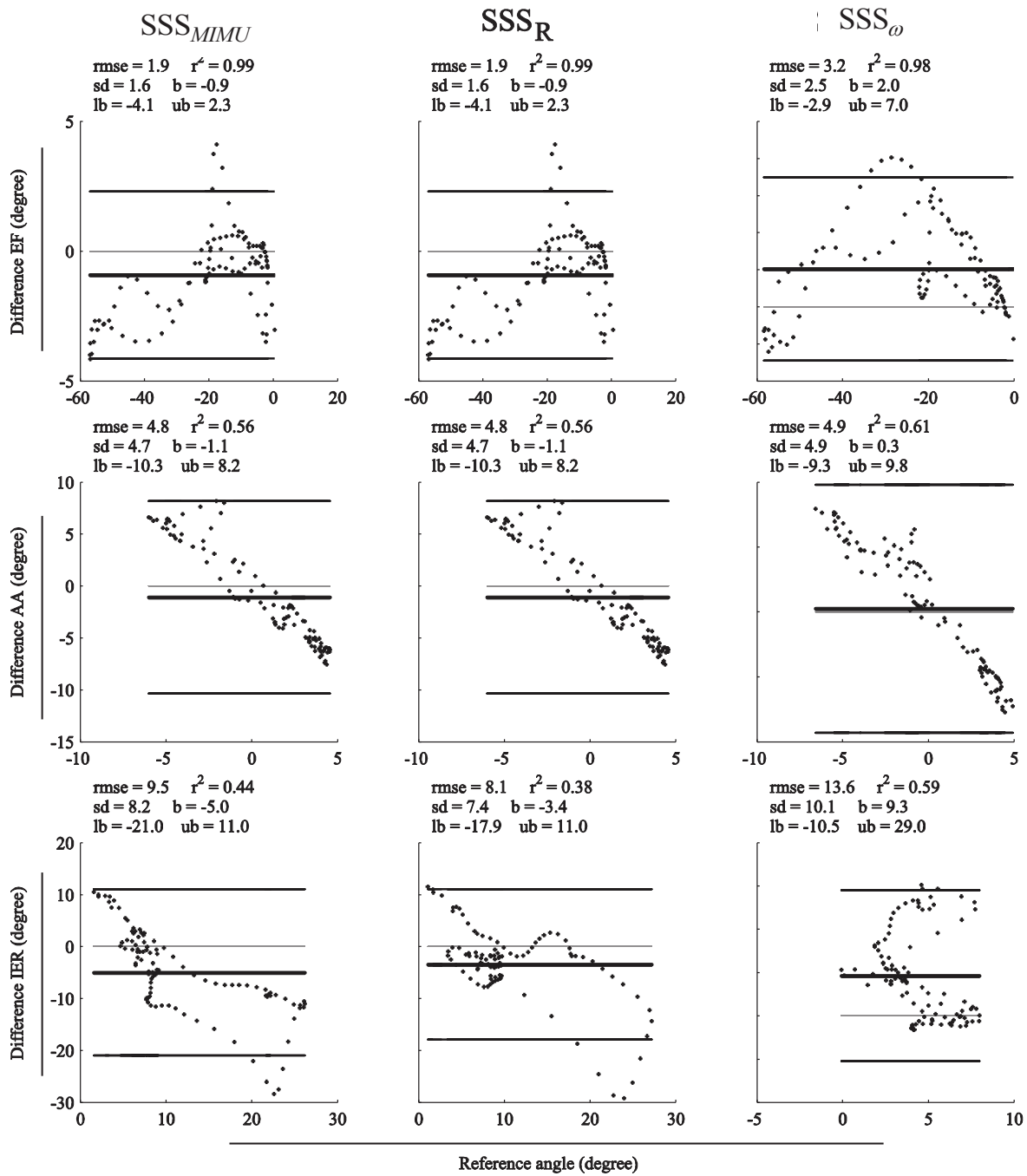


Figure 3.2 Bland Altman plot.

Bland-Altman plot with reference kinematics (absissas) and difference (ordinates) between model-derived and reference skin marker based kinematics (method SSS_{vicon}). From left to right Bland-Altman plots for methods SSS_{MIMU}, SSS_R, SSS_ω respectively, corresponding to joint angles, from top to bottom EF, AA, IER. Differences between model-derived kinematics and skin marker-based kinematics are plotted against reference amplitude of movement (angle). Thick black line represents the bias (mean of the differences) whose value is designated by b , thin black lines represent the limits of agreement (lb and ub) whose value is designated by $l = b \pm 1.96$ standard deviation. Squared Pearson's correlation coefficient (r^2), root mean square error (rmse) and standard deviation (sd) are displayed for each graph.

3.2. Objective function residual and mean differences between measured and modeled parameters

The analysis of the mean residual resulting from the computation of the methods SSS_R , SSS_ω , SSS_A , $SSS_{R+\omega}$, SSS_{R+A} and $SSS_{R+\omega+A}$ showed that the ability of the MBO to estimate the orientation, the angular velocity or the acceleration depends on the presence of the corresponding variable in the objective function. The mean residuals of f were reported in Table 3.2 for all models.

	SSS_R	SSS_ω	SSS_A	$SSS_{R+\omega}$	SSS_{R+A}	$SSS_{R+\omega+A}$
\bar{df}_R	1.5e-13	1.5e-2	-	2.0e-13	2.9e-14	6.1e-12
\bar{df}_ω	20.5	2.0e-13	-	8.0e-14	21.7	2.2e-14
\bar{df}_A	1.9e2	2.0e2	-	1.9e2	4.0e-10	1.3e-13

Table 3.2 Residual and mean difference.

Mean residual of the objective function and mean difference between measured and modeled parameters corresponding to the three terms \bar{df}_R , \bar{df}_ω and \bar{df}_A resulting from the comparison of the joint angles estimates obtained with methods SSS_R , SSS_ω , SSS_A , $SSS_{R+\omega}$, SSS_{R+A} and $SSS_{R+\omega+A}$.

3.3. Foot position and error

The analysis of the position of the foot expressed in the ICS translated at the pelvis proximal endpoint revealed the same pattern for the movement computed by forward kinematics using the MIMUs orientations when compared to the estimate obtained from method SSS_ω (Figure 3.3). About X axes, the patterns were similar with all methods, about Y axes, the foot position obtained with method SSS_ω was slightly different, about Z axes, the estimates were similar with method SSS_R when compared to the reference.

Concerning the difference in position regarding the reference position, the method SSS_ω globally provided similar patterns, with picks of larger amplitude than provided by method SSS_R . The pick-to-pick amplitude were found similar with both methods, 86 mm along X axes, larger with method SSS_ω than with method SSS_R (76 mm and 55 mm) along Y axes, respectively and larger with method SSS_ω than with method SSS_R (88 mm and 94 mm) along Z axes.

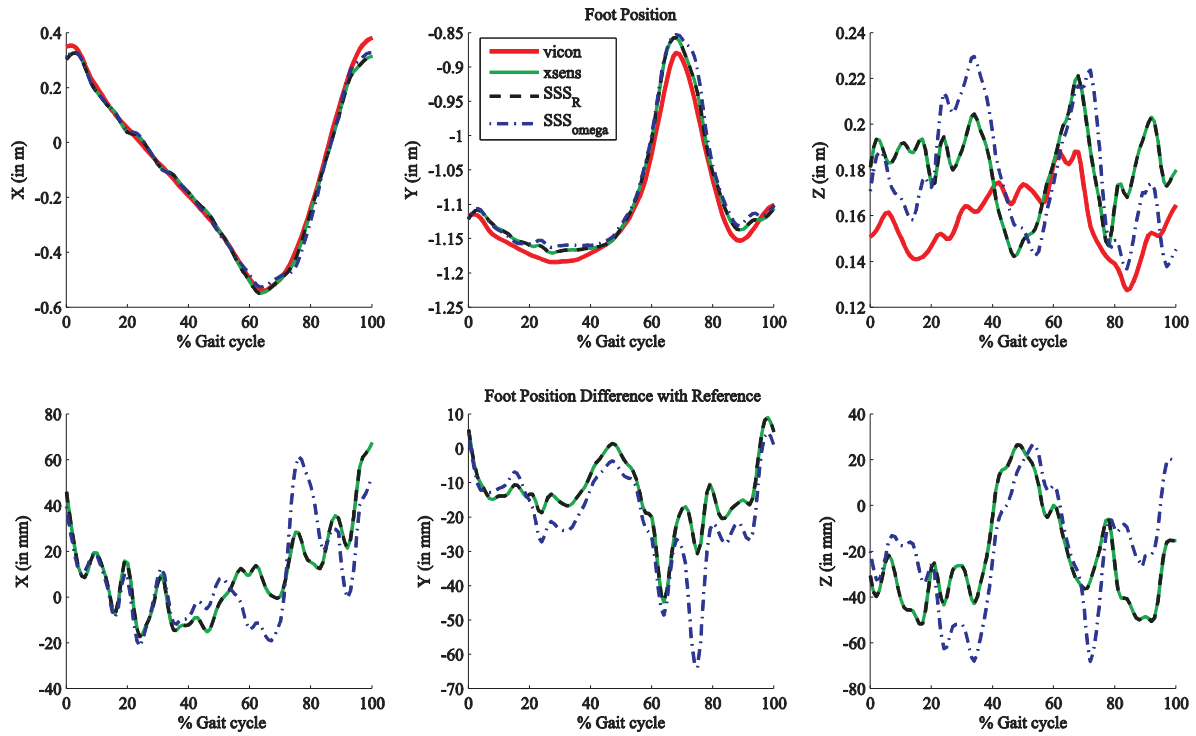


Figure 3.3 Foot position and error with respect to the reference.

On top, foot position along ICS axes (origin translated to the proximal point of the pelvis segment) estimated through MBO method embedding spherical joint constraints (SSS) with orientation tracking (SSS_R : green), and angular velocity tracking (SSS_ω : blue) compared against reconstructed foot position from MIMUs (black) and skin markers (red) and difference in position against reference. On bottom, the difference against the foot position reconstructed from skin markers of the foot position estimated through MBO with orientation tracking (SSS_R : green), angular velocity tracking (SSS_ω : blue) and the kinematics reconstructed from MIMUs (black).

4. Discussion

As expected, the orientations obtained by the MIMUs and the fusion algorithm provided by the manufacturer can be implemented in the MBO with satisfactory performance with respect to the stereophotogrammetry for kinematics estimation, as well as for proximal point of the foot position estimation. The importance of the calibration has been confirmed to be critical since it represents the main reason for the difference between skin marker-based and MIMU-tracked kinematics. The objective function residuals revealed that the method is reliable in minimizing the errors in the modeled orientations, the angular velocities and the accelerations. Globally the joint angles corresponded well to the angles obtained from stereophotogrammetry.

The MBO method showed satisfying performance in estimating joint angles and foot position with methods SSS_ω (and $SSS_{\omega+A}$ which was not reported). In other words, the kinematic model can

be driven by angular velocity data without involving the magnetometer data, integration of signals nor fusion algorithm, pending an appropriate initial guess. The influence of this initial guess has not been investigated here. Nevertheless, the possibility, in the proposed MBO method, of using principally or exclusively the angular velocity data may reveal of great interest if the MIMUs are to be used in a perturbed magnetic field environment.

The kinematics estimates obtained from the MBO methods embedding models involving the acceleration were tested but not reported since they did not converge. Indeed, due to the errors in the estimation of the position of the origin of the accelerometer and/or due to the hypothesis made for the translation of the pelvis proximal endpoint at constant velocity, the results were far from the reference when tracking the acceleration only.

The kinematics estimation is similar to the kinematics obtained directly using MIMUs orientation (through anatomical calibration), so long as the orientation criterion is introduced into the objective function. In other terms, the MBO method showed similar performance in estimating joint angles with methods $SSS_{R+\omega}$, SSS_{R+A} and $SSS_{R+\omega+A}$ for equal weighting factors on each component of the objective function.

The present study succeeded in merging three existing approaches in showing that the MBO embedding MIMU-derived objective function (Koning et al., 2015) with the anatomical calibration procedure (Picerno et al., 2008), results in physiological knee joint angle estimates. The MIMU-tracking procedure considering orientations and angular velocity totally comply with the MBO framework. The hypothesis that anatomical calibration is adequate to define segment coordinate system also holds true. To demonstrate that, the calibration of the segment coordinate system performed with the stereophotogrammetric data followed the methodology of (Picerno et al., 2008) in order to use the same definition for the processing of both MIMUs and skin markers. Further validation would be required to evaluate the accuracy of the method. The study demonstrated that the MBO method embedding a MIMU-based objective function, and in particular when considering angular velocities without integration, is competitive with regard to a skin marker-based objective function.

The study deserves further development in regard to the acceleration. Furthermore the estimated kinematics obtained with MBO embedding MIMU signals in the objective function depends on the initial solution of the biomechanical model, determined at this time thanks to the orientation of MIMUs.

The proposed MIMU-driven framework is particularly promising with regard to musculoskeletal modeling, for inverse dynamics in particular. Indeed, the latter method traditionally considers dynamic quantities computed from an estimate of kinematics and derivatives. With the proposed

MIMU-tracking MBO, both velocity and acceleration parameters are estimated concurrently with bone pose, ensuring the consistency of the dataset. Nevertheless, as far as the position of the foot is not determined with respect to the ICS (only ICS translated at the pelvis proximal endpoint), the inverse dynamics shall not include force plate but shoe sensors (Faber et al., 2016; Khurelbaatar et al., 2015). This remains consistent with an ambulatory assessment and the proposed MBO ensures that every segments are well positioned with respect to the other and comply with the measured angular velocity and linear acceleration. These are exactly the quantities involved in the inverse dynamics.

More generally, the interest of the MBO method is the possibility to define various joint models, implement joint limits, and eventually limit the number of sensors. These are interesting perspectives for the use of MIMUs for the analysis of the musculoskeletal system, not investigated so far.

Chapter 4.

The content of this chapter is referred to the article:

“Knee Kinematics Estimation Using Multi-body Optimization Embedding a Knee Joint Stiffness Matrix: A Feasibility Study “

Submitted for publication in PLOS ONE (under review).

1. Introduction

The *in-vivo* assessment of lower limb joint kinematics is generally performed using an optoelectronic system and skin markers. Data processing often includes a multi-body optimization (MBO) procedure (Andersen et al., 2009; Duprey et al., 2010; Li et al., 2012; Lu and O'Connor, 1999; Moniz-Pereira et al., 2014; Reinbolt et al., 2005; Sandholm et al., 2011; Scheys et al., 2011; Sholukha et al., 2006b; Stagni et al., 2009). The principle is to minimize the sum of the squared distances between the measured and model-derived skin marker trajectories. The model-derived trajectories rely on a set of joint constraints modeling the osteoarticular structures (i.e., cartilage surfaces, capsule and ligaments). It is assumed that these joint constraints can help compensate for the soft tissue artefact (i.e., relative movement between the skin-markers and the underlying bone: STA).

STA represents the principal stumbling block in bone pose estimation (Leardini et al., 2005), and its quantification and compensation demand constant effort. As a consequence of the STA, it is commonly admitted that movement analysis using optoelectronic systems and skin markers, and state-of-the art data processing displays a resolution in the order of 5 to 12° and 5 to 17 mm (Garling et al., 2008; Leardini et al., 2005). During function, human joints undergo rotations and translations the amplitude of which may be as small as a few degrees and millimeters. This is the case for those degrees of freedom that are stabilized by the passive periarticular structures and, as such, of special interest in clinical applications involving orthopedic reconstructive procedures (Freeman and Pinskerova, 2005). As a consequence, in these applications it is desirable that methods used to reconstruct these movements display resolutions in the order of 1° and 1 mm. If the objective is motor function assessment, lower resolutions may be acceptable.

Different joint constraints, which may be referred to as “hard” constraints, for use in MBO have been proposed and evaluated. The very first consisted in a spherical joint and was used to model

the lower limb (Lu and O'Connor, 1999). The knee joint has also been modeled as a hinge joint (Andersen et al., 2009; Moniz-Pereira et al., 2014; Reinbolt et al., 2005) and the ankle joint as a universal joint (Andersen et al., 2009; Moniz-Pereira et al., 2014; Reinbolt et al., 2005). Moreover, in order to better represent the interaction between the knee osteoarticular structures, coupling curves between the joint degrees of freedom (DoFs) (Li et al., 2012; Sandholm et al., 2011; Scheys et al., 2011; Sholukha et al., 2006b) and parallel mechanisms (Duprey et al., 2010; Valente et al., 2015) have been proposed.

The accuracy of kinematics that can be achieved using MBO and the above-mentioned joint models is still under debate (Andersen et al., 2010a; Clément et al., 2014; Gasparutto et al., 2015; Li et al., 2012; Stagni et al., 2009). Barring input data errors and STA, the accuracy of the estimated joint kinematics depends on how biofidelic the joint models are. In this respect, two means of improvement are possible. One way is to model joint constraints using subject-specific information derived from medical imaging (typically bone geometry). This method has been shown to have some beneficial effect on the results (Clément et al., 2015; Scheys et al., 2011; Valente et al., 2015). However, the techniques involved, such as MRI, bi-planar fluoroscopy, or bi-planar radiography, are cumbersome. When such experimental approach is not possible, the mathematical identification of the geometrical parameters of the model is used in some advanced MBO methods (Andersen et al., 2010b; Reinbolt et al., 2005). However, this identification remains limited to the position of spherical joint centers or the orientation of hinge joint axes. A second way of improving joint kinematics estimation is to introduce “soft” constraints and a penalty-based method (Gasparutto et al., 2015), thus accounting for ligament deformability and inter-individual differences. The use of “soft” constraints has been proposed for both the lower limb and the upper limb and provided promising results (Bolsterlee et al., 2014; Charbonnier et al., 2014; Gasparutto et al., 2015).

Making similar use of “soft” constraints, the objective of the present study is to introduce into the MBO another tool for modeling the osteoarticular structures: the joint stiffness matrix. Various notions of stiffness have been used in the literature and a terminology has been proposed to distinguish the different spring-like systems according to their physical nature and the method of measurement (Latash and Zatsiorsky, 1993). In this study, stiffness is defined as the characteristic of a 6DoFs elastic system, for which elastic forces provide resistance to the external forces, measured at equilibrium without energy dissipation. This definition of stiffness dispels confusion regarding *apparent stiffness* and *quasi-stiffness* (Latash and Zatsiorsky, 1993). Knee joint stiffness has been widely studied in the past (Caplan and Kader, 2014; Fox et al., 1998; Kanamori et al., 2000; Loch et al., 1992), but never considered as a joint constraint for the lower limb.

This study characterizes knee joint restraints by their elastic energy derived from the 6DoFs stiffness matrix. The assumption is that minimizing the deformation energy of these restraints during movement is a plausible physiological criterion that may provide more accurate kinematics estimates than obtained with the normally used above-mentioned models.

The present study is based on the following hypotheses. Given the acknowledged experimental errors and STA, (a) an improvement of the accuracy of the estimated knee kinematics can be obtained by introducing joint constraints, however (b) not those constraints that impede or prescribe joint displacements, and (c) the introduction of “soft” constraints based on a joint stiffness matrix represents an acceptable biofidelic solution. The accuracies with which joint kinematics can be estimated using the joint stiffness matrix and classical joint models, as embedded in MBO, were assessed and submitted to comparative analysis. This was done using STA affected data, collected during stair-ascent using stereophotogrammetry and skin-markers, and reference data, virtually free of STA, simultaneously acquired using bi-planar fluoroscopy. Bland-Altman analysis was conducted to substantiate the above-listed claims. Furthermore, for point (c), a sensitivity analysis was performed to confirm that a single stiffness matrix can be representative of knee joint restraints, despite variability due to joint movement, muscle loading and subject-specific factors.

2. Materials and methods

2.1. Multi-body optimization

MBO is a constrained minimization of the sum of the squared distances between measured and model-derived skin-marker positions. These distances are represented by driving constraints, Φ^m (Duprey et al., 2010). The MBO was applied to two segments (thigh and shank). The design variables of the optimization are the natural coordinates (Dumas and Chèze, 2007; Garcia De Jalon et al., 1994), \mathbf{Q}_i , consisting, for each body segment i , of two position vectors (proximal (P_i) and distal (D_i) endpoints of the segment) and two unitary direction vectors (\mathbf{u}_i perpendicular to the frontal plane of the segment and \mathbf{w}_i aligned with the mean flexion/extension axis of the distal joint) defining the position and orientation of segments: $\mathbf{Q}_i = [\mathbf{u}_i \quad \mathbf{r}_{P_i} \quad \mathbf{r}_{D_i} \quad \mathbf{w}_i]^T$. These natural coordinates are expressed in the global (inertial) coordinate system referred to as ICS (Figure 4.1). Since each segment is defined by 12 parameters representing the 6DoFs, rigid body constraints Φ^r (Dumas and Chèze, 2007) need to be considered.

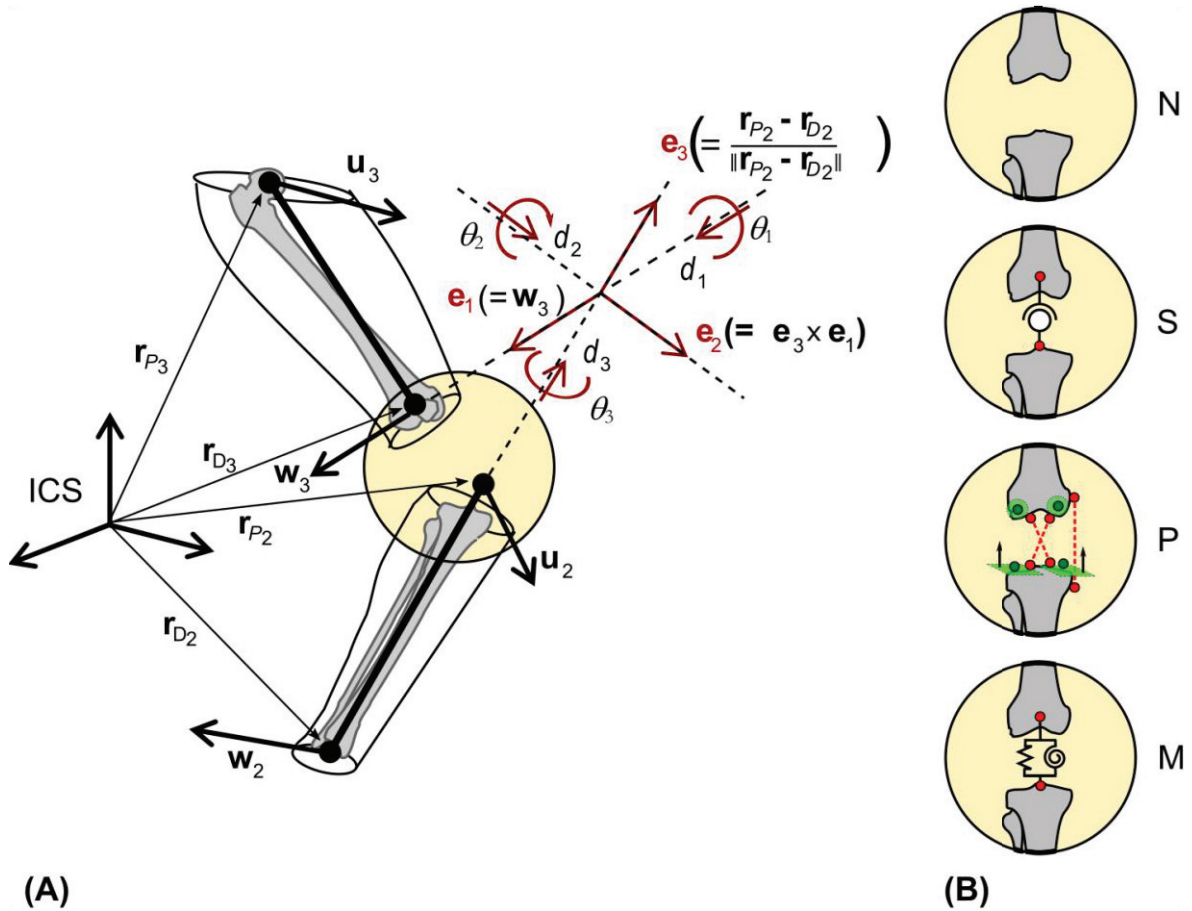


Figure 4.1 Model specifications.

(A) Natural coordinates, Q_i , for thigh ($i=3$) and shank ($i=2$) and knee joint coordinate system.

(B) Representation of the four different knee joint models, from top to bottom: no joint model (N), spherical model (S), parallel mechanism (P), and stiffness matrix (M).

There is also the issue regarding the kinematic constraints, Φ^k , in the different knee joint models dealt with in the present study. The first knee joint model (N) is characterized by no constraint. This represents a special case of MBO, namely a single-body optimization (SBO) for shank and thigh separately. The MBO is defined by:

$$\begin{aligned} \min_Q f &= \frac{1}{2} [\Phi^m]^T \Phi^m \\ \text{subject to } \Phi^r &= 0 \end{aligned} \quad (4.1)$$

The second knee joint model (S) is based on a spherical joint (Lu and O'Connor, 1999), and the third (P) on a parallel mechanism (Duprey et al., 2010). The MBO becomes:

$$\begin{aligned} \min_{\mathbf{Q}} f &= \frac{1}{2} [\Phi^m]^T \Phi^m \\ \text{subject to } &\begin{cases} \Phi^k = \mathbf{0} \\ \Phi^r = \mathbf{0} \end{cases} \end{aligned} \quad (4.2)$$

The fourth, and original, knee joint model (M) introduced in the present study is based on the knee stiffness matrix. The MBO is modified to include a deformation energy term:

$$\begin{aligned} \min_{\mathbf{Q}} f &= \frac{1}{2} \left([\Phi^m]^T \Phi^m + w [\mathbf{U} - \mathbf{U}_0]^T \mathbf{S} [\mathbf{U} - \mathbf{U}_0] \right) \\ \text{subject to } &\Phi^r = \mathbf{0} \end{aligned} \quad (4.3)$$

where $\mathbf{U} - \mathbf{U}_0$ is the difference between current and neutral joint angles and displacements, \mathbf{S} is the stiffness matrix, and w is a weighting factor.

In this study, the decision to impose the same order of magnitude on both terms of the objective function resulted in arbitrarily weighting the deformation energy term by a factor w set to 10^{-8} . The actual joint angles and displacements, $\mathbf{U} = [\theta_1 \ \theta_2 \ \theta_3 \ d_1 \ d_2 \ d_3]^T$, are computed from the natural coordinates \mathbf{Q} (Dumas et al., 2012b) and correspond to extension/flexion (EF), adduction/abduction (AA), and internal/external rotation (IER) angles and lateral/medial (LM), anterior/posterior (AP), and proximal/distal (PD) displacements, respectively. The goal is to conform to the joint coordinate system (JCS) definition ($\mathbf{e}_1, \mathbf{e}_2, \mathbf{e}_3$) (Wu et al., 2002). For consistency, the same axis definitions were used for MBO, stiffness matrix determination, and processing of validation data (Figure 4.1).

To describe knee joint movements, tibia and femur segment coordinate systems (SCSs) were defined following the recommendations of the ISB (Wu et al., 2002), which resulted in a direct relation between the natural coordinates, \mathbf{Q}_i , and the SCS axes:

$$\mathbf{R}_{0 \rightarrow i} = \begin{bmatrix} \mathbf{u}_i & (\mathbf{r}_{P_i} - \mathbf{r}_{D_i}) & \mathbf{w}_i \end{bmatrix} [\mathbf{B}_i^{\text{uv}}]^{-1} \quad (4.4)$$

with \mathbf{B}_i^{uv} being a constant transformation matrix (Dumas and Chèze, 2007).

The knee JCS was built by aligning the tibia and femur SCS axes in static position as acquired during the calibration phase. The rotation of the tibia with respect to the femur in this so-called aligned JCS was constructed as follows:

$$\mathbf{R}_{3 \rightarrow 2} = [\mathbf{R}_{0 \rightarrow 3}]^{-1} [\mathbf{R}_{0 \rightarrow 2} \mathbf{A}] \quad (4.5)$$

where $\mathbf{R}_{3 \rightarrow 2}$ is the rotation matrix defining the attitude of the tibia SCS with respect to the femur SCS, $\mathbf{R}_{0 \rightarrow 2}$ is the rotation matrix defining the attitude of the tibia SCS with respect to the ICS (directly related to the natural coordinates \mathbf{Q}_2) and $\mathbf{R}_{0 \rightarrow 3}$ is the rotation matrix defining the attitude of the femur SCS with respect to the ICS (directly related to the natural coordinates \mathbf{Q}_3). The alignment of both SCSs in static position is obtained by the matrix \mathbf{A} consisting of the coordinates of the axes $\mathbf{X}_2|_3$ $\mathbf{Y}_2|_3$ $\mathbf{Z}_2|_3$ of the tibia SCS in static position expressed in the femur SCS (Hagemeister et al., 2011).

2.2. Knee stiffness matrix

The stiffness matrix reflects the relation between the joint passive forces and moments \mathbf{F} and the joint angles and displacements \mathbf{U} . The stiffness matrix satisfies the general equation $\mathbf{F} - \mathbf{F}_0 = \mathbf{S}(\mathbf{U} - \mathbf{U}_0)$.

The present study relies on a single stiffness matrix, \mathbf{S} , based on cadaveric experiments (Lamberto et al., 2016) conducted to target a relative orientation between femur and tibia of 45° of flexion (i.e., fourth angle condition tested on the robot, as explained hereafter). Experiments were carried out at the Institute of Biomedical Engineering in Taiwan (National Taiwan University). A fresh-frozen knee joint was obtained from a 75-year-old female (151 cm, 47 kg). Ethical approval was granted by the Institutional Research Board of China University Hospital (Lamberto et al., 2016). The transepicondylar width was 73.6 mm, and the radii of lateral and medial condyles obtained by fitting two spheres on the condyles were 20 and 24 mm, respectively. The specimen, from mid-shaft femur to mid-shaft tibia, was dissected down to bone, leaving intact the major ligaments. The experimental measurements were performed using a Robot-based Joint Testing System (RJTS) consisting of an industrial robotic manipulator (RV-20A, Mitsubishi Electric Corporation, Japan) and a six-component load cell (UFS, Model PY6-100, Bertec Corporation, USA). The position and orientation repeatability of the robot were less than 0.2 mm and 0.2°, respectively. The three force and three moment components were measured thanks to the universal force-moment sensor along and about a Cartesian axis system the repeatability of which was within the range of 0.2 N for forces and 0.01 Nm for moments (Lamberto et al., 2016). A dedicated computer interface, embedding a Jacobian matrix-based algorithm (Fujie, 2015) was used to control both forces and moments, positions and orientations. Tests were carried out in seven EF angle configurations: 0, 15, 30, 45, 60, 75, and 90°. The measures were performed imposing incremental rotations and translations from neutral load equilibrium position of the knee joint, using a series of single DoF tests. Linear least-square minimization was used in post-processing to determine, for each EF angle,

the inverse of the stiffness matrix, namely the compliance matrix, while assuming a symmetric and positive matrix definition. Validation tests on the calculated matrices were carried out under a force control at 30° of EF, starting from the same neutral load position (Lamberto et al., 2016).

The axes of measurements in these experiments were consistent with those used for the joint angles and displacements estimated using MBO ($\mathbf{U} = [\theta_1 \ \theta_2 \ \theta_3 \ d_1 \ d_2 \ d_3]^T$). In particular, the control of the robotic arm was operated around the JCS axes ($\mathbf{e}_1, \mathbf{e}_2, \mathbf{e}_3$) (Fujie, 2015; Hsieh et al., 2015). On the tested cadaveric knee, the femur z-axis (\mathbf{e}_1 in the JCS) was aligned with the transepicondylar axis and pointed toward the medial epicondyle. The y-axis was defined as the projection of the femoral longitudinal axis onto the sagittal plane pointing to the distal part of the segment. The x-axis was defined perpendicular to both the y- and z-axes. The femur and tibia SCSs were considered to be coincident in the first angle condition (i.e., 0° of flexion) tested on the robot, as explained above. The y-axis of the tibia is thus \mathbf{e}_3 in the JCS.

The symmetrical stiffness matrix, determined at 45° EF angle, is given by:

$$\mathbf{S} = \begin{bmatrix} 869.5 & 2733 & 154.2 & 55.88 & -22.45 & 81.57 \\ & 8819 & 331.4 & 174.8 & -73.83 & 250.5 \\ & & 129.7 & 10.36 & -1.453 & 18.48 \\ & & & 3.895 & -1.620 & 5.330 \\ & Sym & & & 1.246 & -1.864 \\ & & & & & 8.063 \end{bmatrix} \times 10^2 \quad (4.6)$$

The neutral position should be understood as a position with minimum loads and does not imply null joint angles and displacements. The neutral joint angles and displacements, in degrees and mm, were $\mathbf{U}_0 = [46.59 \ -4.79 \ 11.68 \ -1.64 \ 3.21 \ 4.80]^T$. However, in order not to penalize EF in equation (4.3), the neutral value was replaced by the actual joint angle, θ_1 . \mathbf{S} was therefore reduced to the last five columns and lines of the matrix, taking no account of the coefficients relative to EF angle.

2.3. Validation data and procedure

The validation of the study was conducted through a comparative study between the accuracies of the four MBO methods using a Bland-Altman analysis. The question whether the use of a stiffness matrix determined at a single knee flexion angle (45° of flexion) is relevant for the estimation of the stair ascent cycle was also explored through a sensitivity analysis.

2.3.1. Experimental methods

In-vivo stair climbing experiments were carried out at the Institute of Biomedical Engineering in Taiwan (National Taiwan University, Institute of Biomedical Engineering, Taipei, Taiwan) on two healthy male subjects who provided informed written consent to participate in the study. Approval was provided by the local Institutional Human Research Ethics Committee (please note that underlying data are not publicly available due to lack of informed consent for data-sharing at the time of collection; however, interested researchers may request data to twlu@ntu.edu.tw and obtain a de-identified, minimal dataset pending ethical approval). The age, height and mass of the subjects S1 and S2 were 21 and 20 years, 176 and 164 cm, and 84 and 59 kg, respectively. The trajectories of ten skin markers on the right thigh (four markers at mid-thigh and two on the medial and lateral epicondyles) and shank (one marker each at the head of the fibula, tibial tuberosity and medial and lateral malleoli) were recorded using a 7-camera stereophotogrammetry system (Vicon, Oxford Metrics, UK), operated at 60 samples per second. Simultaneously, bone pose was recorded with bi-planar fluoroscopy. The frequency of acquisition of the fluoroscopes (with a 1020x932 image resolution) was 30 samples per second. Stereophotogrammetric and fluoroscopic data were acquired under the same experimental conditions (same protocol, laboratory, marker set, fluoroscopy registration method, movement) as in Tsai et al. (Tsai et al., 2011). The registration method was affected by the following errors (rmse \pm sd): 0.24 ± 0.77 mm for in-plane displacements, 0.41 ± 3.06 mm for out-of-plane displacements and $0.59 \pm 1.13^\circ$ for all rotations (Tsai et al., 2011).

Calibration of the reference position of the skin markers with respect to the femur and tibia was performed in a static position maintained by the subject at the beginning of the measurement session. The tibia and femur SCSs were considered to be aligned in the static position, as explained in the section *Multi-body optimization*. The coordinate systems based on 3D bone geometry were defined in the same way as on the cadaver knee (Lamberto et al., 2016).

The joint angles and displacements estimated using the four MBO methods and skin-marker data were compared to their respective reference values determined using the fluoroscopy data.

2.3.2. Sensitivity analysis

This sensitivity analysis addresses the variability of the coefficients that characterize the proposed stiffness matrix using statistical distributions, and explores the propagation of this variability to the tibiofemoral kinematics estimation using the proposed MBO method. Since the stiffness matrix applied to two different subjects was computed from experimental measurements involving a single cadaveric knee at 45° of flexion, there are several potential sources of variability. First, the stiffness

matrix was derived from a set of compliance matrices extracted with a range of angle conditions tested on the robot (0, 15, 30, 45, 60, 75, and 90° of flexion). However, a single stiffness matrix determined for a tibiofemoral joint presenting a flexion angle of 45° was applied to a stair climbing movement ranging from approximately 0 to 70° of flexion. Therefore, the influence of joint angle variations needs to be investigated. Second, the influence of loading conditions needs to be evaluated: the compliance matrix considered a single loading condition (almost unloaded condition), while the stair-climbing movement performed by the subjects involves varying knee loading conditions. Third, the differences between the specimen the stiffness matrix of which was used and the subjects whose movement was analyzed should be taken into account. Most of these sources of variation in the stiffness matrix coefficients are not properly quantifiable, thus, to address this issue, the amplitudes of the perturbations applied to the stiffness matrix coefficients were evaluated based on the expected largest variability. A maximum ratio of 50 was found between the coefficients of the seven compliance matrices determined at each angle conditions tested on the robot (Lamberto et al., 2016), while the ratio between the coefficients of the knee stiffness matrix in joint loading conditions ranging from 0 to 1800 N was found to be up to 10 (Marouane et al., 2013). The sensitivity analysis was conducted to cover the largest range of variation: a range of perturbation covering 5000% of the initial value of each coefficient was applied. The stiffness matrix contains a total of 25 coefficients, but, due to symmetry, only 15 of them (5 diagonal terms and 10 extra-diagonal terms) were considered. The sensitivity analysis consisted of perturbing the above-mentioned 15 coefficients using a Gaussian statistical distribution. The means of these distributions were assumed to be the stiffness matrix coefficients determined at 45° of flexion. A Latin hypercube sampling (LHS) method was used (El Habachi et al., 2015) to generate a set of $1.6 \cdot 10^6$ samples of perturbed coefficients. We tested for positive definiteness of the generated stiffness matrix in order to discard non-complying matrices. Finally, a run of 511 MBOs was performed, in keeping with the number of runs in previous sensitivity studies using LHS (Martelli et al., 2015; Valente et al., 2014). The Gaussian distribution of the perturbed coefficients was preserved for extra-diagonal terms of the stiffness matrix, while the distribution was truncated for diagonal terms. Indeed, these coefficients are strictly positive, resulting in the exclusion of negative terms. The actual distribution of the tested coefficients is provided in Figure 4.2. For consistency of the weighting factor w used for the deformation energy term in the MBO, each of the perturbed stiffness matrices was scaled with respect to the initial stiffness matrix defined at 45° of flexion using the ratio of traces.

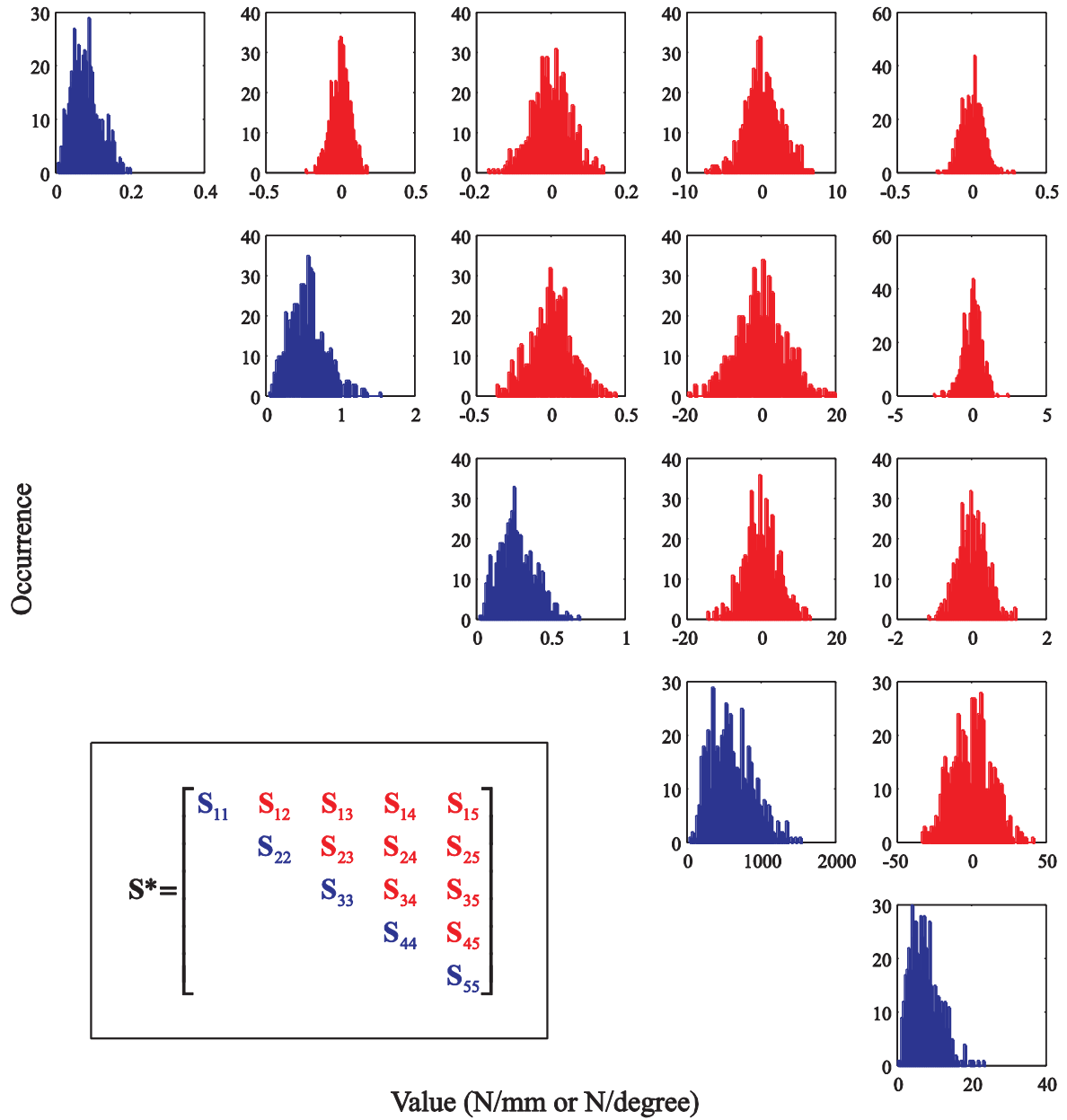


Figure 4.2 Distribution of coefficients of stiffness matrix samples

The problem is formulated as follows:

$$\min_{\mathbf{Q}} f = \frac{1}{2} \left(\left[\mathbf{\Phi}^m \right]^T \mathbf{\Phi}^m + [w \cdot \text{tr}(\mathbf{S})] [\mathbf{U} - \mathbf{U}_0]^T \left[\mathbf{S}^* / \text{tr}(\mathbf{S}^*) \right] [\mathbf{U} - \mathbf{U}_0] \right) \quad (4.7)$$

subject to $\mathbf{\Phi}^r = \mathbf{0}$

where \mathbf{S} is the initial stiffness matrix determined at 45° of flexion and \mathbf{S}^* is a perturbed stiffness matrix, and tr stands for the trace of the matrix.

2.3.3. Statistics

The hypotheses of the study were supported by Bland-Altman analysis (Bland and Altman, 1986; McLaughlin, 2013) of the knee joint kinematics estimated using MBO embedding each of the four knee joint models (N, S, P and M). The reference kinematics, determined using fluoroscopy, assumed to be a “gold-standard” acquisition system, was set as an invariant for comparison of the four model-based methods. Given this reference condition, the difference between model-derived kinematics and fluoroscopy-based kinematics was plotted against the reference value, instead of taking the mean difference over reference and each model-derived kinematics (as initially proposed for Bland-Altman analysis) (Krouwer, 2008). Consequently, to assess differences in the performance of the methods in the four models proposed, the Bland-Altman results for each model were compared. The method’s accuracy was given by the bias, and its precision was given by the standard deviation of the differences. Limits of agreement were set to 1.96 sd, providing an interval within which 95% of differences between model-derived and fluoroscopy-based are expected to lie. Rmse and correlation coefficients (r^2) were also reported.

With regard to the sensitivity analysis, joint angles and displacements estimated through MBO for the perturbed samples of stiffness matrix were represented by the mean of the kinematics estimations over the 511 runs. Two corridors of 1 and 1.96 sd respectively around the mean value illustrate how the perturbation propagates to the kinematics.

3. Results

3.1. Comparative analysis of the knee kinematics estimates

3.1.1. Bias

There was wide inter-model and inter-subject discrepancy in accuracy on knee joint angles and displacements (Figure 4.3, Figure 4.4 for subject S1 and S2, respectively). For EF in subject S1, the smallest bias was observed with model S (-0.1°) and the largest with model P (-2.0°), while with models N and M the bias was intermediate (-0.8 and -0.4° , respectively). In subject S2, the bias was -3.1° with model P, 0.2° with model M, and -0.4 and 0.9° with models N and S, respectively. For

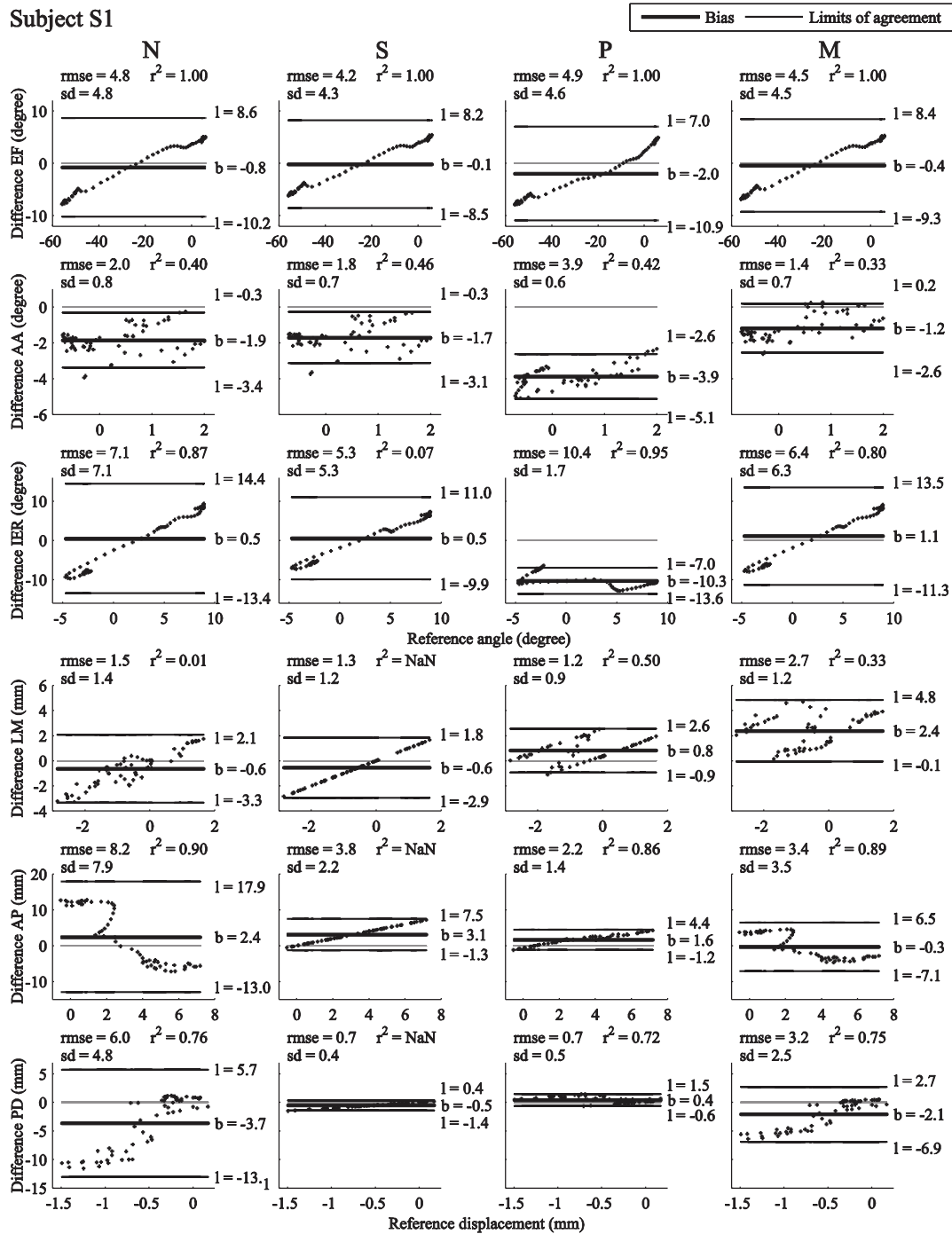


Figure 4.3 Bland Altman plot for subject S1.

Bland-Altman plot with reference kinematics (abscissas) and difference (ordinates) between model-derived and reference fluoroscopy-based kinematics. From left to right Bland-Altman plots for models N, S, P, M respectively, corresponding to joint angles and displacements, from top to bottom EF, AA, IER, and LM, AP and PD, respectively. Differences between model-derived kinematics and fluoroscopy-based kinematics are plotted against reference amplitude of movement (angle or displacement). Thick black line represents the bias (mean of the differences) whose value is designated by b , thin black lines represent the limits of agreement whose value is designated by $l = b \pm 1.96$ standard deviation. Squared Pearson's correlation coefficient (r^2), root mean square error (rmse) and standard deviation (sd) are displayed for each graph.

Subject S2

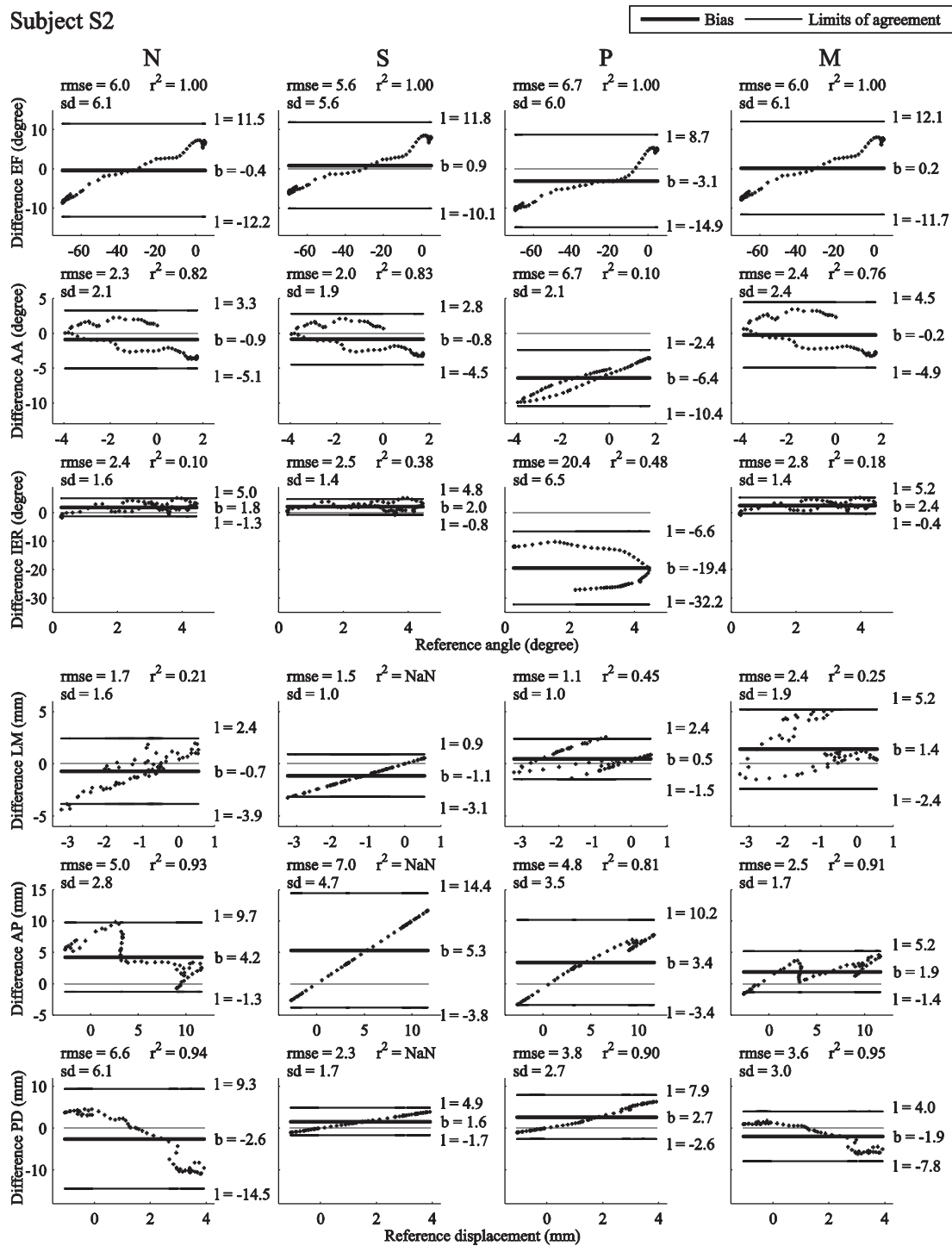


Figure 4.4 Bland Altman plot for subject S2.

Bland-Altman plot with reference kinematics (abscissas) and difference (ordinates) between model-derived and reference fluoroscopy-based kinematics. From left to right Bland-Altman plots for models N, S, P, M respectively, corresponding to joint angles and displacements, from top to bottom EF, AA, IER, and LM, AP and PD, respectively. Differences between model-derived kinematics and fluoroscopy-based kinematics are plotted against reference amplitude of movement (angle or displacement). Thick black line represents the bias (mean of the differences) whose value is designated by b , thin black lines represent the limits of agreement whose value is designated by $l = b \pm 1.96$ standard deviation. Squared Pearson's correlation coefficient (r^2), root mean square error (rmse) and standard deviation (sd) are displayed for each graph.

AA in both subjects, the smallest bias was found with model M (-1.2° for subject S1 and -0.2° for subject S2), and the largest bias was obtained with model P (-3.9 and -6.4° for subjects S1 and S2, respectively). With model N, bias was -1.9 and -0.9° for subjects S1 and S2, respectively, and with model S, bias was -1.7 and -0.8° for subject S1 and S2, respectively. For IER in subject S1, there was a bias of 0.5 , 0.5 , -10.3 and 1.1° with models N, S, P and M, respectively, and in subject S2 the bias was 1.8 , 2.0 , -19.4 and 2.4° with models N, S, P and M respectively. For LM, the bias was larger for subject S1 with model M (2.4 mm) than with models N (-0.6 mm), S (-0.6 mm) and P (0.8 mm), and larger for subject S2 with model M (1.4 mm) than with models N (-0.7 mm), S (-1.1 mm) and P (0.5 mm). For AP, the bias was smaller for subject S1 with model M (-0.3 mm) than with models N (2.4 mm), S (3.1 mm) and P (1.6 mm); the same was true for subject S2, where model M's bias was smallest at 1.9 mm, while models N, S and P showed a bias of 4.2 mm, 5.3 mm and 3.4 mm respectively. Finally for PD, the largest bias was found with model N for subject S1 (-3.7 mm) and with model P for subject S2 (-2.7 mm), while there was a bias of -0.5 , 0.4 , and -2.1 mm with models S, P and M, respectively, for subject S1 and of -2.6 , 1.6 , and -1.9 mm with models N, S and M respectively for subject S2.

3.1.2. Standard deviation

For EF, sd values were similar with all models, being smaller for subject S1 (4.8 , 4.3 , 4.6 , and 4.5° with models N, S, P and M, respectively) than for subject S2 (6.1 , 5.6 , 6.0 , and 6.1° with models N, S, P and M, respectively). For AA for subject S1, sd was under 1° with all models, while for subject S2, sd was similar with models N and P (2.1°), smaller with model S (1.9°) and larger with model M (2.4°). For IER, subject S1 showed a discrepancy between sd obtained with models N (7.1°), S (5.3°), P (1.7°) and M (6.3°), while subject S2 showed less discrepancy with models N, S and M (1.6 , 1.4 , and 1.4° respectively) and larger sd with model P (6.5°). Standard deviations obtained for LM were 1.4 , 1.2 , 0.9 , and 1.3 mm with models N, S, P and M, respectively for subject S1 and 1.6 , 1.0 , 1.0 , and 1.9 mm with models N, S, P and M, respectively for subject S2. AP for subject S1 showed larger sd with model N (7.9 mm) than with models S (2.2 mm), P (1.4 mm) and M (3.5 mm), whereas for subject S2, sd was larger with model S (4.7 mm) than with models N (2.8 mm), P (3.5 mm) and M (1.7 mm). Finally, for PD, both subjects showed larger sd with model N (4.8 and 6.1 mm respectively) and M (2.5 and 3.0 mm respectively) than with models S (0.4 and 1.7 mm respectively) and P (0.5 and 2.7 mm respectively). Note that very few differences in the Bland-Altman plot were outside the 95% confidence interval.

3.1.3. Root mean square error

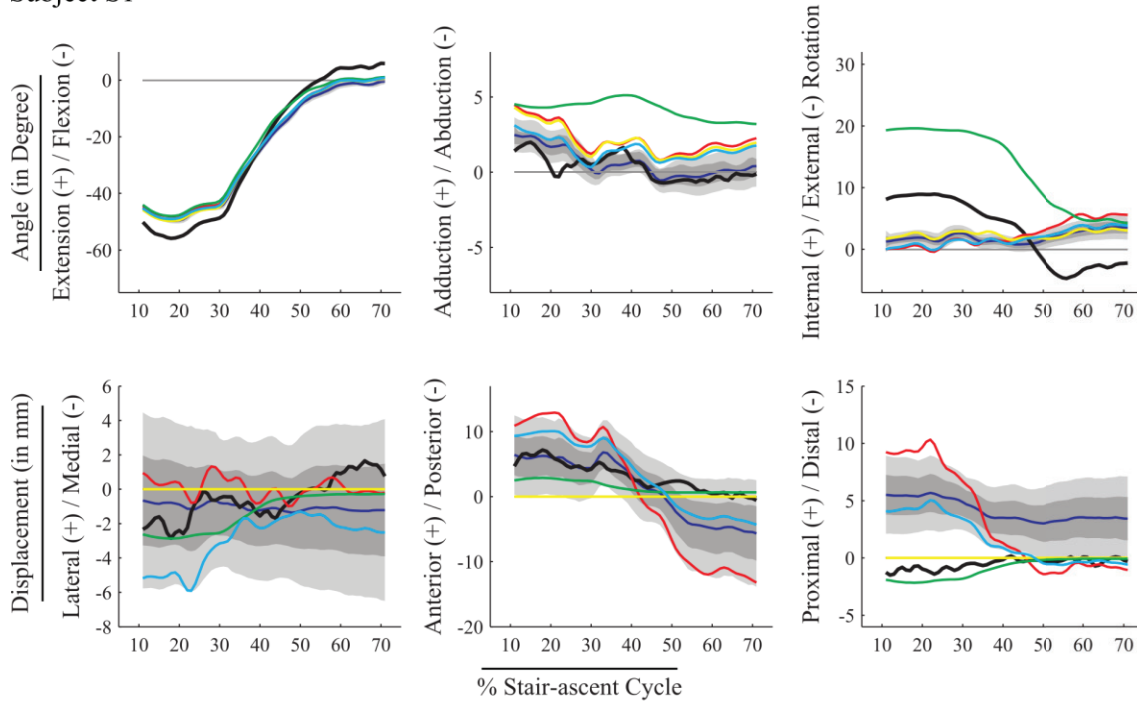
Similar rmse (Figure 4.3, Figure 4.4) were found for EF, with the four models between 4.2° (model S) and 4.9° (model P) for subject S1 and between 5.6 (model S) and 6.7° (model P) for subject S2. For AA, subject S1's rmse were lower with models N, S and M (2.0, 1.8, and 1.4°, respectively) than with model P (3.9°). Subject S2's rmse for AA were much higher with model P (6.7°) than with models N, S and M (2.3, 2.0, and 2.4, respectively). For IER, subject S1's rmse were higher with model P (10.4°) than with models N (7.1°), S (5.3°) and M (6.4°). Subject S2's rmse for IER were higher with model P (20.4°) than with models N (2.4°), S (2.5°) and M (2.8°). For LM in subject S1, the highest rmse was obtained with models M (2.7 mm), while models N, S and P had rmse of 1.5, 1.3, and 1.2 mm, respectively. In subject S2, the highest rmse were obtained with model M (2.4 mm), while rmse with models N (1.7 mm), S (1.5 mm) and P (1.1 mm) were lower. For subject S1, rmse for AP were 8.2, 3.8, 2.2, and 3.4 mm with models N, S, P and M, respectively, while for subject S2 they were 5.0, 7.0, 4.8, and 2.5 mm for models N, S, P, and M, respectively. For PD, there was wide discrepancy in results from the four knee joint models. For subject S1, rmse were between 0.7 (models S and P) and 6.0 mm (model N), with 3.2 mm for model M. For subject S2, rmse were between 2.3 (model S) and 6.6 mm (model N), with 3.6 mm for model M.

3.1.4. Correlation coefficient

The correlation coefficients were altogether high for both subjects S1 and S2 (Figure 4.3, Figure 4.4). For EF with all models, coefficients r^2 were close to 1. Coefficients r^2 were significantly lower for AA (from 0.33 for model M to 0.46 for model S) for subject S1, being much higher for subject S2 (from 0.76 for models M to 0.83 for model S), except for model P (0.10). For IER, coefficients r^2 were generally high for subject S1 (between 0.80 for model M and 0.95 for model P), except for model S (0.07). For subject S2, coefficients r^2 were generally lower than for subject S1 (0.10, 0.48 and 0.18 with models N, P and M, respectively), except with model S which gave slightly higher r^2 (0.38). For LM, coefficient r^2 was low, under 0.50 in both subjects S1 and S2 for models N, P and M. For AP, coefficients r^2 were close to 0.9 for subject S1, being highest for model N (0.90) and lowest for model P (0.86). For subject S2, coefficients r^2 were between 0.81 (model P) and 0.93 (model N). Finally, for PD, lower coefficients r^2 were observed for subject S1 (0.76 for model N, 0.72 for model P and 0.75 for model M) than for subject S2 (0.94 for model N, 0.90 for model P, and 0.95 for model M). Note that it was not possible to compute the correlation coefficient for displacements with model S.

It should be noted that a generally satisfactory estimation of kinematics with model M is obtained around 45° of flexion, the angle at which the stiffness matrix used was obtained.

Subject S1



Subject S2

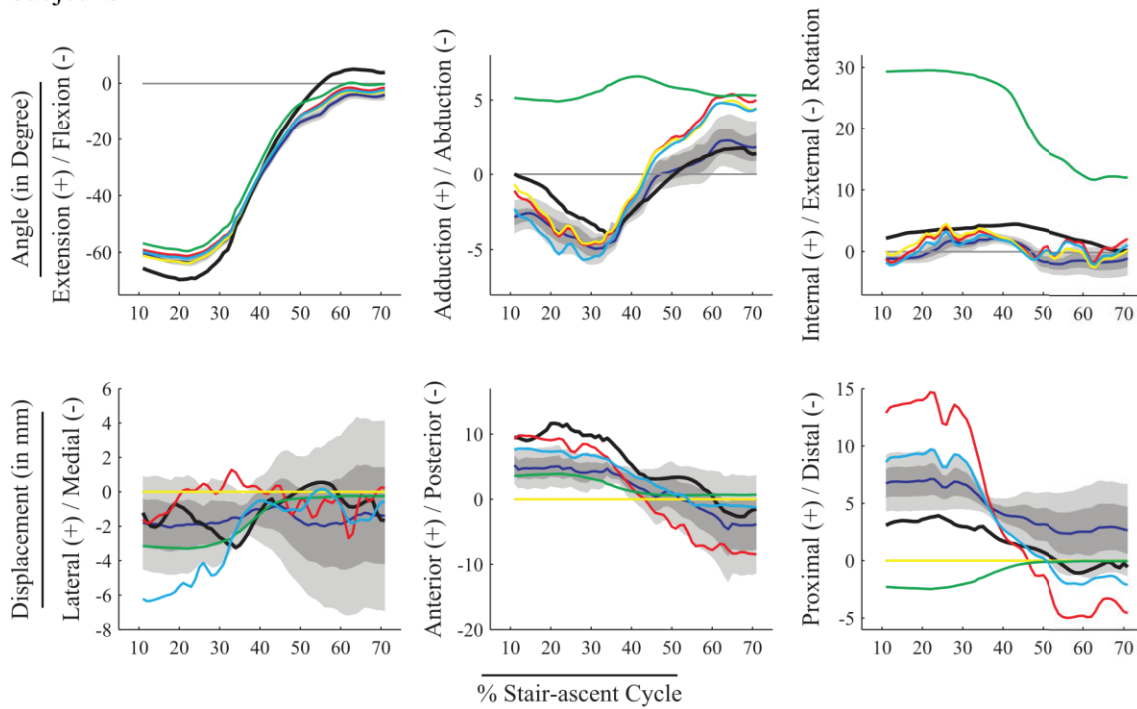


Figure 4.5 Knee joint angles and displacements, $U = [\theta_1 \theta_2 \theta_3 d_1 d_2 d_3]^T$ for both subjects.

Model-derived kinematics estimated with the four different knee joint models: no joint model (N, red), spherical model (S, yellow), parallel mechanism (P, green), and stiffness matrix (M, cyan) plotted against fluoroscopy-based kinematics (Ref, black). Sensitivity analysis results are represented by the mean of the kinematics estimation over the 511 runs of MBO embedding perturbed stiffness matrices (\bar{M}^* , dark blue), with corridor representing the variation in the estimation for one standard deviation (light grey, $\bar{M}^* \pm \text{sd}$) and 1.96 standard deviation ($\bar{M}^* \pm 1.96\text{sd}$, dark grey) around the mean value.

3.2. Sensitivity

The elastic joint model-derived kinematics embedding the initial stiffness matrix (M), as well as the mean (\bar{M}^*) and corridors of 1.1 ($\bar{M}^* \pm sd$) and 1.96 ($\bar{M}^* \pm 1.96 sd$) standard deviation of the elastic joint model-derived kinematics embedding the perturbed stiffness matrix, were computed for both subjects (Figure 4.5). The corridors were narrow for joint angles, with a maximum sd of 1.4° for EF and IER in subject S2, particularly for AA (0.7° for S1 and 0.9° for subject S2). Larger corridor amplitudes were observed for displacements, with a maximum sd for AP of 4.2 mm in both subjects S1 and S2. A significant difference was observed in patterns and values between the angles and displacements obtained with the initial stiffness matrix M (cyan in Figure 4.5) and the mean over the 511 runs on joint angles and displacements obtained with the perturbed stiffness matrices \bar{M}^* (dark blue in Figure 4.5). Curves for model M were generally within the corridor $\bar{M}^* \pm 1.96 sd$, except for LM and PD in subject S2.

4. Discussion

Although, virtually none of the methods tested provided joint angle and displacement estimates with the desirable resolution of 1° and 1 mm, the elastic joint proved to be a feasible alternative to other joint models for embedment in MBO and improvement of the relevant outcome. The comparative analysis of the results obtained using the four selected joint models supports the hypotheses formulated in the introduction.

The first hypothesis was that an improvement of the accuracy of the estimated knee kinematics can be obtained by introducing joint constraints and performing MBO. This hypothesis is supported by the analysis of the kinematics patterns and the Bland-Altman plots as well as the results on rmse. Overall, the method with model N yields poor agreement compared to the reference, with an average of absolute bias and standard deviation of $1.1 \pm 3.8^\circ$ and 2.4 ± 4.1 mm for joint angles and displacements, respectively, with the lowest values for EF ($0.6 \pm 5.5^\circ$) and LM (0.7 ± 1.5 mm). Furthermore, rmses are systematically high, relative to the amplitude of the joint angle or displacement considered. Kinematics estimation obtained from MBO embedding model N (i.e., SBO) actually reflects most of the STA, since there are no constraints to compensate for it (Bonci et al., 2015).

Our second hypothesis was that accurate knee kinematics cannot be obtained with joint constraints that impede or prescribe joint displacements. Indeed, using a spherical knee joint model, all displacements are set to zero arbitrarily, possibly resulting in better rmses but physiologically

meaningless (Clément et al., 2015; Gasparutto et al., 2015). Moreover, in the literature, the spherical knee joint model generally results in a higher level of errors compared to the errors found in the present study (Andersen et al., 2010a; Clément et al., 2015; Stagni et al., 2009). Likewise, the prescription of joint angles and displacements in model P led to even greater inaccuracy in the estimation of knee joint kinematics. Indeed, statistical analysis revealed a significant bias in the kinematics obtained with this model compared to the reference (average of absolute bias and standard deviation for rotations and displacements: $7.7 \pm 3.6^\circ$ and 1.6 ± 1.7 mm), which suggests a large systematic error. This assumption is supported by the shift observed in the kinematics plot (Figure 4.5), in particular for IER. Although model P is considered a physiological joint model (Duprey et al., 2010), it relies on “hard” constraints that prescribe two joint angles and three joint displacements, possibly resulting in high coefficients r^2 (IER for subjects S1 and S2), but also high rmse. This frequently occurs when using models based on anatomical features which require personalisation. Substantial systematic errors associated with high correlation has also been reported for an MBO that models the knee joint using coupling curves between DoFs (Li et al., 2012).

Our third hypothesis was that the introduction of “soft” constraints based on the joint stiffness matrix represents a promising trade-off. Introducing a stiffness matrix in MBO has previously been proposed for the spine (Koell et al., 2010; Marin et al., 2010), where no classic joint model is applicable. However, to the best of the authors’ knowledge, this approach has not been extended to other joints. Using “soft” constraints, as previously shown with deformable ligament in a parallel mechanism (Gasparutto et al., 2015), provides mixed results. The Bland-Altman analysis (Figure 4.3 and Figure 4.4), the rmse and the r^2 , showed that, overall, better agreement with the reference can be obtained with model M than with model N. The rmses obtained with models M and S are similar (average level of errors for rotations and displacements: $3.9 \pm 3.6^\circ$, 3.0 ± 2.3 mm and $3.6 \pm 3.2^\circ$, 2.8 ± 1.9 mm, respectively), and smaller than those obtained with models N and P (average level of errors: $4.1 \pm 3.8^\circ$, 4.8 ± 4.1 mm and $8.8 \pm 3.6^\circ$, 2.3 ± 1.7 mm, respectively). However, the Bland-Altman analysis also indicated that the limits of agreement with respect to the reference are slightly larger with model M than with model S, while the bias is more or less equivalent. This confirms that minimizing deformation energy represents at least an equally accurate alternative to the classic kinematic constraint (model S) for estimating knee joint angles such as EF and IER. The model based on the stiffness matrix also seems to estimate joint displacements efficiently (in particular for AP and PD) compared to model P. The advantage of characterising the knee joint by a stiffness matrix is the ability to define coupling between DoFs (i.e., extra-diagonal terms). The drawback lies in the introduction of a penalty-based method where the choice of the weight factor

w is critical. Here, in order to minimize errors on both skin marker trajectories and deformation energy, we chose to consider a similar contribution to the objective function for both terms. It would be possible to consider “softer” or “harder” constraints by adjusting the weighting factor.

The sensitivity analysis revealed that the model-derived kinematics is not very sensitive to perturbation of the stiffness coefficients, which supports the use of a single knee stiffness matrix (defined at 45 degrees of flexion) throughout. Compared to the outcome of previous global sensitivity analyses performed on lower-limb multi-body models (El Habachi et al., 2015; Martelli et al., 2015) taking into account the main parameters likely to influence performance, the stiffness matrix coefficients were shown to be less sensitive to perturbation. Model-derived kinematics have been reported to be sensitive to model parameter uncertainties, like orientation of joint axes, position of joint centers and origin, insertion and length of ligaments (in parallel mechanism) (El Habachi et al., 2015; Martelli et al., 2015). More detailed deformable knee models have also been found to be sensitive to ligament stiffness and reference strains (Lenhart et al., 2015). In the penalty-based method proposed here, the model-derived kinematics did not depend on the absolute, but rather on the relative values of the stiffness coefficients. This made it possible for the stiffness matrix to define coupling between DoFs. However, because of the positive definite property, the ratios between coefficient values are bounded. Therefore, the substantial variation in the stiffness matrix coefficient values depending on flexion angle (Lamberto et al., 2016) may slightly influence the accuracy of the method, without affecting the method’s convergence, nor its feasibility. Differences between the kinematics estimated with the initial stiffness matrix (\mathbf{M}) and the mean of the estimated kinematics over the 511 runs of MBO embedding the perturbed stiffness matrix ($\bar{\mathbf{M}}^*$) are also the consequence of the truncation of the distribution of the diagonal coefficients of the perturbed stiffness matrix.

This study is limited by the small number of subjects it considers. Moreover, the MBO method was applied to only two segments. However, as in other validation studies, reference kinematics data were available for thigh and shank only (Andersen et al., 2010a; Gasparutto et al., 2015). Further, the stiffness matrix was derived from a single cadaveric specimen. Such *in-vivo* validation data and *ex-vivo* modeling data are obviously difficult to obtain. Yet, while the inter-subject variability is not representative with only two subjects, the results of the present study confirms the feasibility of the method. Previous validation studies of MBO against fluoroscopy or pin data have been performed on two (Stagni et al., 2009) to ten (Clément et al., 2015; Li et al., 2012) subjects. Previous knee joint models, such as parallel mechanisms, have also been developed using data gathered from one cadaveric knee (Gasparutto et al., 2015).

Moreover, the authors purposely present a single stiffness matrix to focus attention on the feasibility of such joint modeling. This choice is supported by the results of the sensitivity analysis, which show that varying the stiffness matrix coefficients does not significantly affect the performance of the method. Nevertheless, the consequence of using a single stiffness matrix obtained at 45° of flexion is a good estimation of kinematics at this specific knee position. Future implementation of bilinear stiffness (i.e., different stiffness coefficients for opposite joint movement and especially for proximal/distal displacement) or of angle-dependent stiffness, in the same way as the previously proposed angle-dependent ligament length variation ([Bergamini et al., 2011](#)), may lead to more accurate estimation of knee joint kinematics. Ligament-deficient stiffness matrices may also be made available, as in ([Lamberto et al., 2016](#)), and embedded in MBO for application to pathological subjects.

To conclude, improvement of MBO accuracy and further personalization will necessarily follow from a better definition of joint models. In that regard, the present study allows us to foresee an alternative to the use of “hard” constraints in the multi-body method. The more physiological constraints implied by a penalty-based method (referred to as “soft” constraints) represent a progress toward making models more subject-specific.

Chapter 5. Simultaneous optimization of bone pose and soft tissue artefact model parameters through multi-body optimization: a feasibility study

1. Introduction

Estimating accurate skeletal kinematics is crucial for many application purposes. When performing non-invasive analysis, the use of stereophotogrammetry is quasi-systematic. However, as pictured in Chapter 2, optoelectronic systems present numerous limitations. Since the technology is ripe, improvement may be sought in post-processing methods. A particular attention must be paid to the inextricable issue embodied by the soft tissue artefact (STA). In fact, STA is reported to result from a combination of two contributions. Considering a marker-cluster on a segment, its transformation due to STA can be figured out as a change in shape or deformation (homothety and stretch), and a rigid transformation (translation and rotation) of the marker-cluster as a whole (Dumas et al., 2014). Recent studies showed that the main contribution to STA is the rigid transformation of the marker-cluster (Andersen et al., 2012; Barré et al., 2013; Grimpampi et al., 2014). As a consequence, the classic least squares bone pose estimators, based on the Procrustes superimposition approach, cannot fully compensate for the STA (Andriacchi et al., 1998; Ball and Pierrynowski, 1998; Challis, 1995; Chèze et al., 1995; Dumas and Chèze, 2009; Heller et al., 2011; Soderkvist and Wedin, 1993). With the willingness to improve kinematics and bone pose estimation using optoelectronic systems and skin markers, investigations have been conducted for decades to understand and handle the STA phenomenon (Leardini et al., 2005; Peters et al., 2010b). Nowadays, given the large number of studies in the literature investigating on the techniques for STA assessment and minimization, the community shows an increasing interest in the modeling of STA. Modeling STA is fundamental for its compensation and removal from skin marker trajectories in order to improve the accuracy of bone pose estimation.

It has been shown in Chapter 3 and Chapter 4 that multi-body optimization (MBO) embedding kinematic models for modeling the joints may improve joint kinematics and bone pose estimation as compared to single body optimization (SBO, also based on Procrustes superimposition approach). The impediment or prescription of DoFs imposed by these kinematic models prevents from dislocation while limiting the effects of STA (Lu and O'Connor, 1999). Nevertheless, the estimated kinematics obtained from model-based optimization remains inaccurate, and thus unsatisfactory. Even when the model is selected with care, it is not sufficient to compensate well for STA.

The objective of the present work was to investigate the feasibility and the efficiency of incorporating a model of the STA in the MBO. The feasibility of such a method involving bone pose and STA model parameters for a simultaneous optimization has been investigated in the past using SBO method (Alexander and Andriacchi, 2001) and MBO (Richard et al., 2012) but the final kinematics has never been validated. Following the idea that MBO may be an efficient tool for joint kinematics and bone pose estimation, the hypothesis was that wisely selecting the models embedded in the MBO may allow for an adequate STA compensation.

As mentioned above, the present study investigates the feasibility of estimating the parameters of a model of STA in the same time as femur and tibia pose. To this purpose, different STA models based on a modal decomposition (Camomilla et al., 2015) were introduced in the MBO. These models were designed in the perspective of limiting the number of the parameters embedded in the model, for computational efficiency. In the present work, the decision was made to embed four different STA models split in two categories depending on elementary transformation considered. Two of them approximated the STA by considering the rigid component of the marker-cluster, the STA field was reduced to rotation and translation modes (representing 6 parameters of amplitude for each segment). Indeed, the STA for a given marker is characterized at each instant of time as a vector by its amplitude and direction. Conversely, two models were composed of three rotation components only. Furthermore, for each of these first two categories, each of these models was aggregated with two different definitions of the amplitude of the STA. The first approach considered the amplitude as the parameters of the MBO, while the second approach considers the amplitude with a specific architecture. This architecture relies on a linear combination of the relevant joints adjacent to the considered body segment (shank or thigh), which coefficients were optimized in the MBO. Furthermore, the MBO is, of course, characterized by the embedded kinematic models at the joints, two models have been used for modeling the joints, no constraints (SBO) and spherical joints. The efficiency of models (i.e. joint model associated with a STA model) was evaluated depending on the results of joint kinematics and STA model estimation. The estimates of joint kinematics and STA models were compared to the reference kinematics reconstructed from pin data and classic MBO with no joint constraints and spherical constraints. The STA amplitudes have been previously evaluated using this reference kinematics (Camomilla et al., 2015). The study aimed at discriminating the different models with regard to their efficiency in estimating both kinematics and STA models parameters at the same time.

2. Materials and methods

2.1. Mathematical representation of the STA model

The mathematical formulation of STA used in the present study was depicted in [Dumas et al. 2014](#), to represent the pose, size and shape variations of a cluster of skin markers associated with a segment. This mathematical formulation aims at defining a general framework for the decomposition of the actual STA field on an adequate selected basis of directions in space. In the present study, the STA was unknown and its model parameters (either the amplitudes or the coefficients of the kinematic-driven architecture) represented the output of the optimization together with the bone pose. The mathematical formulation of STA was versatile and allowed to select any kind of orthogonal basis for modal definition of the STA. The decision for the present study was to consider a marker-cluster geometrical transformation definition with a rigid transformation only. This definition presents an easy interpretation as it considers rotations of the marker-cluster around the three axis of the segment coordinate system with the origin located at the centroid of the marker-cluster, and translations along the same axes. The procedure for the present model construction was the following: we built an arbitrary selected orthogonal basis of vectors representing preferential directions in space for the STA model amplitude for each mode (for instance rotation and translation components of the marker-cluster). STA was then reconstructed by adding the estimated components of the model.

The displacement of each marker j of segment i relative to the reference position was represented by the unknown vector $\mathbf{v}_i^j|_i(k)$ expressed in the segment coordinate system. As a whole, STA affecting the cluster of m_i markers was defined at every instant of time $k=1..n$ by an STA field:

$$\mathbf{V}_i(k) = \begin{bmatrix} \mathbf{v}_i^1|_i(k) \\ \vdots \\ \mathbf{v}_i^j|_i(k) \\ \vdots \\ \mathbf{v}_i^{m_i}|_i(k) \end{bmatrix} \quad (5.1)$$

The STA field $\mathbf{V}_i(k)$ defined the $3m_i$ DoFs of the problem. It originally represented the actual STA of the marker-cluster and can be projected on the selected arbitrarily orthogonal basis $\{\Psi_i^1 \dots \Psi_i^l \dots \Psi_i^{3m_i}\}$ representing the preferential directions in space, that suit the best the needs of the study. In our study, the STA field was unknown since it derives from the estimation

of the STA model parameters. As a consequence it represented the STA approximation estimated during the optimization process. The modal decomposition of the field of STA was (Figure 5.1):

$$\mathbf{V}_i(k) = \sum_{l=1}^{3m_i} a_i^l(k) \mathbf{\Psi}_i^l \quad (5.2)$$

The so-called mode amplitude $a_i^l(k)$ was unknown and was a parameter of interest in the study. The mode l was designated by $a_i^l(k) \mathbf{\Psi}_i^l$, representing the vector of STA along the specified mode l . The basis vector $\mathbf{\Psi}_i^l$ was known and built *a priori*.

In the case of a STA rigid component model, $\mathbf{V}_i(k)$ was approximated by six additive modes:

$$\mathbf{V}_i(k) = \sum_{l=1}^6 a_i^l(k) \mathbf{\Psi}_i^l \quad (5.3)$$

And the six unitary vectors $\mathbf{\Psi}_i^l$ were arbitrarily computed for $l = 1..6$ as:

$$\mathbf{\Psi}_i^l = \frac{\begin{bmatrix} (\mathbf{R}^l \mathbf{r}_{M_i^1}|_0} + \mathbf{t}^l) - \mathbf{r}_{M_i^1}|_0 \\ \vdots \\ (\mathbf{R}^l \mathbf{r}_{M_i^j}|_0} + \mathbf{t}^l) - \mathbf{r}_{M_i^j}|_0 \\ \vdots \\ (\mathbf{R}^l \mathbf{r}_{M_i^{m_i}}|_0} + \mathbf{t}^l) - \mathbf{r}_{M_i^{m_i}}|_0 \end{bmatrix}}{\left\| \begin{bmatrix} (\mathbf{R}^l \mathbf{r}_{M_i^1}|_0} + \mathbf{t}^l) - \mathbf{r}_{M_i^1}|_0 \\ \vdots \\ (\mathbf{R}^l \mathbf{r}_{M_i^j}|_0} + \mathbf{t}^l) - \mathbf{r}_{M_i^j}|_0 \\ \vdots \\ (\mathbf{R}^l \mathbf{r}_{M_i^{m_i}}|_0} + \mathbf{t}^l) - \mathbf{r}_{M_i^{m_i}}|_0 \end{bmatrix} \right\|} \quad (l = 1..3) \quad (5.4)$$

where \mathbf{r}_i^j was the position of the skin marker j ($j = 1..m_i$) embedded in the segment coordinate system with the origin at the centroid of the skin markers and with

$$\mathbf{R}^1 = \begin{bmatrix} 1 & 0 & 0 \\ 0 & \cos \theta & -\sin \theta \\ 0 & \sin \theta & \cos \theta \end{bmatrix} \quad (5.5)$$

$$\mathbf{R}^2 = \begin{bmatrix} \cos \theta & 0 & \sin \theta \\ 0 & 1 & 0 \\ -\sin \theta & 0 & \cos \theta \end{bmatrix} \quad (5.6)$$

$$\mathbf{R}^3 = \begin{bmatrix} \cos \theta & -\sin \theta & 0 \\ \sin \theta & \cos \theta & 0 \\ 0 & 0 & 1 \end{bmatrix} \quad (5.7)$$

$$\mathbf{R}^l = \begin{bmatrix} 1 & 0 & 0 \\ 0 & 1 & 0 \\ 0 & 0 & 1 \end{bmatrix} \quad (l = 4..6) \quad (5.8)$$

with $\theta = 0.02^\circ$ chosen arbitrarily, and

$$\mathbf{t}^l = \mathbf{0} \quad (l = 1..3) \text{ and } \mathbf{t}^4 = \begin{bmatrix} 1 \\ 0 \\ 0 \end{bmatrix}, \mathbf{t}^5 = \begin{bmatrix} 0 \\ 1 \\ 0 \end{bmatrix}, \mathbf{t}^6 = \begin{bmatrix} 0 \\ 0 \\ 1 \end{bmatrix}. \quad (5.9)$$

By construction, the basis vectors were all orthogonal.

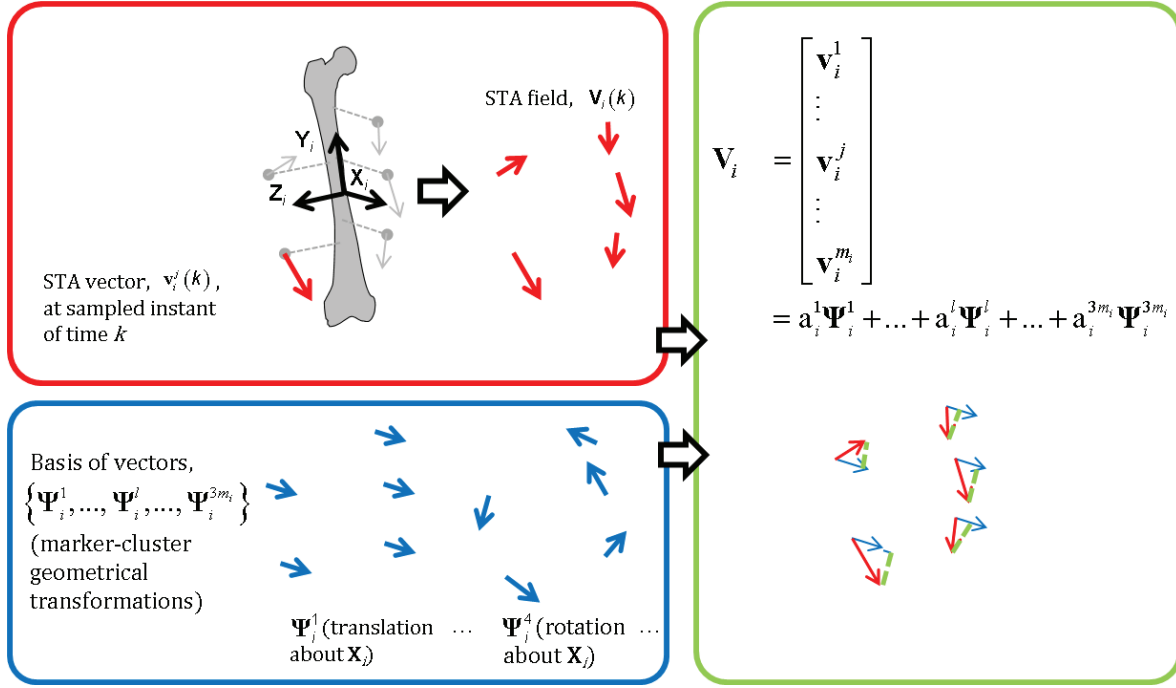


Figure 5.1 Framework for the mathematical representation of the STA

2.2. STA rigid component model

Given this considerations, the decision was made to model STA considering a marker-cluster as a deformable shape undergoing a geometric transformation embedding the STA rigid component. With this definition, the basis of vectors was built on six transformations only (three translations and three rotations). Thus, the basis was truncated and represented a STA subspace composed of six basis vectors. The method developed for simultaneous optimization of bone pose and STA model parameters was based on the MBO, in which STA model parameters were introduced as design variables in the same way as bone pose parameters (Richard et al., 2012). The study considered the thigh and shank using in-vivo running data (skin markers and intracortical pins markers, (Reinschmidt et al., 1997c)).

The present study followed the proposition to consider a STA rigid component model based on rotation and translation components of the cluster-marker representing six modes ($l = 1..6$)

(Camomilla et al., 2015). These basis vectors were built *a priori* in the segment coordinate system. Thus, the STA field was approximated by six additive modes:

$$\mathbf{V}_i(k) = \sum_{l=1}^6 a_i^l(k) \mathbf{\Psi}_i^l \quad (5.10)$$

The STA model embedding kinematics-based architecture within the amplitude became:

$$\mathbf{V}_i(\mathbf{\Lambda}_i(k)) = \sum_{l=1}^6 a_i^l(\mathbf{\Lambda}_i(k), \mathbf{h}_i^l) \mathbf{\Psi}_i^l \quad (5.11)$$

where $\mathbf{\Lambda}_i(k)$ represents the relevant joint angles and \mathbf{h}_i^l the model parameters vector as detailed below.

A specific architecture base on a linear combination of knee and hip joint angles was introduced, based on the experience with STA representation at individual marker level (Bonci et al., 2014; Camomilla et al., 2013). Hence, the amplitude $a_i^l(k)$ of mode l for thigh and shank was represented by a linear combination of relevant adjacent joint angles. This model was based on the assumption of a linear relationship between STA and relevant joint angles. The kinematics features involved in the model were assumed to impact the most on the artefact. For thigh and shank ($i = 2, 3$, respectively), the expression of the amplitude was modeled as:

$$a_2^l(\mathbf{\Lambda}_2(k), \mathbf{h}_2^l) = h_{2,\delta}^l \delta(k) + h_{2,\zeta}^l \zeta(k) + h_{2,\eta}^l \eta(k) \quad \mathbf{\Lambda}_2 = [\delta, \zeta, \eta] \quad (5.12)$$

$$a_3^l(\mathbf{\Lambda}_3(k), \mathbf{h}_3^l) = h_{3,\alpha}^l \alpha(k) + h_{3,\beta}^l \beta(k) + h_{3,\gamma}^l \gamma(k) + h_{3,\delta}^l \delta(k) \quad \mathbf{\Lambda}_3 = [\alpha, \beta, \gamma, \delta] \quad (5.13)$$

where $\mathbf{\Lambda}_i(k)$ represents the relevant joint angles; $\alpha(k)$, $\beta(k)$, $\gamma(k)$ are the components of the hip attitude vector, $\delta(k)$ is the knee orientation vector amplitude, and $\zeta(k)$, $\eta(k)$ are the components of the ankle orientation vector relative to the dorsi-plantar flexion and inversion-eversion axes. Coefficients \mathbf{h}_i^l were the model parameters (in a vector) to be optimized. The definition of the amplitude of STA introduced coupling laws between joint kinematics $\mathbf{\Lambda}$ and STA model parameters \mathbf{h} , which restraint the solution space. They act as constraints on the amplitude. This rigid component model with specific architecture for the amplitude was declined in four different versions. The model presented above was the first version. The model parameter number was 24 for thigh and 18 for shank respectively (for a total of 42 parameters). The second version considers the same six modes but considered directly the amplitudes as the parameters of the STA model instead of the coefficients \mathbf{h} . In other terms, no specific architecture was embedded in the definition of the amplitude. The model parameter number was 6 for thigh and shank respectively (for a total of 12 parameters). The third version considered only the three rotation component of the marker-cluster deformation, and resulted in a basis of vectors truncated to three modes $l = 1..3$

, embedding the specific amplitude architecture. The parameter number was 12 for thigh and 9 for shank respectively (for a total of 21 parameters). The fourth version considered the three rotation modes and no specific architecture for amplitudes. The model parameter number was 3 for thigh and shank respectively (for a total of 6 parameters). In the next sections, modes will be designated by the axis along which it is defined: we will consider rotation modes \mathbf{x} , \mathbf{y} and \mathbf{z} , and translation modes \mathbf{x} , \mathbf{y} and \mathbf{z} .

2.3. Multi-body optimization

The principle of the multi-body optimization embedding STA model is to estimate the bone pose and STA model parameters by minimizing a cost function composed of the difference between measured marker trajectories affected by the STA model and the model-derived marker trajectories. The models of STA was built in the segment coordinate system of thigh and shank respectively. The implementation of the models in the MBO implied to transform the STA vectors \mathbf{v}_i^j , defined in the segment coordinate system, in the reference coordinate system (ICS). The rotation matrix $\mathbf{R}_{0 \rightarrow i}(\mathbf{Q}_i)$ from segment coordinate system to reference coordinate system was computed from the bone pose parameters \mathbf{Q} defining the non-orthogonal segment coordinate system and the constant interpolation matrix $\mathbf{B}_i^{\mathbf{uv}}$ (Chapter 1) defining the transformation from the non-orthogonal segment coordinate system to the orthogonal coordinate system:

$$\mathbf{R}_{0 \rightarrow i} = \begin{bmatrix} \mathbf{u}_i & (\mathbf{r}_{P_i} - \mathbf{r}_{D_i}) & \mathbf{w}_i \end{bmatrix} [\mathbf{B}_i^{\mathbf{uv}}]^{-1} \quad (5.14)$$

with

$$\mathbf{B}_i^{\mathbf{uv}} = \begin{bmatrix} 1 & L_i \cos \gamma_i & \cos \beta_i \\ 0 & L_i \sin \gamma_i & \frac{\cos \alpha_i - \cos \beta_i \cos \gamma_i}{\sin \gamma_i} \\ 0 & 0 & \sqrt{1 - (\cos \beta_i)^2 - \left(\frac{\cos \alpha_i - \cos \beta_i \cos \gamma_i}{\sin \gamma_i} \right)^2} \end{bmatrix} \quad (5.15)$$

and

$$\begin{cases} L_i = \sqrt{(\mathbf{r}_{P_i} - \mathbf{r}_{D_i})^2} \\ \alpha_i = \cos^{-1} \left(\frac{((\mathbf{r}_{P_i} - \mathbf{r}_{D_i}) \bullet \mathbf{w}_i)}{L_i} \right) \\ \beta_i = \cos^{-1} (\mathbf{u}_i \bullet \mathbf{w}_i) \\ \gamma_i = \cos^{-1} \left(\frac{(\mathbf{u}_i \bullet (\mathbf{r}_{P_i} - \mathbf{r}_{D_i}))}{L_i} \right) \end{cases} \quad (5.16)$$

Using the parameter set and systems of coordinates detailed in Chapter 1, the driving constraints Φ^m dependent in time were defined as follow:

$$\Phi^m = \begin{cases} \mathbf{r}_{M_2^1}^{\wedge} \Big|_0 - (\mathbf{R}_{0 \rightarrow 2}(\mathbf{Q}_2) \mathbf{v}_2^1 \Big|_2) - \mathbf{N}_2^{M_2^1} \mathbf{Q}_2 = \mathbf{0}_{3 \times 1} \\ \vdots \\ \mathbf{r}_{M_2^{m_2}}^{\wedge} \Big|_0 - (\mathbf{R}_{0 \rightarrow 2}(\mathbf{Q}_2) \mathbf{v}_2^{m_2} \Big|_2) - \mathbf{N}_2^{M_2^{m_2}} \mathbf{Q}_2 = \mathbf{0}_{3 \times 1} \\ \vdots \\ \mathbf{r}_{M_3^1}^{\wedge} \Big|_0 - (\mathbf{R}_{0 \rightarrow 3}(\mathbf{Q}_3) \mathbf{v}_3^1 \Big|_3) - \mathbf{N}_3^{M_3^1} \mathbf{Q}_3 = \mathbf{0}_{3 \times 1} \\ \vdots \\ \mathbf{r}_{M_3^{m_3}}^{\wedge} \Big|_0 - (\mathbf{R}_{0 \rightarrow 3}(\mathbf{Q}_3) \mathbf{v}_3^{m_3} \Big|_3) - \mathbf{N}_3^{M_3^{m_3}} \mathbf{Q}_3 = \mathbf{0}_{3 \times 1} \end{cases} \quad (5.17)$$

With $\mathbf{r}_{M_i^j}^{\wedge} \Big|_0$ the measured position marker j ($j = 1..m_i$) of the segment i ($i = 2, 3$), $\mathbf{R}_{0 \rightarrow i}(\mathbf{Q}_i) \mathbf{v}_i^j \Big|_i$ the STA vector of marker j of segment i expressed in the reference coordinate system (thanks to the rotation matrix $\mathbf{R}_{0 \rightarrow i}(\mathbf{Q}_i)$ from segment coordinate system to reference coordinate system), $\mathbf{N}_i^{M_i^j} \mathbf{Q}_i$ the model determined marker position.

The implementation of the four STA models in MBO required two different formalisms of the problem depending on the parameters of the STA model. The first group of models was dealing with the amplitude of the STA driven by a specific architecture. Each amplitude component was a linear combination of the adjacent joint angles, where coefficients of the linear combinations \mathbf{h}_i^l are the output parameters of the STA model identification. Indeed, \mathbf{h} parameters are constant over the time, while amplitudes $a_i^l(k)$ (as well as joint angles $\Lambda_i(k)$) are time-dependent. This implied the use of a two-level optimization (Reinbolt et al., 2005). An outer loop concerned the optimization whose design variables were the parameters \mathbf{h} . An inner loop considered the natural coordinates $\mathbf{Q}(k)$ as design variables while both parameters \mathbf{h} and values of joint angles involved in the STA model were considered constant. In particular, coefficients \mathbf{h} participated in the

expression of amplitudes $a_i^l(k)$ through equations (5.12) and (5.13). Furthermore, in this first feasibility study, the values of joint angles considered onto the computation of amplitudes were not updated at each iteration but computed from the prior bone pose estimation obtained with MBO embedding spherical joint constraints before entering the optimization process. The inner loop consisted in the following optimization problem:

$$\begin{aligned} \min_{\mathbf{Q}(k)} f &= \frac{1}{2} \left(\Phi^m(\mathbf{Q}(k))^T \Phi^m(\mathbf{Q}(k)) \right) \text{ with given } \mathbf{h}, \Lambda_i(k) \\ \text{subject to } &\begin{cases} \Phi^k = 0 \\ \Phi^r = 0 \end{cases} \end{aligned} \quad (5.18)$$

Where Φ^m , Φ^k , Φ^r are driving constraints, kinematic constraints and rigid-body constraints, respectively (Duprey et al., 2010).

While for the outer loop the optimization problem was:

$$\min_{\mathbf{h}} f = \frac{1}{2n} \sum_{k=1}^n \left(\Phi^m(\mathbf{h})^T \Phi^m(\mathbf{h}) \right) \text{ with given } \mathbf{Q}(k), \Lambda_i(k) \quad (5.19)$$

The second group of models was considering the amplitude of the STA model without specific architecture. This problem was solved by a frame-by-frame Gauss-Newton algorithm since all parameters were time-dependent. In other words, the output parameters of the optimization were the natural coordinates $\mathbf{Q}(k)$ and the amplitudes $a_i^l(k)$ at each sampled instant of time. The optimization performed for the bone pose estimation was:

$$\begin{aligned} \min_{\substack{\mathbf{Q}(k) \\ \mathbf{a}(k)}} f &= \frac{1}{2} \left(\Phi^m(\mathbf{Q}(k), \mathbf{a}(k))^T \Phi^m(\mathbf{Q}(k), \mathbf{a}(k)) \right) \\ \text{subject to } &\begin{cases} \Phi^k = 0 \\ \Phi^r = 0 \end{cases} \end{aligned} \quad (5.20)$$

The different models of STA were implemented in the MBO considering shank and thigh with the aim to evaluate the ability of different models of STA combined with different joint constraints to estimate knee joint kinematics with STA compensation. Thus, in addition to the analysis of those four STA models (both types of rigid component models with and without specific architecture to model amplitude), the study also considered two modeling approach in terms of joint constraints embedded in the MBO. In this purpose, two types of joint constraints have been tested: no joint constraint (N) for ankle, knee and hip (SBO), and spherical constraints (S) to the ankle, knee and hip. The method will be referred as \mathbf{S}_n^h and \mathbf{S}_n^a ($n=3$ or $n=6$ depending on the number of modes selected in the model) for the STA models with and without the angle-dependent architecture for

amplitude respectively, considering spherical constraints at the joints. It will be referred as N_n^h and N_n^a ($n = 3$ or $n = 6$ depending on the number of modes selected in the model) for the STA models with and without the angle-dependent architecture for amplitude respectively, considering no joint constraint. The initial solution of the different optimizations was, in all cases, the result of a previous optimization performed without STA model and with spherical joints (S) at the ankle, knee and hip.

2.4. Validation data and procedure

To investigate the efficiency of implementing a STA model in MBO, the pin- and skin-marker data acquired by [Reinschmidt et al. \(1997c\)](#) were used. Three healthy male subjects (S1, S2, S3; age 27.7 ± 2.1 years; weight 85.5 ± 9.6 kg; height 186 ± 10 cm) were analyzed while running at slow speed (2.9 ± 0.2 m/s). Three clusters of three markers each attached to an intracortical pin were inserted into the postero-lateral aspect of the right calcaneus, lateral tibial condyle and lateral femoral epicondyle. In addition, the subjects were equipped with five skin markers glued on the thigh and six on the shank. The stance phase of five running trials were acquired for each subject using a three film camera system (sampling frequency: 200 frames/s). The anatomical calibration using a radiostereometric analysis ([van den Bogert et al., 2008](#)) was used to define reference thigh and shank anatomical frames. The foot frame was defined as parallel to the global frame while standing. The reference pose of these three anatomical frames were estimated through a Procrustes approach ([Soderkvist and Wedin, 1993](#)), at each instant of time during the movement. The anatomical frame for the pelvis has been arbitrarily assumed to be always parallel to the global frame while the position of the hip joint center was fixed at the proximal endpoint of the thigh ([Camomilla et al., 2015](#)). To investigate the efficiency of the estimation of both bone pose and STA model parameters simultaneously, different aspects were analyzed in terms of kinematics and STA compensation.

2.5. Evaluation of STA model implementation and MBO effectiveness

The main objective of the study was to evaluate the effectiveness of the MBO method to estimate STA model parameters and bone pose in the same process. Given the initial proposition to implement the model N_6^h , which STA model considers six rigid modes and the joint angles architecture for amplitude in SBO (i.e. MBO with no joint constraints), we proposed to investigate the feasibility of implementing the latter model as well as its possible sub-options. By comparing different models for STA and joints, we aimed at comforting the approach proposed in [Camomilla](#)

et al. (2015) (model N_6^h) in its ability to provide the most accurate estimate of STA model while improving joint kinematics estimation in comparison to other versions of the model (S_6^h , N_3^h , S_3^h , N_6^a , S_6^a , N_3^a and S_3^a). A particular attention has been paid to the comparison between STA model approach considering amplitudes architecture, with \mathbf{h} in the design variables, and STA model approach considering mode amplitudes as design variables, without a specific architecture for the STA model. The evaluation of the different STA models tested in the present work were conducted in two phases. First, a qualitative description of the results to discriminate relevant models was performed. Second, a quantitative study on the selected models was performed on the results to conclude on the effectiveness of the method.

Concerning the joint kinematic models, the decision to introduce a spherical model rather than more detailed models (as elastic joint model (Chapter 2) or parallel mechanism (Duprey et al., 2010; Gasparutto et al., 2015)) was supported by previous study concluding in the relative efficiency of spherical joint to model the knee joint. In particular for this set of data, it has been shown that spherical joint provided a better accuracy in estimating knee joint kinematics than other models (Gasparutto et al., 2015). We focused on the knee joint kinematics to evaluate the efficiency of the models to predict bone pose since it is the joint adjacent to both shank and thigh. Obviously, the hip and ankle joints influenced the results obtained with models N_6^h , S_6^h , N_3^h and S_3^h . Nevertheless modeling the hip joint with spherical joint is current in the literature. Concerning the ankle, it influenced the bone pose and amplitude estimation on the shank, but the observation of knee kinematics provided sufficient information to discriminate models.

2.6. Part 1: Overview and selection of relevant models

In this part, consisting in a preliminary selection of relevant models, all the models presented above were implemented into the MBO.

2.6.1. Objectives and procedure

MBO was performed for each combination of STA model and joint kinematics model presented below on one trial for each of the three subjects (S1, S2 and S3). An overview on the results on kinematics and models parameters permitted to eliminate irrelevant models. In regards to the similarity of the observations over the three subjects, only a typical trial of one subject is presented in this section. Some models caused computational issues when implemented in the MBO. Since the optimization process involving models S_6^a , N_6^h and N_3^a did not converge, these models were simply discarded from the study. For this typical subject, we focused on the kinematics patterns for models N_6^h , S_3^h , S_3^a , N_3^h relative to the kinematics obtained with model N and S (without any

STA model) and reference. The observations on kinematics patterns were corroborated by the observations on the amplitude of modes composing the models. As said before, the amplitudes and the coefficients of coefficients of the kinematic-driven architecture have been previously evaluated on this reference kinematics (Camomilla et al., 2015).

2.6.2. Results

2.6.2.a. STA rigid component model approximated by six modes

For a better legibility, the presentation of results deriving from the tested models have been split in two groups depending on the number of modes involved in the approximation of STA. We referred to different modes with the name of the axis along which it is defined, for instance, the modes of the rigid components model will be referred as mode **x**, mode **y** and mode **z** for rotation and translation. Looking at STA rigid component models considering rotations and translations (six modes), with a group reduced to model N_6^h , the kinematics patterns (Figure 5.2) shows that this model was unable to reproduce accurately any angle or displacement at the knee. It provided kinematics estimation particularly distant from reference regarding to classic MBO (embedding model S as well as N). It is especially visible for joint displacements. In terms of pattern, only extension-flexion presented similarities with the curves obtained from reference and

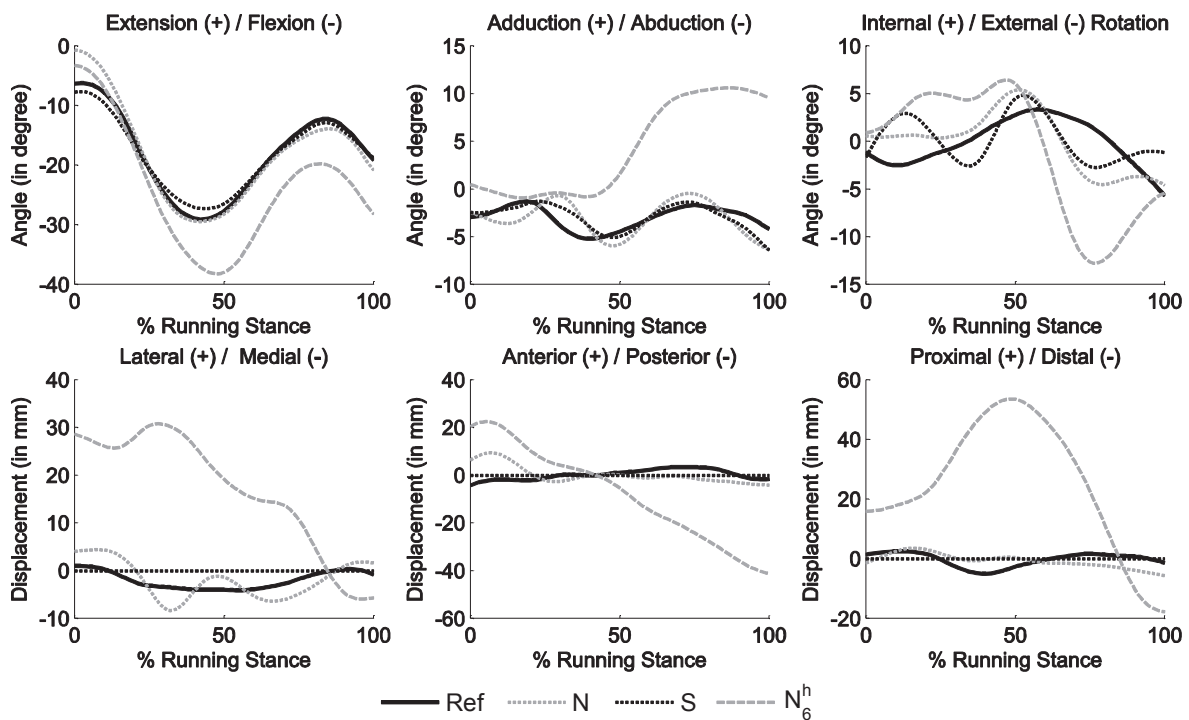


Figure 5.2 Knee joint kinematics model N_6^h .

Plot for one trial of a typical subject resulting from MBO embedding model N_6^h against MBO embedding models N and S and reference kinematics.

models N and S. Still, even for extension-flexion, the angle and displacement amplitudes reflected aberrant behavior of the joint.

STA amplitudes obtained from MBO with model N_6^h were compared against reference derived from the calibration of the STA model for shank (Figure 5.3) and thigh (Figure 5.4). The time histories of the amplitude for each mode revealed very important inaccuracy of the estimated amplitudes. For the shank, the patterns of the amplitude on rotation mode about \mathbf{x} and translation modes along \mathbf{y} and \mathbf{z} were almost symmetrical at each instant of time, relative to zero. For this modes and the translation mode \mathbf{z} , the magnitude (pick-to-pick) of the time histories of the amplitude were similar for the estimate and the reference. Outlier amplitudes were observed for rotation modes about \mathbf{y} and \mathbf{z} .

For the thigh, none of the observations depicted for the shank was confirmed. Except that all the estimated amplitudes were significantly far from reference both in amplitude values and patterns (Figure 5.4). In addition to the opposite curve for some modes (rotation mode \mathbf{x} , translation modes \mathbf{y} and \mathbf{z}), the curves were shifted for all modes from about 3mm up to 11mm relative to the reference values.

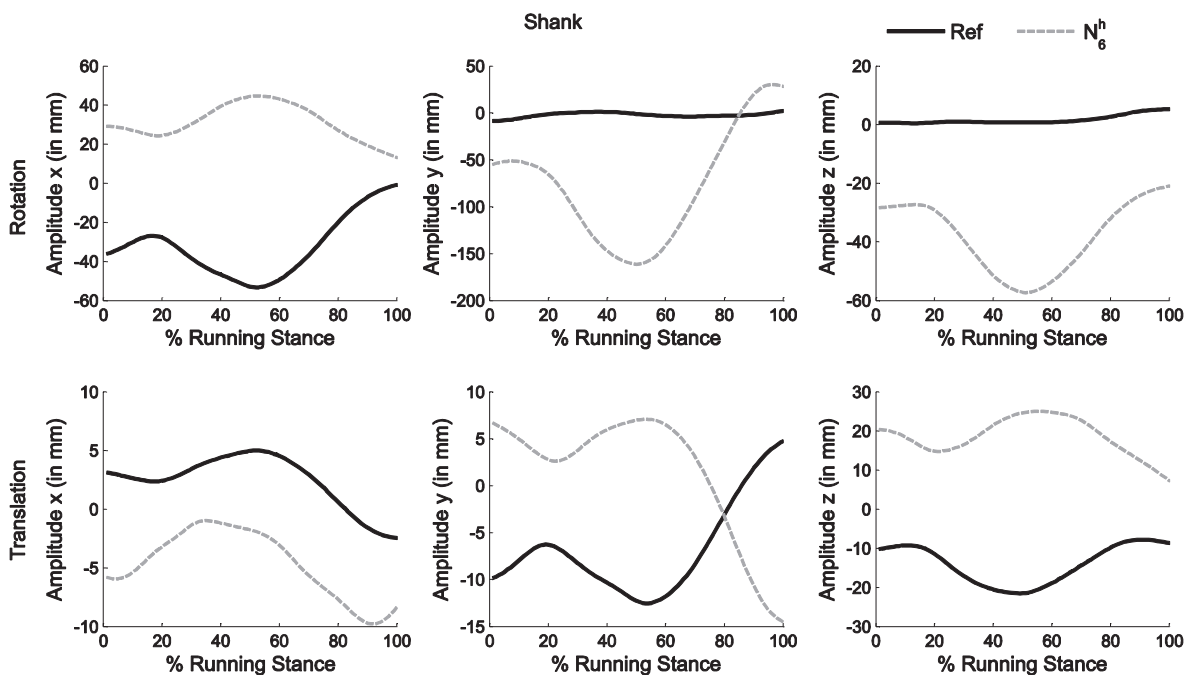


Figure 5.3 Amplitude estimate's time histories for model N_6^h .

Plot for the shank for one trial of a typical subject resulting from MBO embedding model N_6^h against reference amplitude.

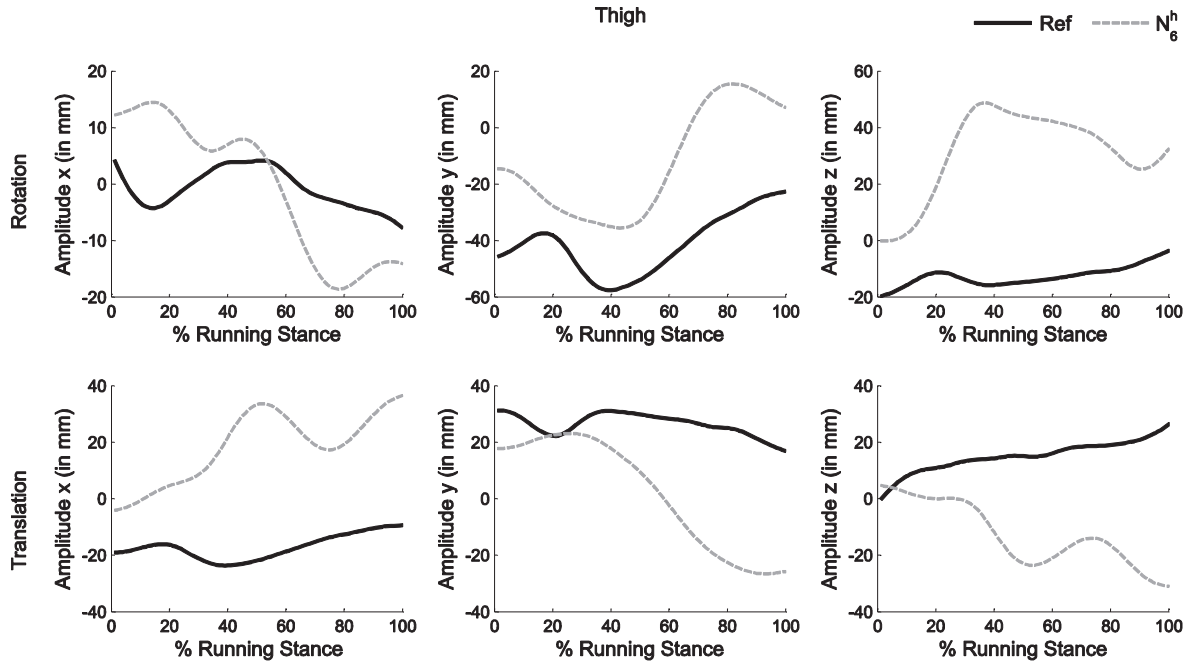


Figure 5.4 Amplitude estimate's time histories for model N_6^h .

Plot for the thigh for one trial of a typical subject resulting from MBO embedding model N_6^h against reference mode amplitudes.

2.6.2.b. STA rigid component model approximated by three modes

For joint angle kinematics estimation resulting from MBO embedding the models represented by three rotation modes (S_3^h , N_3^h and S_3^a), we observed that the model considering no joint constraint (N_3^h) provided the most distant curve from reference in comparison to models N , S , S_3^h and S_3^a (Figure 5.5). The curves obtained from MBO with model S_3^h was slightly closer to the one obtained with model S than with model S_3^a .

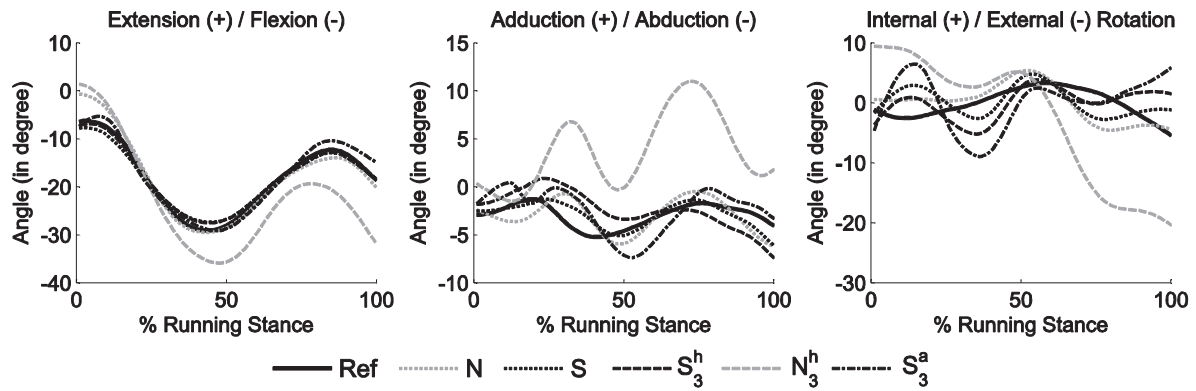


Figure 5.5 Knee joint angle kinematics for models S_3^h , N_3^h and S_3^a .

Plot for one trial of a typical subject resulting from MBO embedding models S_3^h , N_3^h and S_3^a against MBO embedding models N and S and reference kinematics.

The estimation of STA amplitude of rotation modes during the stance phase of running was depicted in Figure 5.6. The overall estimated curves of amplitude were found far from the reference. Concerning the rotation modes for the shank, the time history amplitude of mode **x** obtained with models S_3^h and S_3^a were closer from the reference than with model N_3^h , without significant difference between them. For mode **y**, model S_3^a provided the most distant estimate from reference, after N_3^h and particularly S_3^h . For mode **z**, no significant difference was observed between the three models, the curve obtained with S_3^h was still slightly closer to reference.

Concerning the rotation modes for the thigh, for modes **x** and **z**, models S_3^h and S_3^a were similar and closer to the reference than model N_3^h . For the mode **y**, results were mitigatory but globally unsatisfactory.

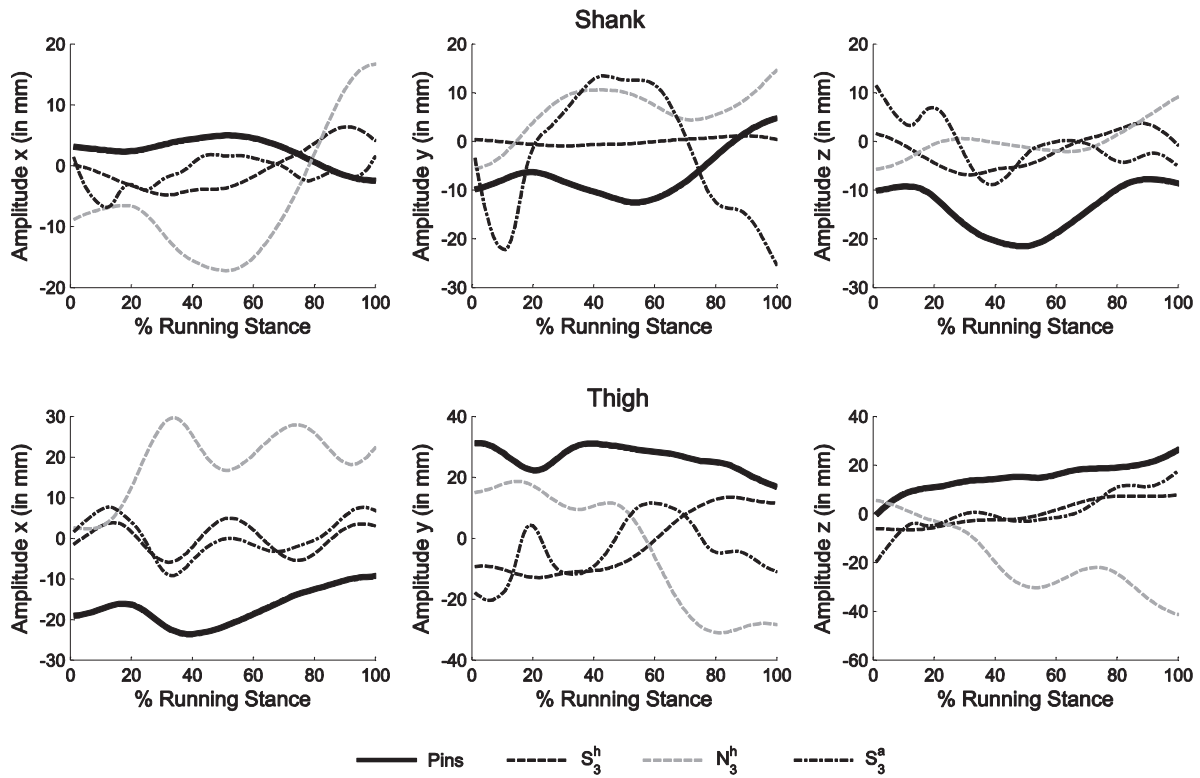


Figure 5.6 Amplitude estimate's time histories for models S_3^h , N_3^h and S_3^a .

Plot for the shank (top) and thigh (bottom) for one trial of a typical subject resulting from MBO embedding models S_3^h , N_3^h and S_3^a against reference mode amplitudes.

For models S_3^h and N_3^h , the comparison of the parameters \mathbf{h} of the STA modeled amplitude were possible against the reference parameters calibrated from intracortical pin data (Camomilla et al., 2015) (Figure 5.7).

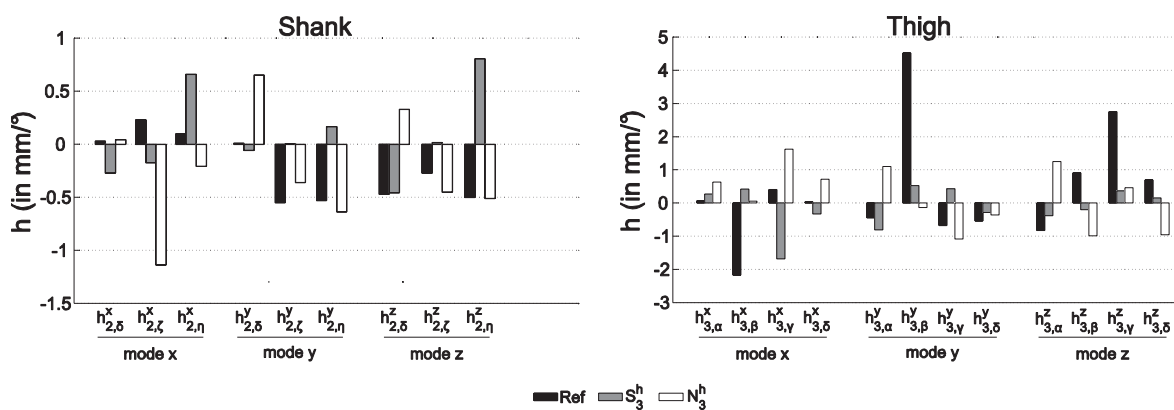


Figure 5.7 Amplitude model parameters \mathbf{h} estimate for model S_3^h and N_3^h .

Plot for the shank (left) and thigh (right) for one trial of a typical subject resulting from MBO embedding model S_3^h and N_3^h against reference amplitudes amplitude model parameters.

The first observation was that all the estimated values were more or less in the same order of magnitude as the reference values. Nevertheless, there was a lot of discrepancy between all the coefficients. In particular, the sign of the coefficients was often opposed to the one of the reference : with model S_3^h for $h_{2,\delta}^x$, $h_{2,\zeta}^x$, $h_{2,\delta}^y$, $h_{2,\zeta}^y$, $h_{2,\eta}^y$, $h_{2,\zeta}^z$ and $h_{2,\eta}^z$ for the shank, and $h_{3,\beta}^x$, $h_{3,\gamma}^x$, $h_{3,\delta}^x$, $h_{3,\delta}^y$ and $h_{3,\beta}^z$ for the thigh; with model N_3^h for $h_{2,\zeta}^x$, $h_{2,\eta}^x$ and $h_{2,\delta}^z$ for the shank, and $h_{3,\beta}^x$, $h_{3,\alpha}^y$, $h_{3,\beta}^y$, $h_{3,\alpha}^z$, $h_{3,\beta}^z$ and $h_{3,\delta}^z$ for the thigh. Note that the results were different depending on the subject. None of the models were able to represent accurately parameters \mathbf{h} , and none of S_3^h or N_3^h was better than the other.

2.6.3. Discussion

These preliminary results spotted numerical divergence problems for the MBO embedding models S_6^a , N_6^a and N_3^a which were hence discarded from the further quantitative study. This first step in the development led to the conclusion that the STA model built on the six rigid modes in all cases is not adapted to implementation in the proposed MBO method. The actual structure of the MBO, and particularly the form of the objective function was unable to well handle a large number of degrees of freedom (the number of design variables compared to the number of constraints or couplings). The problem was too much under-determined for a reliable estimation of both kinematics and STA parameters. Furthermore, the problem of under determinacy was also observed when using SBO, that is to say for models N_6^h and N_3^h . Thus, SBO was also inefficient in estimating simultaneously bones pose and STA model parameters since reducing the number of constraints equation increase the number of DoFs in the problem. Given this statement, decreasing the number of joint constraints while increasing the number of variables (for instance model N_6^h) constituted an inefficient approach. The systematic offset observed on the estimated \mathbf{h} parameters may be explained by the fact that the STA model was not calibrated. In the model originally proposed in Camomilla et al. (2015), the architecture of the STA entailed a linear combination of relevant joints, as in the present study, with a constant parameter determined under calibration procedure so that the estimated STA vector has a zero value when the subject assumes a reference posture. In our case, where only skin marker data was available, there was no calibration phase, the reference posture was approximated by the marker-cluster pose during the trial in the relevant segment coordinate system, but no constant correction term was embedded in the model. To be more specific, the initial STA vector was not set to zero which explained the shift on \mathbf{h} parameter estimates. As a consequence, the comparison of parameters \mathbf{h} did not provide relevant information for the discrimination of models S_3^h and N_3^h . MBO embedding joint constraints S_3^h or not N_3^h

seemed unable to reproduce parameters \mathbf{h} , while S_3^h provided acceptable amplitude estimate. Here was spotted the necessity of embedding joint constraints in MBO. Considering the above mentioned conclusions, the next part of the study will focus on the evaluation of the MBO embedding models S_3^h and S_3^a , a particular attention will be paid to the potential gain brought by the architecture of the amplitude in the STA model when introduced in MBO with spherical joints S_3^h when compared to the model S_3^a . We will no longer consider the capacity of the model to predict parameters \mathbf{h} , but the amplitude computed from equations (5.12) and (5.13).

2.7. Part 2: Evaluation of the selected models

The second part of the work presents the results of the optimization for the three trial of each subject S1, S2 and S3 considering the selected models S_3^h and S_3^a . A quantitative study was led on the mean values of joint kinematics and amplitude time histories, a basic statistic study was performed with the computation of RMSE and R^2 coefficient for a comparison of the estimates obtained with both models when embedded in MBO.

2.7.1. Objectives and procedure

The two models tested hereby were derived from two approaches of STA modeling. The objective here was to determine which model was better in estimating joint kinematics and STA model parameters. The first approach consisted in modeling the STA by a combination of three rotation modes and joints by spherical linkages S_3^h , initially proposed with six rigid modes in SBO (Camomilla et al., 2015), it has been shown in the previous qualitative part of this study that this version of the model did not suit well to the proposed MBO. The second model S_3^a embedded in MBO consisted in spherical joint models associated to the STA model approximating the amplitude of rotation modes as design variables of the optimization, this approach has been proposed with an affine approach instead of modal decomposition approach (Richard et al., 2012), but the implementation in MBO remains similar.

The models were evaluated by their ability to estimated accurate kinematics and amplitude of modes. The parameters \mathbf{h} could be compared between models since only model S_3^h provided these information. Furthermore, it has been mentioned in the previous part that the MBO was not able to estimate these parameters. A first section will present kinematics estimation for both models in regard to reference kinematics obtained from intracortical pins. The curves of the time histories of joint angles were analyzed through RMSE and R^2 . The same procedure was applied to the comparison of the amplitude of modes during the movement against the reference.

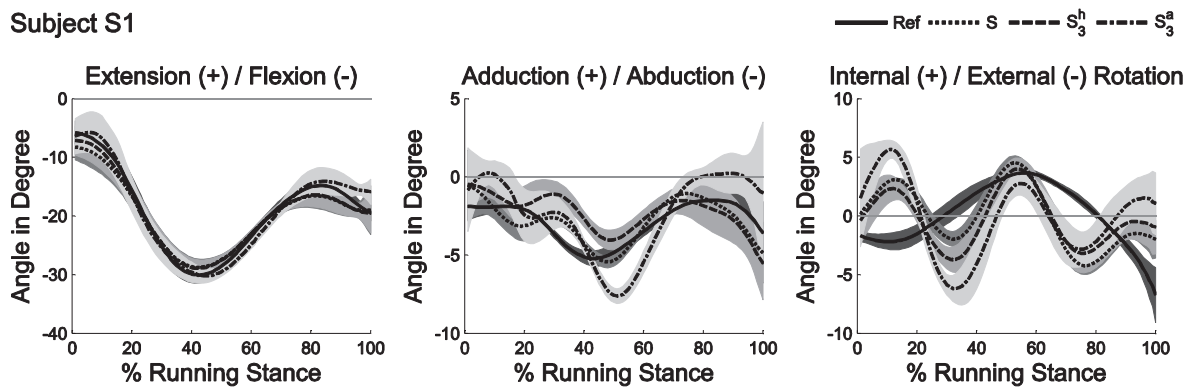
2.7.2. Results

Joint angles were represented in Figure 5.8 for MBO embedding models S , S_3^h and S_3^a and for reference kinematics obtained from intracortical pins, we also depicted RMSEs (Figure 5.9) and R^2 (Figure 5.10). Flexion was consistent with the reference for both model-derived estimations, even if little variations were observed in the initial and final values of the estimated angular kinematics. No systematic error was reported. The effectiveness of the models in estimating extension-flexion (EF) was comforted by RMSE similarly lower than 2° and correlation coefficient R^2 close to 1 for all models when compared to reference. Results were more mitigated for adduction-abduction (AA) and internal-external rotation (IER). While all models globally provided similar patterns (with different magnitudes), depending on the subject, these patterns were more or less close to the reference. Angular kinematics estimation obtained with model S_3^h was slightly closer than with model S_3^a to the estimation obtained with model S , which was the closest to the reference.

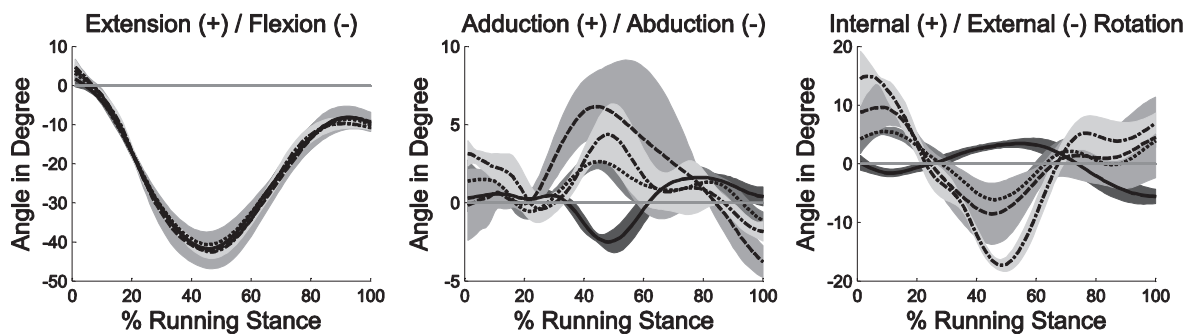
Except from EF angle, the spherical model (S) provided the lowest RMSE for all subjects. For subjects S1 and S2, model S_3^h provided lower RMSE than model S_3^a , for subject S2, model S_3^h presented higher RMSE on EF and AA than model S_3^a , but lower on IER. For all subjects and all models, the largest RMSE was observed for IER. Note that the RMSE for AA and IER for both model was in the same range as the magnitude of the actual angle. Except for EF, coefficients R^2 were globally low for all models, under 0.1 for IER for subjects S1 and S3, under 0.2 for AA for subject S2, about 0.3 for IER for subject S2, under 0.7 and 0.6 for subjects S1 and S3 respectively. The large discrepancy within different models and subjects did not show systematic difference preventing from determining if a model was closer to the reference than the other.

The amplitude $a_i^l(k)$ along each rotation mode (\mathbf{x} , \mathbf{y} and \mathbf{z}) were measured in mm. They were obtained for the three subjects estimating the shank and thigh STA using the models S_3^h and S_3^a and compared to the reference amplitude derived from intracortical pin data (Camomilla et al., 2015) (Figure 5.11). The time histories of the amplitude on the shank were globally far from the reference, irrespective of the model and the mode. In particular, for all subjects, we observed that the patterns of estimated amplitude of mode \mathbf{y} were the inverse relative to the reference, increasing when the reference decrease and vice-versa. Furthermore, while the magnitude of the amplitude obtained with model S_3^h was similar with the reference, the estimate obtained with model S_3^a provided significantly larger magnitude (more than twice). Focusing on the corridors appearing in Figure 5.11, we observed that subject S3 presented a large intra-subject variability while the estimated amplitudes showed little variability. For subjects S1 and S2, the variability amongst trials

Subject S1



Subject S2



Subject S3

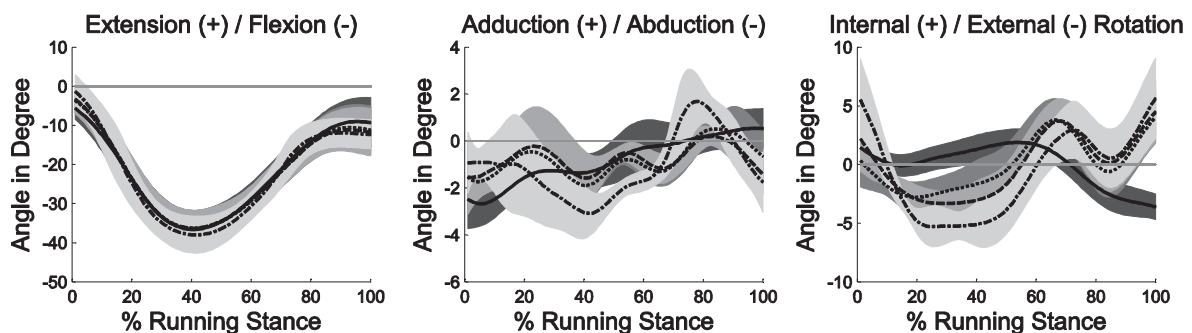


Figure 5.8 Knee joint angles for model S_3^h and S_3^a .

Plot resulting from MBO embedding model S_3^h and S_3^a against MBO embedding model S and reference kinematics. Plot of the mean and standard deviation over five trial of each of the three subjects S1 (top), S2 (middle) and S2 (bottom).

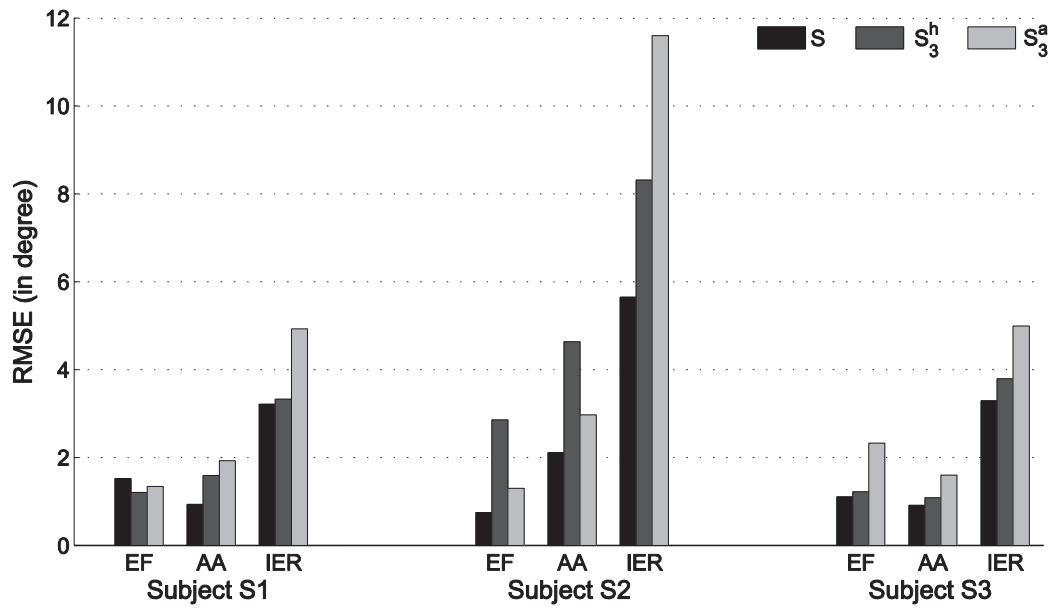


Figure 5.9 Root mean square errors (RMSE) for models S, S₃^h and S₃^a.

Plot resulting from the comparison of knee joint angles obtained from MBO embedding models S, S₃^h and S₃^a against reference kinematics. RMSE computed over five trial of each of the three subjects S1 (left), S2 (middle) and S2 (right). The three joint angles are EF: extension-flexion; AA: adduction-abduction; IER: internal-external rotation.

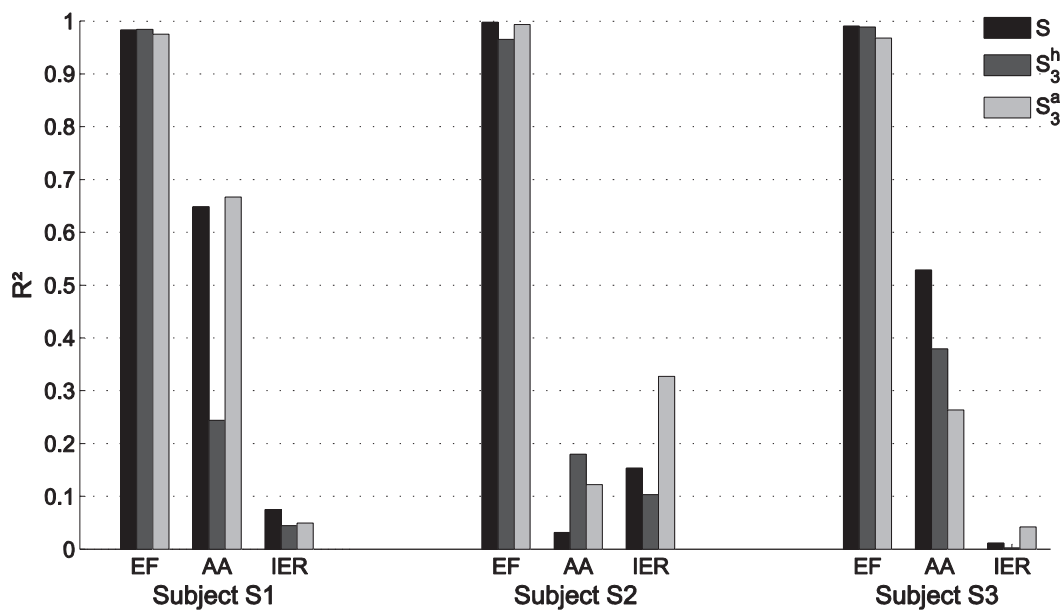


Figure 5.10 Correlation coefficient (R²) for models S, S₃^h and S₃^a.

Plot resulting from the comparison of knee joint angles obtained from MBO embedding models S, S₃^h and S₃^a against reference kinematics. RMSE computed over five trial of each of the three subjects S1 (left), S2 (middle) and S2 (right). The three joint angles are EF: extension-flexion; AA: adduction-abduction; IER: internal-external rotation.

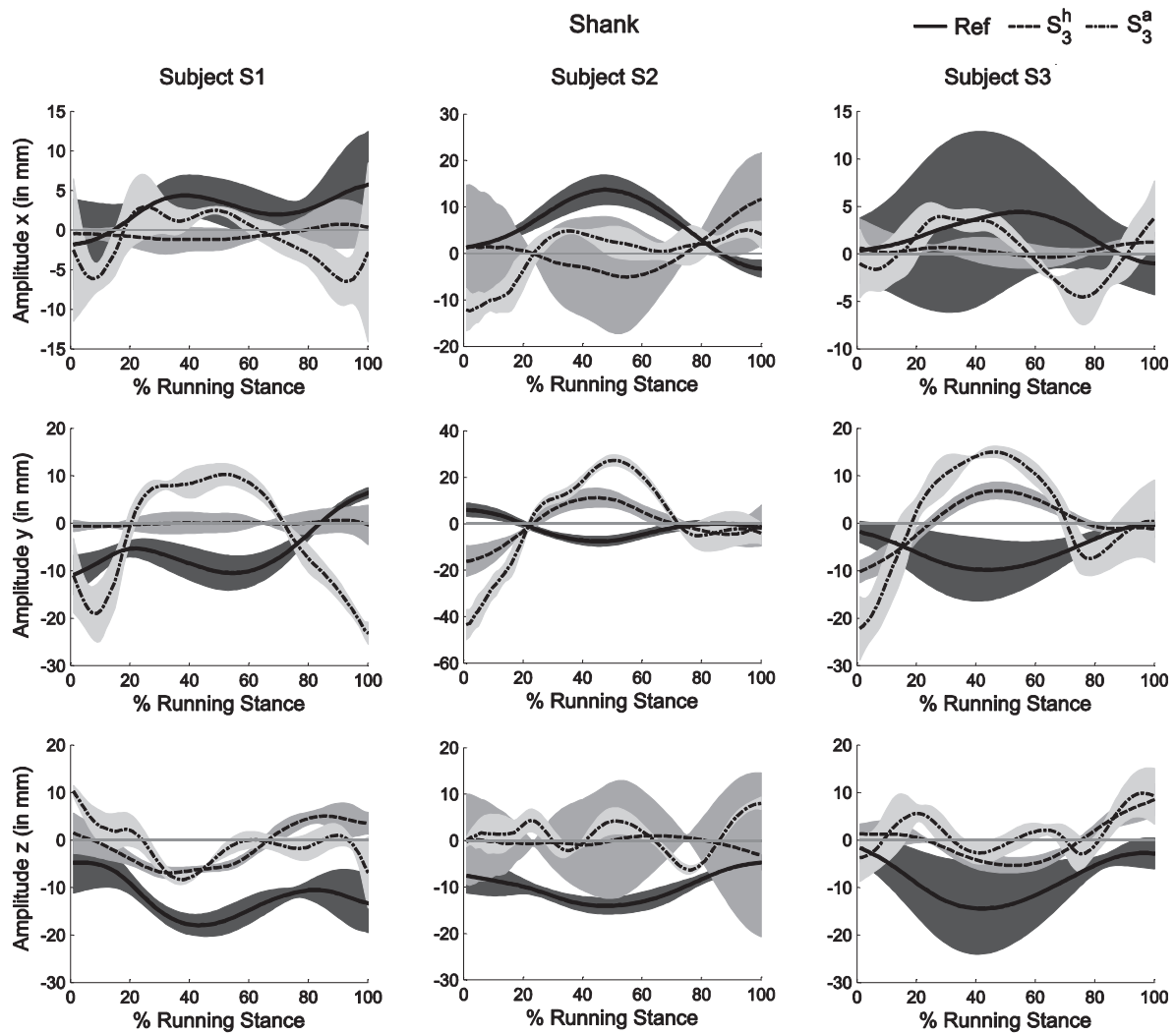


Figure 5.11 Amplitude estimate's time histories for models S_3^h and S_3^a .

Plot resulting from the shank with MBO embedding models S_3^h and S_3^a against reference mode amplitudes. Plot of the mean and standard deviation over five trial of each of the three subjects S1 (left), S2 (middle) and S2 (right).

of the same subject were low for reference as well as for model-derived estimate, except for subject S2 with model S_3^h . We can note that the model S_3^h provided more regular curves than model S_3^a which showed more inflection points and was waving around the curves obtained with model S_3^h .

For the thigh, results on amplitude patterns showed more similarities with the reference for both models than for the shank, even if globally the intra-subject variability was higher, in particular for mode y (Figure 5.12). Nevertheless, the patterns of amplitude for both models and the three

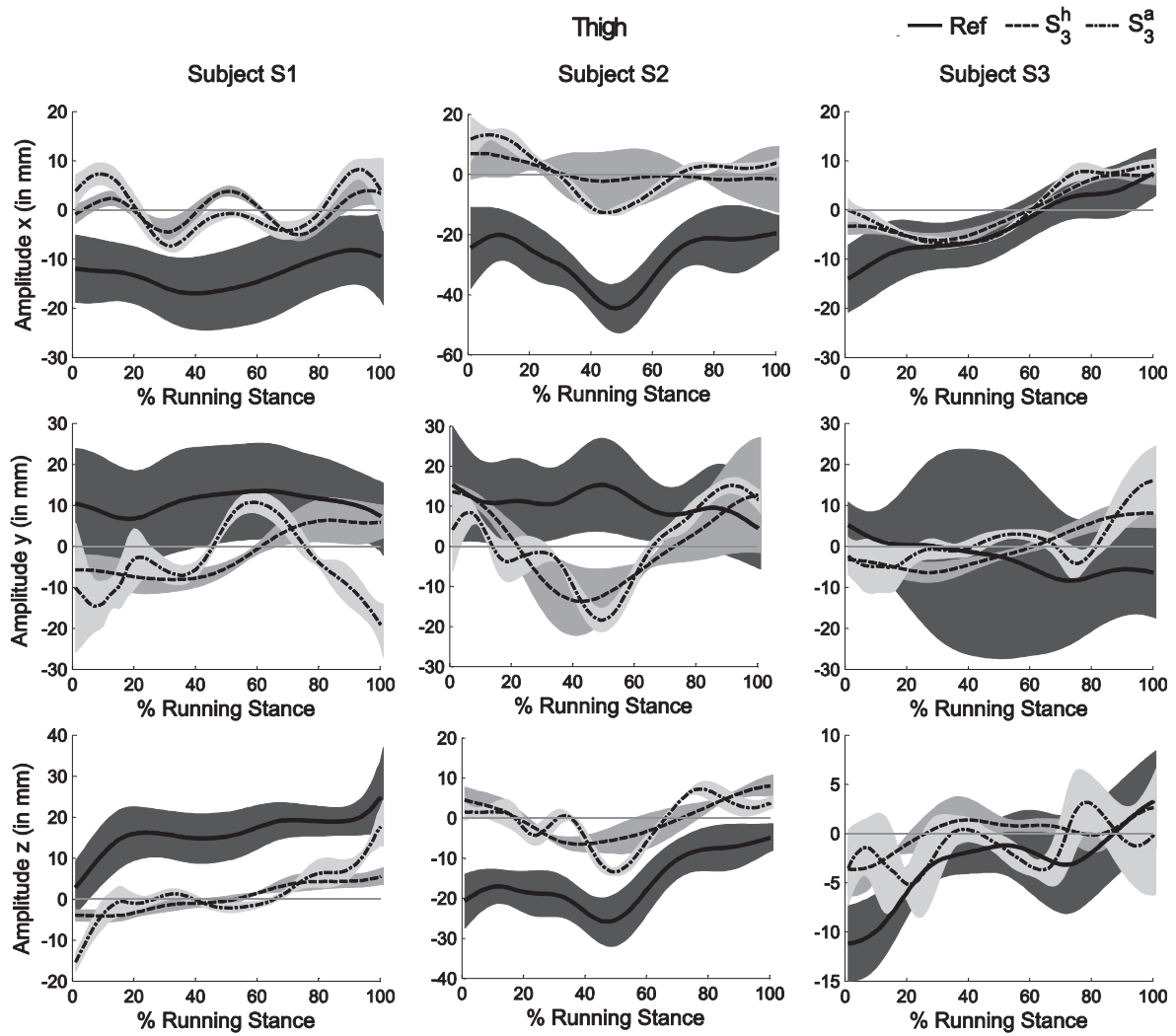


Figure 5.12 Amplitude estimate's time histories for models S_3^h and S_3^a .

Plot resulting from the thigh with MBO embedding models S_3^h and S_3^a against reference mode amplitudes. Plot of the mean and standard deviation over five trial of each of the three subjects S1 (left), S2 (middle) and S2 (right).

subjects were generally not contained in the range of variability of the reference amplitude, except for subject S3 on mode x which was close to the reference and for subject S3 on mode y where the intra-subject variability of the reference was large (about 50 mm). The couplings of amplitudes with angular kinematics did not appear clearly on the results with the model S_3^h . The amplitudes were generally shifted with an offset depending on the subject, mode and model considered. For example, the reference amplitude for modes x of subject S1 and S2 and mode z for subject 2 were strictly negative during the movement while the estimates obtained from models S_3^h and S_3^a oscillated between positive and negative values.

With RMSE of the amplitude for the thigh ranging between 5mm and 23mm (Figure 5.13), the amplitude for the shank was closer to the reference than for the thigh, with a range of RMSE

between 5mm and more than 32mm. RMSE showed more discrepancy amongst models S_3^h and S_3^a for the shank than for the thigh, for which RMSE on each mode was similar with both models. For the shank, RMSE were larger on modes x and z with model S_3^a than with S_3^h . For subject S2, smaller RMSE were observed on modes x and mode z with model S_3^a and larger RMSE on y . The overall RMSE were slightly smaller for model S_3^h than for model S_3^a .

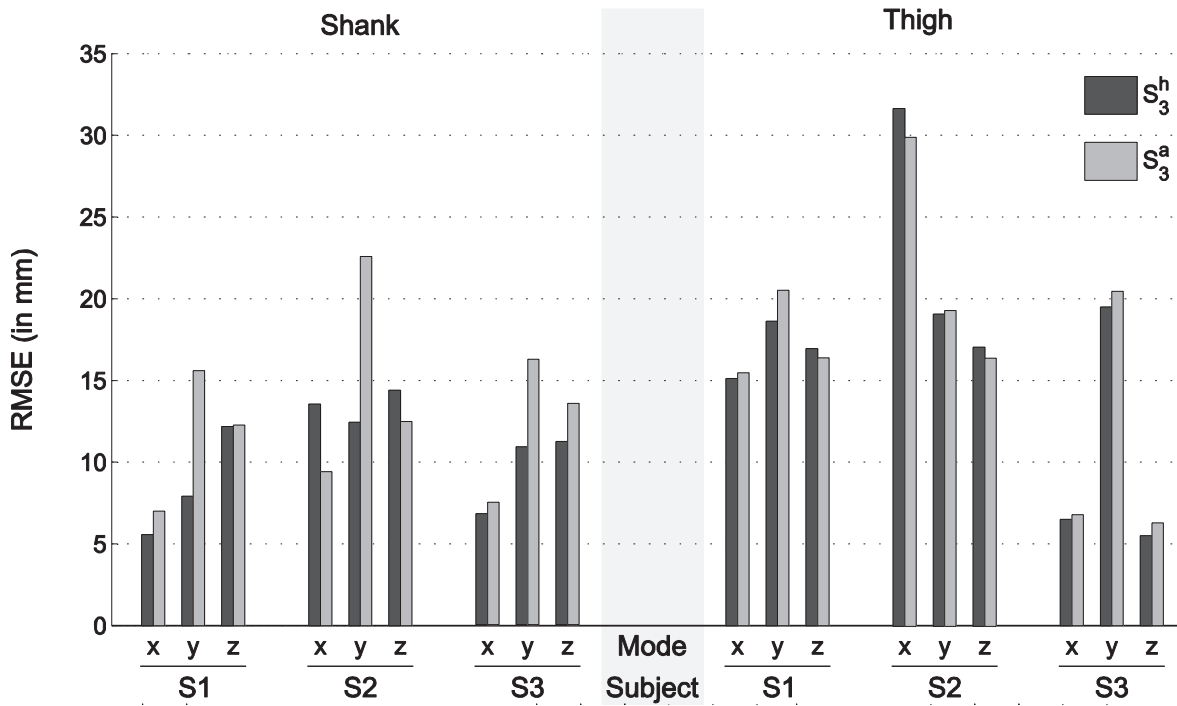


Figure 5.13 Root mean square errors (RMSE) for S_3^h and S_3^a .

Plot resulting from the comparison of amplitude of modes estimation obtained from MBO embedding models S_3^h and S_3^a against reference amplitude of modes. RMSE computed over five trial of each of the three subjects S1 (left), S2 (middle) and S2 (right). The three rotation modes are designated by x , y and z .

Correlation coefficients R^2 of the amplitudes were really low (Figure 5.14), under 0.5 for all subjects on all modes with all models, except for mode y of subject S2 for the shank which presented coefficients R^2 between 0.6 and 0.7 for both models. We observed in particular coefficients R^2 under 0.1 for the shank for subject S1 on mode x with both models, for subject S2 on modes x and z , for subject S3 on mode x and z with both models; for the thigh for subject S1 on modes x and y with both models, for subject S2 on mode x with model S_3^a and y with both models, and for subject S3 on mode y with both models and z with model S_3^a .

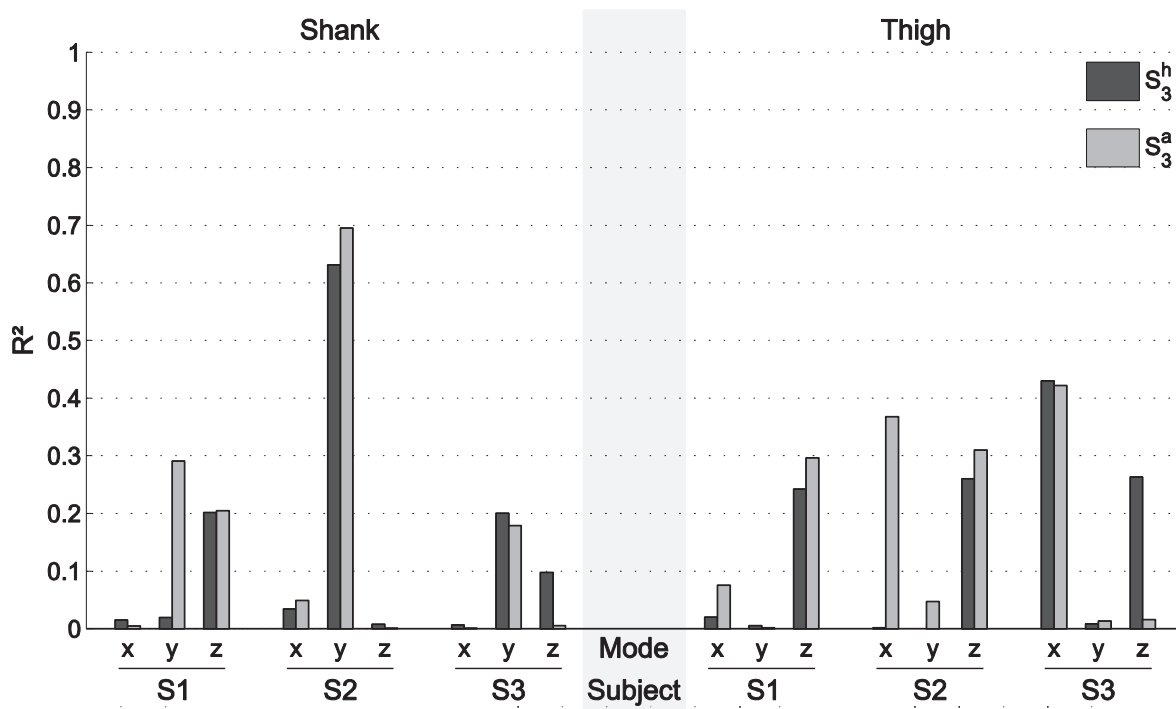


Figure 5.14 Correlation coefficient (R^2) for models S_3^h and S_3^a .

Plot resulting from the comparison of the estimation of STA amplitudes obtained from MBO embedding models S_3^h and S_3^a against reference STA amplitudes. RMSE computed over five trials of each of the three subjects S1, S2 and S3.

The computation time of the MBO embedding model S_3^h for one trial was about 7 minutes while it represented about 1.6 seconds with model S_3^a for a dataset composed of about 100 frames.

2.7.3. Intermediate discussion

The reference angular kinematics and STA model parameters were derived from intracortical pin data. MBO was performed embedding models S_3^h and S_3^a , then compared to the reference. Two aspects of the optimization process were compared. Concerning the angular kinematics, the MBO embedding S_3^h or S_3^a was not able to provide better accuracy than spherical model (S). For subjects S1 and S2, joint angles estimated with model S_3^a were slightly better than with model S_3^h , the opposite tendency was observed for subject S2. Globally, the results were not satisfying. The comparison of STA parameters estimation with models S_3^h and S_3^a were shown to be as mitigatory as for kinematics. We also noted that the variability of the kinematics amongst different trials of a same subject were larger when estimated (with models S_3^h or S_3^a) than for the reference. At the opposite, variability of amplitudes within the five trials of each subject was smaller when modeled than for the reference. Concerning the estimation of the amplitude of STA models, the conclusion was mitigatory, as for kinematics. Model S_3^a seemed to be less inaccurate than model S_3^h for

subjects S1 and S2, and more inaccurate for subject S3. The computation time was therefore an important criterion for the practicability of such a method, in this matter, model S_3^a present a considerable advantage over model S_3^h .

3. Discussion and conclusion

As proposed in the study, no significant difference of efficiency was find between models S_3^h and S_3^a when embedded in MBO. Both models were unable to provide accurate kinematics nor STA amplitude (and less yet \mathbf{h} parameters). In particular, the proposed MBO methods embedding STA models did not provide improvement in estimation of kinematics in comparison to more classic MBO (with models S and N) and the STA amplitude obtained from these models were not satisfying. Even if results showed relatively bad efficiency, the matter in hand presents some promising points deserving particular attention.

As a first point, and not the least, the study showed MBO was proficient in estimating bone pose in the same time as STA model parameters. Indeed, the low variability of the estimated kinematics and amplitudes revealed that the optimization process actually found the minimum of the objective function. In other words, the problem has a unique solution, independent to the initial guess. This statement lead to the main criticism to oppose to the MBO as presented in the study, the objective function was not adapted to the problem.

Attention has also been drawn to the crucial matter of under determinacy of the mathematical formulation, the design of the optimization manages the balance between output parameters (design variables) and constraints (or couplings). An important effort has been made on the reduction of the number of STA model parameters using modal decomposition (Dumas et al., 2014), and further reducing the number of parameters seems difficult, efforts must now be concentrated on the design of the MBO. We have seen that the qualitative efficiency of the models is affected by the degree of the under determinacy of the optimization. For instance, models based on six modes were discarded for providing unacceptable estimates, and associated to SBO (no joint constraints) they prevented the convergence of the optimization. Few solutions may be investigated: the development and implementation of more physiological joint models; the addition of constraints on STA like boundaries derived from *a priori* knowledge on the range of amplitude for example, prescribed signs of the \mathbf{h} parameters (but ranges and signs were found subject-specific); or, it goes back to the design of a more appropriate objective function that would better suit to the management of the two sets of parameters. A possibility would be to perform a multi-objective optimization (Marler and Arora, 2004).

A major issue with model S_3^h and other models embedding the joint angle-dependent architecture is that the amplitude of modes was a linear combination of joint angles kinematics, which was in our case the initial solution derived from the skin markers (subject to artefact) and not from the actual bone pose. The second solution would be to use the kinematics derived from the concurrent optimization. The bias introduced by the difference between initial solution and the actual bone pose was jeopardized by the optimization and influenced kinematics estimation as well as STA model parameters estimation. Preliminary tests using an updated joint kinematics showed that the convergence can be very problematic.

Further work may also take into account the computation time which was dramatically longer for the models embedding STA amplitude architecture. The number of parameters must be reduced to the minimum while the optimization method is crucial as well. In fact, the model considering amplitudes as design variables (S_3^a) was introduced in a frame-by-frame Gauss-Newton algorithm where analytical Jacobians are provided. For the model S_3^h considering a specific architecture of the amplitude of STA, the introduction of parameters \mathbf{h} constant in time in the optimization considering time histories of bone pose parameters involved a major modification of the method. The approach consisted in a two-level optimization considering time dependent parameters in a frame-by-frame Gauss-Newton algorithm, the results of this inner loop were the inputs for the outer loop considering the constant in time \mathbf{h} parameters. That is to say, the inner loop was computed as many times as the number of iterations of the outer loop. A possible solution for this problem would be to concatenate the time dependent parameters (Andersen et al., 2010a) in a single vector, the number of parameters at each iteration would be equal to the number of bone pose parameters times the number of sampled instant of time plus the number of constant in time parameters \mathbf{h} instead of a frame-by-frame approach.

It seems important to note that the standard deviation of the estimation obtained for STA amplitude with models S_3^h and S_3^a was significantly small when compared to the actual STA variability within different trials of the same subject. This characteristics reveal a high precision of the model and the MBO method in general to estimate STA amplitude. One must recall that the accuracy is generally associated with systematic errors while precision with random errors. According to this definition, the method succeeded in reducing random error (low variability), while it failed in compensating the systematic error. However, accuracy is often improved by the fine adaptation of models through calibration, for example. The addition, customization or personalization of constraints to the MBO may also be a part of the solution to the accuracy issue. It is reasonable to envisage a customization of the objective function and constraints that would

provide better accuracy. Combined with the good precision, a well-designed optimization may provide good trueness and efficient estimator, both for bone pose and STA parameters.

Finally, the different results and observation may appear unsatisfactory but many aspects of the results present real interest and widen the perspective of such a method. Actually, this study allow us to envisage STA compensation in an original manner, since the feasibility of implementing a complex model in MBO, considering joint constraints as well as STA features. Given the versatility of the mathematical formulation of the STA model and its ability to be adapted at will, further pieces of work must be supplied on the best way to conciliate design variables apparently uncorrelated (bone pose and STA model parameters) with suited objective function and constraints. This point in particular has been partially investigated with the use of the architecture of the amplitude model ([Camomilla et al., 2015](#)). Even with mitigatory results, this approach proposing couplings between supposedly unpredictable STA and relevant joint angle kinematics showed some promising outcomes.

Chapter 6. General discussion

In the thesis, three approaches of the MBO method were developed, based on an existing mathematical formulation of the MBO method (Duprey et al., 2010) using natural coordinates (Dumas and Chèze, 2007; Garcia De Jalon et al., 1994). The evaluation of the methods essentially consisted in feasibility studies and the objectives were to explore the capacity of the MBO method to provide satisfying estimates of bone pose and joint kinematics using original methods (i.e., tracking MIMUs data, on-line calibration of STA model) and models (elastic joint based on knee stiffness matrix, kinematic-driven STA model). The general framework compatible with all different approaches was developed for computational and numerical evaluation. The objective was to propose new approaches likely to overcome questionable critics generally formulated for movement analysis using model-based bone pose estimators (Andersen et al., 2009; Clément et al., 2014; Li et al., 2012; Stagni et al., 2009). A significant evolution of the MBO method explored in the thesis lies in the feasibility of considering angular velocity and acceleration to drive the kinematic model. It is therefore possible to track either trajectories using stereophotogrammetry and skin markers or MIMUs data to reconstruct joint kinematics through the MBO methods. The MBO method may be used for *in-situ* and ambulatory analysis. Moreover, the possibility to track angular velocity and acceleration suggest that the method can be used even in perturbed magnetic field environment. Another aspect, is discussed in the second study concerning the definition of the joint models. The accuracy of joint kinematics estimated using skin-marker trajectories and the MBO method relies on the biofidelity of the joint model and is still open to debate. The use of “hard” constraints may engender pernicious errors in the estimates. Typically, very limited inter-subject variability is obtained. But the most critical errors in joint angles and displacements estimates using surface measurement consist in the incapacity of the methods to compensate for the STA efficiently. This issue aggregates most of the efforts in the community. Implementing a model of STA in the MBO method represents a challenge which could bring a significant contribution in skeletal movement estimation. All these statement were the source of the studies carried out in the thesis, giving rise to three contributions.

The first approach, extends the MBO framework to the use of MIMUs, including not only orientations (Koning et al., 2015), but also angular velocities and accelerations as drivers of the kinematic model. The study confirmed the feasibility of tracking the orientations in the objective function, as well as, more originally, angular velocity. The study also confirmed the relevance of the anatomical calibration (Picerno et al., 2008) of the MIMU orientation within the MBO framework. While promising, the introduction of linear acceleration has to be further analyzed. In

particular, the use of the linear acceleration in the proposed MBO method supposes to have reliable information about position, which is not provided by the MIMUs. Methods have been proposed very recently to anatomically calibrate the MIMUs position using one off-the-shelf camera (Bisi et al., 2015). Furthermore, the raw output signals are subject to errors (i.e., drift). The main issue remain the lack of the positions of the sensors, which prevent from bone pose estimation in a global reference coordinate system. Further improvement could be expected in developing additional positioning technics.

The second method considers a new knee joint model for the MBO method, whose behavior is described by a stiffness matrix (Lamberto et al., 2016) using a penalty-based method. The implementation of “soft” constraints represents a promising improvement for joint models (Bolsterlee et al., 2014; Charbonnier et al., 2014; Gasparutto et al., 2015). It is less cumbersome than personalization (considered as mandatory when “hard” constraints are to be used), which generally involves medical imaging. Although numerous studies are attached to the personalization of geometric joint models (Clément et al., 2014; Scheys et al., 2011; Valente et al., 2015), it seems also important to consider the adaptation of the computation methods. Constrained optimization methods relies on two sets of equations: “hard” constraints that are strictly respected, “soft” constraints that are minimized (appended to the objective function). By defining joint constraints as “soft” constraints, the deterministic property of the kinematic models can be overcome. The deformation energy, computed from the stiffness matrix, joint angles and displacements, is minimized, together with the tracking errors of the skin markers. The method can be extended to other joints at the condition that the joint mechanical behavior is described by a stiffness matrix, as well as to pathological joints for which classical models (spherical joint, hinge joint) are inappropriate.

The third MBO approach challenges straightforwardly the STA issue (Cappozzo et al., 1996; Leardini et al., 2005) aiming at estimating optimal bone pose by compensating for STA using a kinematic-driven STA model (Bonci et al., 2014; Camomilla et al., 2013). The idea is to concurrently estimate the instantaneous bone pose from skin markers and the amplitude of the STA rigid component (i.e., rotation and translation of the marker-cluster). The large number of parameters involved in the STA model could be deleterious for the convergence of the method. Although the number of parameters has been reduced in the kinematic-driven STA model (Camomilla et al., 2015; Dumas et al., 2014), the under-determinacy of the optimization problem highlighted the importance of choosing adequate criteria (alternative objective function, additional constraints).

Indeed, the minimization of the least square errors between measured and modeled markers, as used in the tested MBO approach, was not found an appropriate criteria, even if a good convergence of the algorithm and a small tracking errors of the markers can be obtained.

To conclude the MBO method was shown to be a versatile model-based approach for joint kinematics and bone pose estimation. Previous studies demonstrated that the method was able to manage various “hard” constraints (Duprey et al., 2010), and “soft” constraints (Gasparutto et al., 2015), but also MIMU-derived objective functions (Koning et al., 2015). The present study goes a step further in the development of the MBO method in proposing alternatives to existing kinematic or driving constraints. Elastic joint models may represent the most accomplished contribution of this work. It is important to note that the work was mainly exploratory and that the methods proposed in the present thesis are still requiring further developments, at this time, the results stands for proof of concept and feasibility studies and prevent from a widespread use, in particular for clinical applications. In proposing versatile methods and models, potentially adaptable to different situations, the scope for the use of the MBO method is getting larger. The real advantage of the general framework of the MBO method lies in the possibility to implement easily any kind of classic joint models, elastic joint models and various objective functions. The possibilities are various, and are adapted to most of the studies.

References

- Ackland, D.C., Keynejad, F., Pandy, M.G., 2011. Future trends in the use of X-ray fluoroscopy for the measurement and modelling of joint motion. *Proc. Inst. Mech. Eng. Part H J. Eng. Med.* 225, 1136–1148.
- Ahmadi, A., Rowlands, D.D., James, D.A., 2006. Investigating the translational and rotational motion of the swing using accelerometers for athlete skill assessment. *Proc. IEEE Sensors* 980–983.
- Akbarshahi, M., Schache, A.G., Fernandez, J.W., Baker, R., Banks, S., Pandy, M.G., 2010. Non-invasive assessment of soft-tissue artifact and its effect on knee joint kinematics during functional activity. *J. Biomech.* 43, 1292–1301.
- Alexander, E.J., Andriacchi, T.P., 2001. Correcting for deformation in skin-based marker systems. *J. Biomech.* 34, 355–361.
- Altun, K., Barshan, B., Tunçel, O., 2010. Comparative study on classifying human activities with miniature inertial and magnetic sensors. *Pattern Recognit.* 43, 3605–3620.
- Andersen, M.S., Benoit, D.L., Damsgaard, M., Ramsey, D.K., Rasmussen, J., 2010a. Do kinematic models reduce the effects of soft tissue artefacts in skin marker-based motion analysis? An in vivo study of knee kinematics. *J. Biomech.* 43, 268–273.
- Andersen, M.S., Damsgaard, M., MacWilliams, B., Rasmussen, J., 2010b. A computationally efficient optimisation-based method for parameter identification of kinematically determinate and over-determinate biomechanical systems. *Comput. Methods Biomech. Biomed. Engin.* 13, 171–183.
- Andersen, M.S., Damsgaard, M., Rasmussen, J., 2009. Kinematic analysis of over-determinate biomechanical systems. *Comput. Methods Biomech. Biomed. Engin.* 12, 371–384.
- Andersen, M.S., Damsgaard, M., Rasmussen, J., Ramsey, D.K., Benoit, D.L., 2012. A linear soft tissue artefact model for human movement analysis: Proof of concept using in vivo data. *Gait Posture* 35, 606–611.
- Andriacchi, T.P., Alexander, E.J., 2000. Studies of human locomotion: Past, present and future. *J. Biomech.* 33, 1217–1224.
- Andriacchi, T.P., Alexander, E.J., Toney, M.K., Dyrby, C., Sum, J., 1998. A point cluster method for in vivo motion analysis: applied to a study of knee kinematics. *J Biomech Eng* 120, 743–749.
- Ausejo, S., Suescun, Á., Celigüeta, J., 2011. An optimization method for overdetermined kinematic problems formulated with natural coordinates. *Multibody Syst. Dyn.* 26, 397–410.
- Baker, R., 2007. The history of gait analysis before the advent of modern computers. *Gait Posture* 26, 331–342.
- Baldisserri, B., Parenti-Castelli, V., 2012. A New 3D Mechanism for Modeling the Passive Motion of the Tibia–Fibula–Ankle Complex. *J. Mech. Robot.* 4, 021004.
- Ball, K.A.K., Pierrynowski, M.R.M., 1998. Modeling of the pliant surfaces of the thigh and leg during gait. *Proc. SPIE- BiOS'98 Int. Biomed. Opt. Symp.* 3254, 435–446.
- Barré, A., Thiran, J.P., Jolles, B.M., Theumann, N., Aminian, K., 2013. Soft tissue artifact assessment during treadmill walking in subjects with total knee arthroplasty. *IEEE Trans. Biomed. Eng.* 60, 3131–3140.
- Benoit, D.L., Damsgaard, M., Andersen, M.S., 2015. Surface marker cluster translation, rotation,

- scaling and deformation: Their contribution to soft tissue artefact and impact on knee joint kinematics. *J. Biomech.* 48, 2124–2129.
- Benoit, D.L., Ramsey, D.K., Lamontagne, M., Xu, L., Wretenberg, P., Renstr m, P., 2006. Effect of skin movement artifact on knee kinematics during gait and cutting motions measured in vivo. *Gait Posture* 24, 152–164.
- Bergamini, E., Pillet, H., Hausselle, J., Thoreux, P., Guerard, S., Camomilla, V., Cappozzo, A., Skalli, W., 2011. Tibio-femoral joint constraints for bone pose estimation during movement using multi-body optimization. *Gait Posture* 33, 706–711.
- Bisi, M.C., Stagni, R., Caroselli, A., Cappello, A., 2015. Anatomical calibration for wearable motion capture systems: Video calibrated anatomical system technique. *Med. Eng. Phys.* 37, 813–9.
- Bland, J., Altman, D.G., 1986. Statistical Methods for Assessing Agreement Between Two Methods of Clinical Measurement. *Lancet* 327, 307–310.
- Bolsterlee, B., Veeger, H.E.J., van der Helm, F.C.T., 2014. Modelling clavicular and scapular kinematics: From measurement to simulation. *Med. Biol. Eng. Comput.* 52, 283–291.
- Bonci, T., Camomilla, V., Dumas, R., Ch ze, L., Cappozzo, A., 2014. A soft tissue artefact model driven by proximal and distal joint kinematics. *J. Biomech.* 47, 2354–2361.
- Bonci, T., Camomilla, V., Dumas, R., Ch ze, L., Cappozzo, A., 2015. Rigid and non-rigid geometrical transformations of a marker-cluster and their impact on bone-pose estimation. *J. Biomech.* 48, 4166–4172.
- Borelli, G.A., 1653. *De motu animalium*. Angeli Bernabo, Rome.
- Braune, W., 1987. *The human gait*. Springer-Verlag Berlin Heidelberg.
- Camomilla, V., Bonci, T., Dumas, R., Ch ze, L., Cappozzo, A., 2015. A model of the soft tissue artefact rigid component. *J. Biomech.* 48, 1752–1759.
- Camomilla, V., Cereatti, A., Ch ze, L., Cappozzo, A., 2013. A hip joint kinematics driven model for the generation of realistic thigh soft tissue artefacts. *J. Biomech.* 46, 625–630.
- Camomilla, V., Donati, M., Stagni, R., Cappozzo, A., 2009. Non-invasive assessment of superficial soft tissue local displacements during movement: A feasibility study. *J. Biomech.* 42, 931–937.
- Caplan, N., Kader, D.F., 2014. Stiffness and laxity of the knee: The contributions of the supporting structures: A quantitative in vitro study. *Class. Pap. Orthop.* 58, 137–139.
- Cappello, A., Cappozzo, A., La Palombara, P.F., Lucchetti, L., Leardini, A., 1997. Multiple anatomical landmark calibration for optimal bone pose estimation. *Hum. Mov. Sci.* 16, 259–274.
- Cappello, A., Stagni, R., Fantozzi, S., Leardini, A., 2005. Soft tissue artifact compensation in knee kinematics by double anatomical landmark calibration: Performance of a novel method during selected motor tasks. *IEEE Trans. Biomed. Eng.* 52, 992–998.
- Cappozzo, a, Catani, F., Della Croce, U., Leardini, a, 1995. Position and orietnation in space of bones during movement. *Clin. Biomech.* 10, 171–178.
- Cappozzo, A., Catani, F., Leardini, A., Benedetti, M.G., Della Croce, U., 1996. Position and orientation in space of bones during movement: Experimental artefacts. *Clin. Biomech.* 11, 90–100.
- Cappozzo, A., Della Croce, U., Leardini, A., Chiari, L., 2005. Human movement analysis using stereophotogrammetry. Part 1: Theoretical background. *Gait Posture* 21, 186–196.
- Cereatti, A., Margheritini, F., Donati, M., Cappozzo, A., 2010. Is the human acetabulofemoral joint spherical? *J. Bone Joint Surg. Br.* 92, 311–314.

- Challis, J.H., 1995. An examination of procedures for determining body segment attitude and position from noisy biomechanical data. *Med. Eng. Phys.* 17, 83–90.
- Chan, Y.Y., Fong, D.T.P., Chung, M.M.L., Li, W.J., Liao, W.H., Yung, P.S.H., Chan, K.M., 2010. Identification of ankle sprain motion from common sporting activities by dorsal foot kinematics data. *J. Biomech.* 43, 1965–1969.
- Charbonnier, C., Chagué, S., Kolo, F.C., Chow, J.C.K., Lädermann, A., 2014. A patient-specific measurement technique to model shoulder joint kinematics. *Orthop. Traumatol. Surg. Res.* 100, 715–719.
- Chardonens, J., Favre, J., Cuendet, F., Gremion, G., Aminian, K., 2013. A system to measure the kinematics during the entire ski jump sequence using inertial sensors. *J. Biomech.* 46, 56–62.
- Charlton, I.W., Tate, P., Smyth, P., Roren, L., 2004. Repeatability of an optimised lower body model. *Gait Posture* 20, 213–221.
- Chèze, L., Fregly, B.J., Dimnet, J., 1995. A solidification procedure to facilitate kinematic analyses based on video system data. *J. Biomech.* 28, 879–884.
- Chiari, L., Della Croce, U., Leardini, A., Cappozzo, A., 2005. Human movement analysis using stereophotogrammetry. Part 2: Instrumental errors. *Gait Posture* 21, 197–211.
- Clark, R.A., Bartold, S., Bryant, A.L., 2010. Tibial acceleration variability during consecutive gait cycles is influenced by the menstrual cycle. *Clin. Biomech.* 25, 557–562.
- Clément, J., Dumas, R., Hagemeister, N., de Guise, J.A., 2015. Soft tissue artifact compensation in knee kinematics by multi-body optimization: Performance of subject-specific knee joint models. *J. Biomech.* 48, 3796–3802.
- Clément, J., Hagemeister, N., Dumas, R., Kanhou, M., de Guise, J.A., 2014. Influence of biomechanical multi-joint models used in global optimisation to estimate healthy and osteoarthritis knee kinematics. *Comput. Methods Biomech. Biomed. Engin.* 17 Suppl 1, 76–7.
- Coley, B., Najafi, B., Paraschiv-Ionescu, A., Aminian, K., 2005. Stair climbing detection during daily physical activity using a miniature gyroscope. *Gait Posture* 22, 287–94.
- Cooper, G., Sheret, I., McMillan, L., Siliverdis, K., Sha, N., Hodgins, D., Kenney, L., Howard, D., 2009. Inertial sensor-based knee flexion/extension angle estimation. *J. Biomech.* 42, 2678–2685.
- Cutti, A.G., Ferrari, A., Garofalo, P., Raggi, M., Cappello, A., Ferrari, A., 2010. “Outwalk”: A protocol for clinical gait analysis based on inertial and magnetic sensors. *Med. Biol. Eng. Comput.* 48, 17–25.
- De Rosario, H., Page, A., Besa, A., Mata, V., Conejero, E., 2012. Kinematic description of soft tissue artifacts: Quantifying rigid versus deformation components and their relation with bone motion. *Med. Biol. Eng. Comput.* 50, 1173–1181.
- De Rosario, H., Page, Á., Besa, A., Valera, Á., 2013. Propagation of soft tissue artifacts to the center of rotation: A model for the correction of functional calibration techniques. *J. Biomech.* 46, 2619–2625.
- Dejnabadi, H., Jolles, B.M., Aminian, K., 2005. A new approach to accurate measurement of uniaxial joint angles based on a combination of accelerometers and gyroscopes. *IEEE Trans. Biomed. Eng.* 52, 1478–1484.
- Desroches, G., 2010. Expression of Joint Moment in the Joint Coordinate System. *J. Biomech. Eng.* 132, 114503.
- Dettwyler, M., Stacoff, A., Kramers-De Quervain, I.A., Stüssi, E., 2004. Modelling of the ankle

- joint complex. Reflections with regards to ankle prostheses. *Foot Ankle Surg.* 10, 109–119.
- Di Gregorio, R., Parenti-Castelli, V., O'Connor, J.J., Leardini, A., 2007. Mathematical models of passive motion at the human ankle joint by equivalent spatial parallel mechanisms. *Med. Biol. Eng. Comput.* 45, 305–313.
- Dubousset, J., 1994. *Three-Dimensional Analysis of the Scoliotic Deformity. The pediatric spine: principles and practice.* Raven Press Ltd., New York, pp. 479–496.
- Dumas, R., Camomilla, V., Bonci, T., Chèze, L., Cappozzo, A., 2014. Generalized mathematical representation of the soft tissue artefact. *J. Biomech.* 47, 476–481.
- Dumas, R., Camomilla, V., Bonci, T., Chèze, L., Cappozzo, A., 2015. What portion of the soft tissue artefact requires compensation when estimating joint kinematics? *J. Biomech. Eng.* 4, 64502.
- Dumas, R., Chèze, L., 2007. 3D inverse dynamics in non-orthonormal segment coordinate system. *Med. Biol. Eng. Comput.* 45, 315–322.
- Dumas, R., Chèze, L., 2009. Soft tissue artifact compensation by linear 3D interpolation and approximation methods. *J. Biomech.* 42, 2214–2217.
- Dumas, R., Chèze, L., Verriest, J.P., 2007. Adjustments to McConville et al. and Young et al. body segment inertial parameters. *J. Biomech.* 40, 543–553.
- Dumas, R., Lafon, Y., Jacquelin, E., Chèze, L., 2009. Soft tissue artefacts: compensation and modelling. *Comput. Methods Biomech. Biomed. Engin.* 12, 103–104.
- Dumas, R., Moissenet, F., Gasparutto, X., Chèze, L., 2012a. Influence of joint models on lower-limb musculo-tendon forces and three-dimensional joint reaction forces during gait. *Proc. Inst. Mech. Eng. Part H J. Eng. Med.* 226, 146–160.
- Dumas, R., Robert, T., Pomeroy, V., Chèze, L., 2012b. Joint and segment coordinate systems revisited. *Comput. Methods Biomech. Biomed. Engin.* 15, 183–185.
- Duprey, S., Chèze, L., Dumas, R., 2009. A constraint-based approach to model the lower limb: preliminary results for running motions. *Comput. Methods Biomech. Biomed. Engin.* 12, 105–106.
- Duprey, S., Chèze, L., Dumas, R., 2010. Influence of joint constraints on lower limb kinematics estimation from skin markers using global optimization. *J. Biomech.* 43, 2858–2862.
- Ehrig, R.M., Taylor, W.R., Duda, G.N., Heller, M.O., 2006. A survey of formal methods for determining the centre of rotation of ball joints. *J. Biomech.* 39, 2798–2809.
- El Habachi, A., Moissenet, F., Duprey, S., Chèze, L., Dumas, R., 2015. Global sensitivity analysis of the joint kinematics during gait to the parameters of a lower limb multi-body model. *Med. Biol. Eng. Comput.* 53, 655–667.
- Faber, G.S., Chang, C.C., Kingma, I., Dennerlein, J.T., Dieën, J.H. Van, 2016. Estimating 3D L5 / S1 moments and ground reaction forces during trunk bending using a full-body ambulatory inertial motion capture system. *J. Biomech.* 49, 904–912.
- Favre, J., Jolles, B.M., Aissaoui, R., Aminian, K., 2008. Ambulatory measurement of 3D knee joint angle. *J. Biomech.* 41, 1029–1035.
- Favre, J., Luthi, F., Jolles, B.M., Siegrist, O., Najafi, B., Aminian, K., 2006. A new ambulatory system for comparative evaluation of the three-dimensional knee kinematics, applied to anterior cruciate ligament injuries. *Knee Surgery, Sport. Traumatol. Arthrosc.* 14, 592–604.
- Findlow, A., Goulermas, J.Y., Nester, C., Howard, D., Kenney, L.P.J., 2008. Predicting lower limb joint kinematics using wearable motion sensors. *Gait Posture* 28, 120–126.

- Fohanno, V., Begon, M., Lacouture, P., Colloud, F., 2014. Estimating joint kinematics of a whole body chain model with closed-loop constraints. *Multibody Syst. Dyn.* 31, 433–449.
- Fong, D.T.P., Chan, Y.Y., 2010. The use of wearable inertial motion sensors in human lower limb biomechanics studies: A systematic review. *Sensors (Switzerland)* 10, 11556–11565.
- Fox, R.J., Harner, C.D., Sakane, M., Carlin, G.J., Woo, S.L.-Y., 1998. Determination of the In Situ Forces in the Human Posterior Cruciate Ligament Using Robotic Technology: A Cadaveric Study. *Am. J. Sport. Med.* 26, 395–401.
- Freeman, M.A.R., Pinskerova, V., 2005. The movement of the normal tibio-femoral joint. *J. Biomech.* 38, 197–208.
- Fujie, H., 2015. A Novel Robotic System for Joint Biomechanical Tests : Application to the Human Knee Joint. *J. Biomech. Eng.* 126, 54–61.
- Garcia De Jalon, J., Cuadrado, J., Avello, A., Jimenez, J.M., 1994. Kinematic dynamic simulation of rigid and flexible systems with fully Cartesian coordinates. In: Seabra Pereira, M.O., Ambrósio, J.C. (Eds.), *Computer-Aided Analysis of Rigid and Flexible Mechanical Systems*, NATO ASI Series. Springer Netherlands, pp. 285–323.
- Garling, E.H., Kaptein, B.L., Mertens, B., Barendregt, W., Veeger, H.E.J., Nelissen, R.G.H.H., Valstar, E.R., 2008. Soft-tissue artefact assessment during step-up using fluoroscopy and skin-mounted markers. *J. Biomech.* 41, 2332–2333.
- Gasparutto, X., Sancisi, N., Jacquelin, E., Parenti-Castelli, V., Dumas, R., 2015. Validation of a multi-body optimization with knee kinematic models including ligament constraints. *J. Biomech.* 48, 1141–1146.
- Grimpampi, E., Camomilla, V., Cereatti, A., De Leva, P., Cappozzo, A., 2014. Metrics for describing soft-tissue artefact and its effect on pose, size, and shape of marker clusters. *IEEE Trans. Biomed. Eng.* 61, 362–367.
- Hagemeister, N., Duval, N., Yahia, L., Krudwig, W., Witzel, U., de Guise, J.A., 2002. Comparison of two methods for reconstruction of the posterior cruciate ligament using a computer based method: Quantitative evaluation of laxity, three-dimensional kinematics and ligament deformation measurement in cadaver knees. *Knee* 9, 291–299.
- Hagemeister, N., Parent, G., Van De Putte, M., St-Onge, N., Duval, N., de Guise, J., 2005. A reproducible method for studying three-dimensional knee kinematics. *J. Biomech.* 38, 1926–1931.
- Hagemeister, N., Senk, M., Dumas, R., Chèze, L., 2011. Effect of axis alignment on in vivo shoulder kinematics. *Comput. Methods Biomech. Biomed. Engin.* 14, 755–61.
- Hanlon, M., Anderson, R., 2009. Real-time gait event detection using wearable sensors. *Gait Posture* 30, 523–527.
- Hara, R., Sangeux, M., Baker, R., McGinley, J., 2014. Quantification of pelvic soft tissue artifact in multiple static positions. *Gait Posture* 39, 712–717.
- Heller, M.O., Bergmann, G., Deuretzbacher, G., Dürselen, L., Pohl, M., Claes, L., Haas, N.P., Duda, G.N., 2001. Musculo-skeletal loading conditions at the hip during walking and stair climbing. *J. Biomech.* 34, 883–893.
- Heller, M.O., Kratzstein, S., Ehrig, R.M., Wassilew, G., Duda, G.N., Taylor, W.R., 2011. The weighted optimal common shape technique improves identification of the hip joint center of rotation in vivo. *J. Orthop. Res.* 29, 1470–1475.
- Holden, J.P., Orsini, J.A., Siegel, K.L., Kepple, T.M., Gerber, L.H., Stanhope, S.J., 1997. Surface movement errors in shank kinematics and knee kinetics during gait. *Gait Posture* 5, 217–227.

- Horn, B.K.P., Hilden, H.M., Negahdaripour, S., 1988. Closed-form solution of absolute orientation using orthonormal matrices. *J. Opt. Soc. Am. A* 5, 1127.
- Houck, J., Yack, H.J., Cuddeford, T., 2004. Validity and comparisons of tibiofemoral orientations and displacement using a femoral tracking device during early to mid stance of walking. *Gait Posture* 19, 76–84.
- Hsieh, H.J., Hu, C.C., Lu, T.W., Kuo, M.Y., Hsu, H.C., 2015. Evaluation of three force-position hybrid control methods for a robot-based biological joint testing system. *Biomed. Eng. Online* In press.
- Kalman, R.E., others, 1960. A new approach to linear filtering and prediction problems. *J. basic Eng.* 82, 35–45.
- Kanamori, A., Woo, S.L.Y., Ma, C.B., Zeminski, J., Rudy, T.W., Li, G., Livesay, G.A., 2000. The forces in the anterior cruciate ligament and knee kinematics during a simulated pivot shift test: A human cadaveric study using robotic technology. *Arthroscopy* 16, 633–639.
- Kapandji, A., 2009. Anatomie fonctionnelle tome 2 : membre inférieur.
- Khurelbaatar, T., Kim, K., Lee, S., Hyuk, Y., 2015. Gait & Posture Consistent accuracy in whole-body joint kinetics during gait using wearable inertial motion sensors and in-shoe pressure sensors. *Gait Posture* 42, 65–69.
- Kiss, R.M., 2010. Effect of walking speed and severity of hip osteoarthritis on gait variability. *J. Electromyogr. Kinesiol.* 20, 1044–1051.
- Kiss, R.M., Kocsis, L., Knoll, Z., 2004. Joint kinematics and spatial-temporal parameters of gait measured by an ultrasound-based system. *Med. Eng. Phys.* 26, 611–620.
- Koell, P., Chèze, L., Dumas, R., 2010. Prediction of internal spine configuration from external measurements using a multi-body model of the spine. *Comput. Methods Biomech. Biomed. Engin.* 13, 79–80.
- Kondo, A., Doki, H., Hirose, K., 2012. An attempt of a new motion measurement method for alpine ski turns using inertial sensors. *Procedia Eng.* 34, 421–426.
- Koning, B.H.W., van der Krogt, M.M., Baten, C.T.M., Koopman, B.F.J.M., 2015. Driving a musculoskeletal model with inertial and magnetic measurement units. *Comput. Methods Biomech. Biomed. Engin.* 37–41.
- Krouwer, J.S., 2008. Why Bland-Altman plots should use X , not $(Y + X)/2$ when X is a reference method. *Stat. Med.* 27, 778–780.
- Kun, L., Inoue, Y., Shibata, K., Enguo, C., 2011. Ambulatory estimation of knee-joint kinematics in anatomical coordinate system using accelerometers and magnetometers. *IEEE Trans. Biomed. Eng.* 58, 435–442.
- Kuo, M.Y., Tsai, T.Y., Lin, C.C., Lu, T.W., Hsu, H.C., Shen, W.C., 2011. Influence of soft tissue artifacts on the calculated kinematics and kinetics of total knee replacements during sit-to-stand. *Gait Posture* 33, 379–384.
- Lafortune, M.A., Cavanagh, P.R., Sommer, H.J., Kalenak, A., 1992. Three-dimensional kinematics of the human knee during walking. *J. Biomech.* 25, 347–357.
- Lamberto, G., Richard, V., Dumas, R., Valentini, P.P., Pennestrì, E., Lu, T.-W., Camomilla, V., Cappozzo, A., 2016. Modeling the Human Tibiofemoral Joint Using Ex Vivo Determined Compliance Matrices. *J. Biomech. Eng.* 138, 061010.
- Latash, M.L., Zatsiorsky, V.M., 1993. Joint stiffness: Myth or reality? *Hum. Mov. Sci.* 12, 653–692.
- Lau, H.-Y., Tong, K.-Y., Zhu, H., 2008. Support vector machine for classification of walking conditions using miniature kinematic sensors. *Med. Biol. Eng. Comput.* 46, 563–573.

- Leardini, A., Chiari, A., Della Croce, U., Cappozzo, A., 2005. Human movement analysis using stereophotogrammetry Part 3. Soft tissue artifact assessment and compensation. *Gait Posture* 21, 212–225.
- Legnani, G., Casolo, F., Righettini, P., Zappa, B., 1996. A homogeneous matrix approach to 3D kinematics and dynamics - I. Theory. *Mech. Mach. Theory* 31, 573–587.
- Lenhart, R.L., Kaiser, J., Smith, C.R., Thelen, D.G., 2015. Prediction and Validation of Load-Dependent Behavior of the Tibiofemoral and Patellofemoral Joints During Movement. *Ann. Biomed. Eng.* 43, 2675–2685.
- Li, K., Zheng, L., Tashman, S., Zhang, X., 2012. The inaccuracy of surface-measured model-derived tibiofemoral kinematics. *J. Biomech.* 45, 2719–2723.
- Li, Y., Fan, S., Guo, Z., Li, J., Cao, L., Zhuang, H., 2013. Mathieu equation with application to analysis of dynamic characteristics of resonant inertial sensors. *Commun. Nonlinear Sci. Numer. Simul.* 18, 401–410.
- Liu, K., Liu, T., Shibata, K., Inoue, Y., Zheng, R., 2009. Novel approach to ambulatory assessment of human segmental orientation on a wearable sensor system. *J. Biomech.* 42, 2747–2752.
- Loch, D.A., Luo, Z., Lewis, J.L., Stewart, N.J., 1992. A theoretical model of the knee and ACL: Theory and experimental verification. *J. Biomech.* 25, 81–90.
- Lovejoy, C.O., 2005a. The natural history of human gait and posture Part 1. Spine and pelvis. *Gait Posture* 21, 95–112.
- Lovejoy, C.O., 2005b. The natural history of human gait and posture: Part 2. Hip and thigh. *Gait Posture* 21, 113–124.
- Lu, T.W., Chang, C.F., 2012. Biomechanics of human movement and its clinical applications. *Kaohsiung J. Med. Sci.* 28, S13–S25.
- Lu, T.W., O'Connor, J.J., 1999. Bone position estimation from skin marker co-ordinates using global optimisation with joint constraints. *J. Biomech.* 32, 129–134.
- Lucchetti, L., Cappozzo, A., Cappello, A., Della Croce, U., 1998. Skin movement artefact assessment and compensation in the estimation of knee-joint kinematics. *J. Biomech.* 31, 977–984.
- Luinge, H.J., Veltink, P.H., 2005. Measuring orientation of human body segments using miniature gyroscopes and accelerometers. *Med. Biol. Eng. Comput.* 43, 273–282.
- Manal, K., McClay, I., Stanhope, S., Richards, J., Galinat, B., 2000. Comparison of surface mounted markers and attachment methods in estimating tibial rotations during walking: An in vivo study. *Gait Posture* 11, 38–45.
- Marey, M., 1873. De la Locomotion Terrestre chez les Bipèdes et les Quadrupèdes, *Journal de l'Anatomie et de la Physiologie*. Impr. E. Martinet.
- Marin, F., Hoang, N., Aufaure, P., Ho Ba Tho, M.C., 2010. In vivo intersegmental motion of the cervical spine using an inverse kinematics procedure. *Clin. Biomech.* 25, 389–396.
- Marler, R.T., Arora, J.S., 2004. Survey of multi-objective optimization methods for engineering. *Struct. Multidiscip. Optim.* 26, 369–395.
- Marouane, H., Shirazi-Adl, a, Adouni, M., 2013. Knee joint passive stiffness and moment in sagittal and frontal planes markedly increase with compression. *Comput. Methods Biomech. Biomed. Engin.* 18, 37–41.
- Martelli, S., Valente, G., Viceconti, M., Taddei, F., 2015. Sensitivity of a subject-specific musculoskeletal model to the uncertainties on the joint axes location. *Comput. Methods Biomech. Biomed. Engin.* 18, 1555–63.

- Masum, M.A., Pickering, M., Lambert, A., Scarvell, J., Smith, P., 2014. Accuracy assessment of Tri-plane B-mode ultrasound for non-invasive 3D kinematic analysis of knee joints. *Biomed. Eng. Online* 13, 122.
- Mayagoitia, R.E., Nene, A. V., Veltink, P.H., 2002. Accelerometer and rate gyroscope measurement of kinematics: An inexpensive alternative to optical motion analysis systems. *J. Biomech.* 35, 537–542.
- Mazzà, C., Donati, M., McCamley, J., Picerno, P., Cappozzo, A., 2012. An optimized Kalman filter for the estimate of trunk orientation from inertial sensors data during treadmill walking. *Gait Posture* 35, 138–142.
- McLaughlin, P., 2013. Testing agreement between a new method and the gold standard-How do we test? *J. Biomech.* 46, 2757–2760.
- Moissenet, F., Chèze, L., Dumas, R., 2014. A 3D lower limb musculoskeletal model for simultaneous estimation of musculo-tendon, joint contact, ligament and bone forces during gait. *J. Biomech.* 47, 50–58.
- Moniz-Pereira, V., Cabral, S., Carnide, F., Veloso, A.P., 2014. Sensitivity of joint kinematics and kinetics to different pose estimation algorithms and joint constraints in the elderly. *J. Appl. Biomech.* 30, 446–460.
- Moore, K.L., Dalley, A.F., 2006. Clinically orientated anatomy.
- Muybridge, E., 1887. *Animal Locomotion: An Electro-photographic Investigation of Consecutive Phases of Animal Movements, Prospectus and Catalogue of Plates.* University of Pennsylvania.
- Netter, F.H., 2010. *Atlas of Human Anatomy.*
- O'Connor, J.J., Lu, T.-W., Wilson, D.R., Feikes, J., Leardini, a., 1998. Review: Diarthrodial Joints-Kinematic Pairs, Mechanisms or Flexible Structures? *Comput. Methods Biomech. Biomed. Engin.* 1, 123–150.
- O'Donovan, K.J., Kamnik, R., O'Keeffe, D.T., Lyons, G.M., 2007. An inertial and magnetic sensor based technique for joint angle measurement. *J. Biomech.* 40, 2604–2611.
- Orgerie, A.C., Lefèvre, L., Gelas, J.P., 2008. Save watts in your grid: Green strategies for energy-aware framework in large scale distributed systems. *Proc. Int. Conf. Parallel Distrib. Syst. - ICPADS.* Citeseer.
- Parenti-castelli, V., Gregorio, R.D.I., Meccanica, D., Connor, J.J.O., 2004. On the Modeling of Passive Motion of the Human Knee Joint by Means 219–232.
- Paul, L.A., Gros, D.F., Strachan, M., Worsham, G., Foa, E.B., Acierno, R., 2014. Prolonged exposure for guilt and shame in a veteran of Operation Iraqi Freedom. *Am. J. Psychother.* 68, 277–286.
- Pennock, G.R., Clark, K.J., 1990. An anatomy-based coordinate system for the description of the kinematic displacements in the human knee. *J. Biomech.* 23, 1209–1218.
- Peters, A., Baker, R., Sangeux, M., 2010a. Validation of 3-D freehand ultrasound for the determination of the hip joint centre. *Gait Posture* 31, 530–532.
- Peters, A., Galna, B., Sangeux, M., Morris, M., Baker, R., 2010b. Quantification of soft tissue artifact in lower limb human motion analysis: A systematic review. *Gait Posture* 31, 1–8.
- Picerno, P., Cereatti, A., Cappozzo, A., 2008. Joint kinematics estimate using wearable inertial and magnetic sensing modules. *Gait Posture* 28, 588–595.
- Picerno, P., Cereatti, A., Cappozzo, A., 2011. A spot check for assessing static orientation consistency of inertial and magnetic sensing units. *Gait Posture* 33, 373–378.

- Ramsey, D.K., Wretenberg, P.F., Benoit, D.L., Lamontagne, M., Németh, G., 2003. Methodological concerns using intra-cortical pins to measure tibiofemoral kinematics. *Knee Surg. Sports Traumatol. Arthrosc.* 11, 344–349.
- Reed, M., Manary, M., Schneider, L., 1999. Methods for Measuring and Representing Automotive Occupant Posture. SAE Tech. Pap.
- Reinbolt, J.A., Schutte, J.F., Fregly, B.J., Koh, B. II, Haftka, R.T., George, A.D., Mitchell, K.H., 2005. Determination of patient-specific multi-joint kinematic models through two-level optimization. *J. Biomech.* 38, 621–626.
- Reinschmidt, C., Van Den Bogert, A.J., Lundberg, A., Nigg, B.M., Murphy, N., Stacoff, A., Stano, A., 1997a. Tibiofemoral and tibiocalcaneal motion during walking: External vs. Skeletal markers. *Gait Posture* 6, 98–109.
- Reinschmidt, C., Van Den Bogert, A.J., Nigg, B.M., Lundberg, A., Murphy, N., 1997b. Effect of skin movement on the analysis of skeletal knee joint motion during running. *J. Biomech.* 30, 729–732.
- Richard, V., Camomilla, V., Chèze, L., Cappozzo, A., Dumas, R., 2012. Feasibility of incorporating a soft tissue artefact model in multi-body optimisation. *Comput. Methods Biomech. Biomed. Engin.* 15, 194–196.
- Roetenberg, D., Luinge, H.J., Baten, C.T.M., Veltink, P.H., 2005. Compensation of magnetic disturbances improves inertial and magnetic sensing of human body segment orientation. *IEEE Trans. Neural Syst. Rehabil. Eng.* 13, 395–405.
- Ryu, T., Choi, H.S., Chung, M.K., 2009. Soft tissue artifact compensation using displacement dependency between anatomical landmarks and skin markers - a preliminary study. *Int. J. Ind. Ergon.* 39, 152–158.
- Sabatini, A.M., 2006. Inertiel sensing in biomechanics: a survey of computational techniques bridging motion analysis and personal navigation. *Comput. Intell. Mov. Sci.* 70 – 100.
- Sancisi, N., Parenti-Castelli, V., 2011. A sequentially-defined stiffness model of the knee. *Mech. Mach. Theory* 46, 1920–1928.
- Sandholm, A., Schwartz, C., Pronost, N., De Zee, M., Voigt, M., Thalmann, D., 2011. Evaluation of a geometry-based knee joint compared to a planar knee joint. *Vis. Comput.* 27, 161–171.
- Sangeux, M., Marin, F., Charleux, F., Dürselen, L., Ho Ba Tho, M.C., 2006. Quantification of the 3D relative movement of external marker sets vs. bones based on magnetic resonance imaging. *Clin. Biomech.* 21, 984–991.
- Sati, M., de Guise, J.A., Larouche, S., Drouin, G., 1996. Improving in vivo knee kinematic measurements: Application to prosthetic ligament analysis. *Knee* 3, 179–190.
- Scheys, L., Desloovere, K., Spaepen, A., Suetens, P., Jonkers, I., 2011. Calculating gait kinematics using MR-based kinematic models. *Gait Posture* 33, 158–164.
- Sholukha, V., Leardini, A., Salvia, P., Rooze, M., Van Sint Jan, S., 2006a. Double-step registration of in vivo stereophotogrammetry with both in vitro 6-DOFs electrogoniometry and CT medical imaging. *J. Biomech.* 39, 2087–2095.
- Sholukha, V., Leardini, A., Salvia, P., Rooze, M., Van Sint Jan, S., 2006b. Double-step registration of in vivo stereophotogrammetry with both in vitro 6-DOFs electrogoniometry and CT medical imaging. *J. Biomech.* 39, 2087–2095.
- Soderkvist, I., Wedin, P., 1993. Determining the movements of the skeleton using well-configured markers. *J. Biomech.* 26, 1473–1477.
- Stagni, R., Fantozzi, S., Cappello, A., 2009. Double calibration vs. global optimisation: Performance

- and effectiveness for clinical application. *Gait Posture* 29, 119–122.
- Stagni, R., Fantozzi, S., Cappello, A., Leardini, A., 2005. Quantification of soft tissue artefact in motion analysis by combining 3D fluoroscopy and stereophotogrammetry: A study on two subjects. *Clin. Biomech.* 20, 320–329.
- Stops, A., Wilcox, R., Jin, Z., 2011. Computational modelling of the natural hip: a review of finite element and multibody simulations. *Comput. Methods Biomech. Biomed. Engin.* 15, 963–979.
- Südhoff, I., Van Driessche, S., Laporte, S., de Guise, J.A., Skalli, W., 2007. Comparing three attachment systems used to determine knee kinematics during gait. *Gait Posture* 25, 533–543.
- Torres-Moreno, J., Blanco-Claraco, J., Giménez-Fernández, A., Sanjurjo, E., Naya, M., 2016. Online Kinematic and Dynamic-State Estimation for Constrained Multibody Systems Based on IMUs. *Sensors* 16, 333.
- Tranberg, R., Karlsson, D., 1998. The relative skin movement of the foot: A 2-D roentgen photogrammetry study. *Clin. Biomech.* 13, 71–76.
- Tsai, T.Y., Lu, T.W., Kuo, M.Y., Lin, C.C., 2011. Effects of soft tissue artifacts on the calculated kinematics and kinetics of the knee during stair-ascent. *J. Biomech.* 44, 1182–1188.
- Valente, G., Pitto, L., Stagni, R., Taddei, F., 2015. Effect of lower-limb joint models on subject-specific musculoskeletal models and simulations of daily motor activities. *J. Biomech.* 48, 4198–4205.
- Valente, G., Pitto, L., Testi, D., Seth, A., Delp, S.L., Stagni, R., Viceconti, M., Taddei, F., 2014. Are subject-specific musculoskeletal models robust to the uncertainties in parameter identification? *PLoS One* 9, e112625.
- van den Bogert, A.J., Reinschmidt, C., Lundberg, A., 2008. Helical axes of skeletal knee joint motion during running. *J. Biomech.* 41, 1632–1638.
- Willemsen, A.T.M., Frigo, C., Boom, H.B.K., 1991. Lower extremity angle measurement with accelerometers - error and sensitivity analysis. *IEEE Trans. Biomed. Eng.* 38, 1186–1193.
- Willemsen, A.T.M., van Alst?, J.A., Boom, H.B.K., 1990. Real-time gait assessment utilizing a new way of accelerometry. *J. Biomech.* 23, 859–863.
- Wong, Y., Kim, W., Ying, N., 2005. Passive motion characteristics of the talocrural and the subtalar joint by dual Euler angles. *J. Biomech.* 38, 2480–2485.
- Wu, G., Siegler, S., Allard, P., Kirtley, C., Leardini, A., Rosenbaum, D., Whittle, M., D'Lima, D.D., Cristofolini, L., Witte, H., Schmid, O., Stokes, I., 2002. ISB recommendation on definitions of joint coordinate system of various joints for the reporting of human joint motion—part I: ankle, hip, and spine. *J. Biomech.* 35, 543–548.